Development of a Data-Driven Algorithm to Determine the W+Jets Background in $t\bar{t}$ Events in ATLAS

DISSERTATION

zur Erlangung des akademischen Grades

Dr. rer. nat.
im Fach Physik

eingereicht an der
Mathematisch-Wissenschaftlichen Fakultät I
Humboldt-Universität zu Berlin

von
Sascha Mehlhase M.Sc.
geboren am 12.04.1981 in Berlin

Präsident der Humboldt-Universität zu Berlin:
Prof. Dr. Dr. h.c. Christoph Markschies

Dekan der Mathematisch-Wissenschaftlichen Fakultät I:
Prof. Dr. Andreas Herrmann

Gutachter:
1. Prof. Dr. Hermann Kolanoski
2. Dr. Ulrich Husemann
3. Prof. Dr. Wolfgang Wagner

eingereicht am: 31. Mai 2010
Tag der mündlichen Prüfung: 12. Juli 2010

Studies presented in this thesis are or will be part of the following notes/papers:

- *G. Aad et al. (ATLAS Collaboration). Expected Performance of the ATLAS Experiment - Detector, Trigger and Physics. CERN, Geneva, 2009*
- *ATLAS Pixel Collaboration. Commissioning of the ATLAS Pixel Detector. Technical Report ATL-COM-INDET-2010-???, CERN, Geneva, in preparation*
- *J. Dopke et al. (ATLAS Pixel Collaboration). Commissioning of the ATLAS Pixel Optical Readout Link. Technical Report ATL-COM-INDET-2010-047, CERN, Geneva, Mar 2010. Internal note*
- *ATLAS Pixel Collaboration. A Summary of Thermal Measurements from the Pixel Commissioning Program of 2008. Technical Report ATL-COM-INDET-2010-???, CERN, Geneva, in preparation. Internal note*

This thesis was typeset with LaTeX/pdfTeX.

Published at the Humboldt-Universität zu Berlin, Berlin, Germany.

Abstract

The physics of the top quark is one of the key components in the physics programme of the ATLAS experiment at the Large Hadron Collider at CERN.

In this thesis, general studies of the jet trigger performance for top quark events using fully simulated Monte Carlo samples are presented and two data-driven techniques to estimate the multi-jet trigger efficiency and the W+Jets background in top pair events are introduced to the ATLAS experiment.

In a *tag-and-probe* based method, using a simple and common event selection and a high transverse momentum lepton as tag object, the possibility to estimate the multi-jet trigger efficiency from data in ATLAS is investigated and it is shown that the method is capable of estimating the efficiency without introducing any significant bias by the given tag selection.

In the second data-driven analysis a new method to estimate the W+Jets background in a top-pair event selection is introduced to ATLAS. By defining signal and background dominated regions by means of the jet multiplicity and the pseudo-rapidity distribution of the lepton in the event, the W+Jets contribution is extrapolated from the background dominated into the signal dominated region. The method is found to estimate the given background contribution as a function of the jet multiplicity with an accuracy of about 25% for most of the top dominated region with an integrated luminosity of above 100 pb^{-1} at $\sqrt{s} = 10$ TeV.

This thesis also covers a study summarising the thermal behaviour and expected performance of the Pixel Detector of ATLAS. All measurements performed during the commissioning phase of 2008/09 yield results within the specification of the system and the performance is expected to stay within those even after several years of running under LHC conditions.

Zusammenfassung

Die Physik des Top-Quarks ist eine Schlüsselkomponente im Forschungsprogramm des ATLAS-Experiments am CERN.

In dieser Arbeit werden Untersuchungen zur Leistungfähigkeit von Jet-Triggern für Top-Quark-Ereignisse präsentiert und zwei datenbasierte Methoden zur Abschätzung der Multijet-Triggereffizienz und des W+Jets-Untergrundes in Top-Quark-Ereignissen in ATLAS eingeführt.

In einer *tag-and-probe* Methode, basierend auf einer einfachen und allgemeinen Ereignisselektion und einem hochenergetischen Lepton als Tag, wird die Möglichkeit zur Bestimmung der Multijet-Triggereffizienz aus Daten heraus evaluiert, und es wird gezeigt, dass die Methode in der Lage ist, die Effizienz ohne signifikante Verfälschung durch die Tag-Selektion zu bestimmen.

In der zweiten datenbasierten Analyse wird eine neue Methode zur Abschätzung des W+Jets-Untergrundes in ATLAS eingeführt. Durch die Definition von signal- und untergrunddominierten Bereichen in Jet-Muliplizität und Pseudorapidität des Leptons wird der Anteil der W+Jets-Ereignisse aus der untergrunddominierten in die signaldominierte Region extrapoliert. Es wird gezeigt, dass die Methode, mit einer integrierten Luminosität von 100 pb^{-1} bei $\sqrt{s} = 10$ TeV, in der Lage ist den Untergrundbeitrag als Funktion der Jet-Muliplizität mit etwa 25% Genauigkeit im Großteil der signaldominierten Region zu bestimmen.

Diese Arbeit umfaßt zudem eine Studie zum thermischen Verhalten und der erwarteten thermischen Leistung des Pixel-Detektors in ATLAS. Alle Messungen, durchgeführt während der Inbetriebnahme des Systems in 2008/09, zeigen Ergebnisse innerhalb der Spezifikationen beziehungweise deuten auf deren Einhaltung auch nach mehreren Betriebsjahren unter LHC-Bedingungen hin.

Contents

Chapter 1.

Introduction

Throughout the history of mankind the nature of matter has been subject of investigation. Always aimed to find the constituents of matter and to describe their interactions, the means used for this investigation have evolved from philosophy to natural science.

The field of elementary particle physics may be said to have emerged with the discovery of the electron more than 100 years ago. But it was the discovery of elementary particles in cosmic rays in the middle of the 20th century when the subject really came into bloom. Since then the construction of dedicated experiments and the development of theories to incorporate their findings as well as the experimental test of predictions in turn have led to an unified theory describing both the building blocks of matter and the interactions between them.

The *Standard Model* of particle physics has been extensively tested by many experiments, and has been found to accurately predict the outcome of various experiments. With the exception of the tau neutrino the top quark was, with the exception of the Higgs boson, the last missing piece in the framework of the *Standard Model*. Anticipated since the discovery of the bottom quark in 1977 [1], its mass has been predicted through precision data since the early nineties. The actual discovery was achieved at the Tevatron only in 1995 [2, 3]. Until recently the Tevatron was the only place to produce the top quark in an experimental environment. Mainly due to the low statistics its properties are only roughly measured. This limitation is going to vanish with the start-up of the Large Hadron Collider (LHC), being able to produce top quarks at a rate orders of magnitude larger than at the Tevatron.

As heavy as a gold atom, the top quark is about five orders of magnitude heavier than the up and down quark. Due to this large mass the top quark has unique features among all elementary matter particles. It allows for studies of perturbative Quantum Chromodynamics as well as a possible mechanism for electroweak symmetry breaking. Potential *new physics* is likely to manifest itself in deviations from *Standard Model* predictions also in the top quark sector. Finally events containing top quarks will be a major background in searches for *new physics*. To study the top quark at an experiment such as ATLAS it is among other things important to efficiently select events containing top quarks and to have precise knowledge of the major backgrounds of these.

This dissertation describes methods for both an estimation of the efficiency of jet based triggers, to be used to select top-pair events, and an estimation of the major background of events containing top quarks, designed to use real measured data as input (data-driven) and to be as much as possible independent from Monte Carlo simulations. An overview of the underlying physics and the properties of the top quark is given in Chapter 2. In the second part of the Chapter, the decay topologies of events with top quarks and the main backgrounds are outlined. In Chapter 3 the experimental setup is described, with emphasis on parts used for the studies presented in this thesis. Studies of the thermal performance of the ATLAS Pixel Detector are summarised in Appendix A. Generation, simulation and content of the Monte Carlo samples used for the analyses presented in this thesis are sketched in Chapter 4. In Chapter 5 the reconstruction and identification of final state objects as well as the event selection is detailed. Chapter 6 contains the efficiency studies of jet-based triggers and describes a possible data-driven estimate of their efficiency. In Chapter 7 the method for estimating the background coming from W bosons produced with associated jets is introduced and its estimated uncertainties are discussed. Chapter 8 gives a summary of the results and an outlook.

Chapter 2.

Theoretical Overview

The *Standard Model* (SM) of particle physics can account for essentially all experimental data from high energy experiments. It is characterised in part by a small set of twelve fundamental spin $\frac{1}{2}$ matter particles (fermions, six quarks and six leptons) and three different interactions. The interactions are described by the exchange of characteristic particles of spin one (bosons), between the fermions. An overview of fermions and bosons within the *Standard Model*, along with their electric charge and year of discovery is given in Table 2.1. Furthermore the *Standard Model* is marked by two crucial properties, gauge invariance and renormalisability. Gauge invariance allows for the freedom to change the phase of a fermion field globally as well as locally at any point in space-time, without changing the physics. By demanding it, a theory can describe conserved currents and the conservation of electric charge. Renormalisability in turn describes the ability to use physical values such as mass (m) or charge (e) as a replacement for products of a purely fictitious and unmeasurable *bare* mass (m_0) or charge (e_0) and a dimensionless term containing divergent integrals. These divergent integrals arise from the fact that virtual processes, with no restriction on their momentum, *dress* the *bare* state (self-energy) and contribute to the measurable quantity. As a result of renormalisation coupling *constants*, such as α_{QED}, are made dependent on the energy scale at which they are observed. An introduction and discussion of the *Standard Model* in greater depth can be found for example in [4], [5] and [6]. The fundamentals of Electroweak Theory are given in [7–9] and the bases of Quantum Chromodynamics are imparted in [10–12]. In the following sections the role of the top quark within the *Standard Model* is described, with details on the production (Section 2.1.1), especially at high energy hadron colliders such as the Large Hadron Collider, its decay (Section 2.1.2) as well as its properties (Section 2.1.3). Since they are crucial for the detection and the reconstruction of top quarks, the signatures of top decays plus those of the most important background processes are discussed in the final part of this chapter (Section 2.2).

2.1. Physics of the Top Quark

The importance of the top quark within the framework of the *Standard Model* as well as for possible extensions of it has already been indicated above. In this chapter this will be outlined in more detail: The production, both via the strong interaction and the electroweak interaction, and its decay are summarised. Its properties, their most recent measurement and/or prediction and possible conclusions to draw from those, are stated.

Table 2.1.: Fundamental matter fermions and gauge bosons within the *Standard Model*. The year of discovery is given in parentheses. $Q/|e|$ denotes the electric charge of the particle in units of the absolute electric charge of the electron.

		Flavour		**Q/|e|**
Leptons	ν_e (1953) [13]	ν_μ (1962) [14]	ν_τ (2000) [15]	≈ 0
	e (1897) [16]	μ (1936) [17]	τ (1975) [18]	-1
Quarks	u (1964) [19]	c (1974) [20, 21]	t (1995) [2, 3]	$+2/3$
	d (1964) [19]	s (1964) [19]	b (1977) [1]	$-1/3$
Bosons		g_1, ..., g_8 (1979) [22]		0
		γ (1900) [23, 24]		0
		$W^\pm$ (1983) [25, 26]		± 1
		Z^0 (1983) [27, 28]		0

2.1.1. Production

The top quark can either be produced in $t\bar{t}$ pairs via the strong interaction or singly via the electroweak interaction. Both mechanisms are describe in the following.

Pair Production via the strong interaction

Pair production via the strong interaction is, in terms of cross-section, the dominant production channel for top quarks, both at the Tevatron and the LHC. It is described by Quantum Chromodynamics, where the hard scattering process between two protons is a result of an interaction between their constituents, quarks and gluons. To be able to produce top quarks, it is the centre-of-mass energy of these partons, themselves only carrying fractions $x_i = k_i/p$ of their parent's longitudinal momenta p, that has to surpass the kinematic production threshold, set by twice the top quark mass m_t.

Factorisation of the Cross-Section To be able to calculate cross-sections even though the colliding hadrons are composite particles which in itself cannot be treated by perturbative QCD, the interaction is separated into an interaction of the whole particle composition (i.e. the proton) on a soft binding energy scale (long distance) and a parton collision on a hard energy (short distance) scale. This approach, with the soft part factored into parton distribution functions (PDFs), is called factorisation. The characteristic energy that separates the two scales is thereby called factorisation scale μ_F^2. Following the factorisation theorem [29, 30], the cross-section for a process such as top-pair production can be expressed as a convolution of the PDFs $f_{i,A/B}(x_i, \mu_F^2)$ for the colliding hadrons A and B and the hard parton-parton cross-section $\hat{\sigma}_{ij}$ of all possible combinations of two partons i and j:

$$\sigma(AB \to t\bar{t}) = \sum_{i,j} \int dx_i dx_j f_{i,A}(x_i, \mu_F^2) f_{j,B}(x_j, \mu_F^2) \hat{\sigma}_{ij}(ij \to t\bar{t}, \hat{s}, \mu_R^2), \tag{2.1}$$

where $\hat{s}$, defined as

$$\hat{s} \equiv (x_i p_A + x_j p_B)^2 \approx x_i x_j s, \tag{2.2}$$

represents the centre-of-mass energy of the colliding partons squared, μ_R^2 denotes the renormalisation scale and s is the square of the centre-of-mass energy at the hadron level, i.e. of the colliding protons. The design value at the LHC is $\sqrt{s} = 14$ TeV, while in 2010 it is limited to be $\sqrt{s} = 7$ TeV. As described above, μ_R^2 is introduced by a renormalisation procedure, removing divergences emerging from virtual loop diagrams in the calculation of partonic cross-sections. Since calculations of the cross-section can only be performed at finite orders in perturbation theory, they always depend on the chosen scale. For top quark physics both scales μ_F^2 and μ_R^2 are commonly set to the momentum scale of the hard scattering process: $\mu_F^2 = \mu_R^2 = \mu^2 = m_t^2$.

Parton Distribution Functions As introduced above the parton distribution functions (PDFs) are used to describe the soft part of the interaction. As this interaction occurs on a small momentum transfer scale it cannot be calculated in perturbative QCD. Instead PDFs, defined as the probability density for finding a particle with a certain longitudinal momentum fraction x at momentum transfer Q^2, are used. These PDFs are primarily obtained from deep-inelastic scattering experiments, such as H1 [31] and ZEUS [32] at the HERA accelerator at DESY. To be able to utilise PDFs at an energy scale Q^2 different to the one they are measured at, as necessary when going from HERA to LHC energies, the so-called DGLAP (Dokshitzer-Gribov-Lipatov-Altarelli-Parisi) evolution equations [33–35] can be used for extrapolation. According to the factorisation theorem, described above, the PDFs do not depend on the process they are measured at and can therefore be used in a calculation for any other hard scattering process. The PDF sets used for the analyses presented in this thesis are provided by the CTEQ [36] and MRST [37, 38] groups. In this thesis CTEQ6M, illustrated in Figure 2.1, is used as the main PDF set. It was derived at next-to-leading order (NLO) using the $\overline{MS}$ renormalisation scheme [39].

Production Mechanism and Threshold To be able to produce top quark pairs in a collision, the available energy has to surpass the threshold defined by the rest mass of the top quark pair, $\sqrt{\hat{s}} \geq 2m_t$. From Equation (2.2) it follows that

$$x_1 x_2 = \frac{\hat{s}}{s} \geq \frac{4m_t^2}{s}. \tag{2.3}$$

As can be seen in Figure 2.1, the probability for finding a parton with momentum fraction x decreases with increasing x. Therefore, a characteristic value for $x_1 x_2$ is close to the threshold, defining $x_1 \approx x_2 = x_{\text{thr}}$. Assuming a LHC centre-of-mass energy of $\sqrt{s} = 14$ TeV ($\sqrt{s} = 7$ TeV), Equation (2.3) gives

$$x_{\text{thr}} \approx \frac{2m_t}{\sqrt{s}} = 0.025 \quad (0.05). \tag{2.4}$$

Again looking at Figure 2.1, it can be reasoned that gluon-gluon fusion (see Figure 2.2(a)) reigns over quark-antiquark annihilation (see Figure 2.2(b)) at the LHC, due to the gluon's much larger distribution function at $x_{\text{thr}} = 0.025$. This effect is much less pronounced at

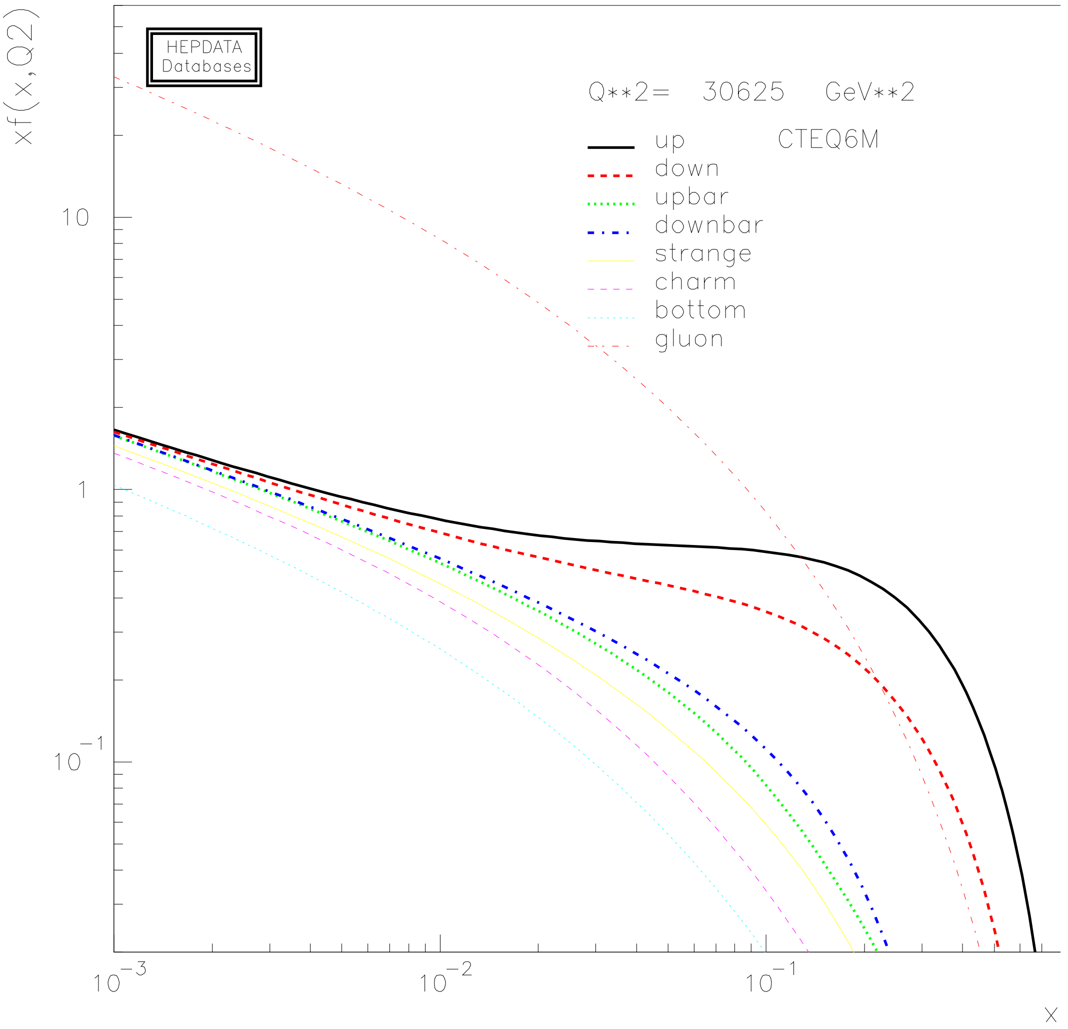

Figure 2.1.: CTEQ6M parton distribution functions for all partons in the proton at an energy scale of $Q^2 = m_t^2 = (175\text{ GeV})^2$ [36, 40].

a centre-of-mass energy of $\sqrt{s} = 7$ TeV ($x_{\text{thr}} = 0.05$) and almost reversed at the Tevatron ($\sqrt{s} = 1.96$ TeV, $x_{\text{thr}} = 0.18$).

The Parton Cross-Section After factorising out the *soft part* of the interaction, the hard parton-parton cross-section $\hat{\sigma}_{ij}$ can be calculated using perturbative QCD. In detail this is done as a perturbation series in the strong coupling constant α_s, where the leading order (LO) processes, contributing with α_s^2, are gluon-gluon fusion and quark-antiquark annihilation, as illustrated in Figures 2.2(a) and 2.2(b), respectively. The differential cross-section of the latter is; in terms of the invariant Mandelstam variables $\hat{s}$, $\hat{t}$ and $\hat{u}$; given by

$$\frac{d\hat{\sigma}}{d\hat{t}}(q\bar{q} \to t\bar{t}) = \frac{4\pi\alpha_s^2}{9\hat{s}^4} \cdot \left[(m_t^2 - \hat{t})^2 + (m_t^2 - \hat{u})^2 + 2m_t^2\hat{s}\right], \tag{2.5}$$

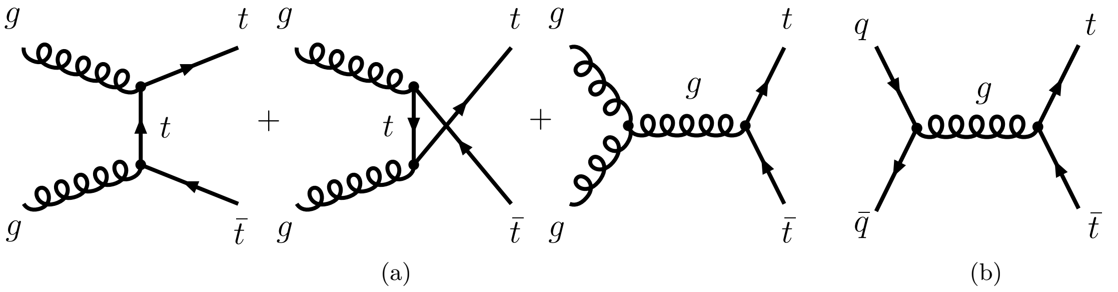

Figure 2.2.: Leading order Feynman diagrams for $t\bar{t}$ production by (a) gluon-gluon fusion and (b) quark-antiquark annihilation.

where m_t denotes the mass of the top quark and $\hat{s}$, $\hat{t}$ and $\hat{u}$ are defined as: $\hat{s} = (p_q + p_{\bar{q}})^2$, $\hat{t} = (p_q - p_t)^2$ and $\hat{u} = (p_q - p_{\bar{t}})^2$, with p_i being the four momentum of quark i. In the same way the differential cross-section for gluon-gluon fusion is given by

$$\begin{aligned}\frac{d\hat{\sigma}}{d\hat{t}}(g_1 g_2 \to t\bar{t}) = & \frac{\pi\alpha_s^2}{8\hat{s}^2} \cdot \left[\frac{6(m_t^2 - \hat{t})(m_t^2 - \hat{u})}{\hat{s}^2} - \frac{m_t^2(\hat{s} - 4m_t^2)}{3(m_t^2 - \hat{t})(m_t^2 - \hat{u})} \right. \\ & + \frac{4}{3} \cdot \frac{(m_t^2 - \hat{t})(m_t^2 - \hat{u}) - 2m_t^2(m_t^2 + \hat{t})}{(m_t^2 - \hat{t})^2} \\ & + \frac{4}{3} \cdot \frac{(m_t^2 - \hat{t})(m_t^2 - \hat{u}) - 2m_t^2(m_t^2 + \hat{u})}{(m_t^2 - \hat{u})^2} \\ & - 3 \cdot \frac{(m_t^2 - \hat{t})(m_t^2 - \hat{u}) - m_t^2(\hat{u} - \hat{t})}{\hat{s}(m_t^2 - \hat{t})^2} \\ & \left. -3 \cdot \frac{(m_t^2 - \hat{t})(m_t^2 - \hat{u}) - m_t^2(\hat{t} - \hat{u})}{\hat{s}(m_t^2 - \hat{u})^2} \right], \end{aligned} \tag{2.6}$$

where is this case the invariant Mandelstam variables are $\hat{s} = (p_{g_1} + p_{g_2})^2$, $\hat{t} = (p_{g_1} - p_t)^2$ and $\hat{u} = (p_{g_1} - p_{\bar{t}})^2$. While these formulas only represent LO perturbative calculations, complete calculations at next-to-leading order (NLO) have been performed since the late eighties [41, 42]. Since then improvement have been achieved e.g. by including next-to-leading logarithms (NLL), next-to-next-to-leading order (NNLO) soft gluon corrections or sub-leading terms of next-to-next-to-leading logarithms (NNLL). While recent ATLAS publications such as [43] used calculations presented in [44], [45] and [46], the analyses in this thesis are based on more recent calculations performed in [47]. In this so-called approximate NNLO calculation improvements due to soft gluon re-summation at NNLL accuracy are employed and a NNLO finite-order cross section, exact in all logarithmically enhanced terms near threshold, is derived analytically. Furthermore this result shows a reduced scale dependence compared to previous calculations. Table 2.2 summarises this and other recent results for a top quark mass of 175 GeV and a centre-of-mass energy of $\sqrt{s} = 14$ TeV. As can be seen in Equations (2.5) and (2.6), the cross-section for top-quark production depends strongly on the top quark mass as well as on the centre-of-mass energy (via the momentum of the interacting gluons or quarks). For the dependence on the top quark mass, the cross-section decreases with increasing mass, due to: (a) the reduced

Table 2.2.: Total cross-section predictions for $t\bar{t}$ production at LHC design energy ($\sqrt{s} = 14$ TeV) assuming a top mass of $m_t = 175$ GeV. Also the PDF set used for the calculation is given.

Cross-Section [pb]	**Order**	**PDF set**
833^{+52}_{-32} [44]	NLO + NLL	MRSR2 [48]
838^{+76}_{-78} [45]	NLO + NLL	CTEQ6M [36]
847^{+70}_{-51} [46]	≈ NNLO	CTEQ6.6M [49]
807±45 [47]	≈ NNLO	CTEQ6.5M [50]

phase space available for the hard parton-parton cross-section, (b) the scale dependence of $\alpha_s = \alpha_s(\mu^2)$, with $\mu^2 \simeq m_t^2$ and (c) the reduced probability to find a parton with $x \geq x_{\text{thr}}$ (see Equation (2.4)). The centre-of-mass energy dependence is illustrated in Figure 2.3, showing an increasing cross-section with rising $\sqrt{s}$. The causes are basically the inverse of those stated for the top-quark mass dependence: (a) an increased phase space available, (b) the scale dependence of α_s and (c) the increasing probability to surpass decreasing x_{thr}. In addition the relative contributions of gluon-gluon fusion and quark-antiquark annihilation change with the given centre-of-mass energy, as depicted in Figure 2.1.

Single-Top Production via the electroweak interaction

Besides the production in pairs of top and antitop quarks via the strong interaction, the top quark can also be produced singly via the weak interaction. Predicted for a long time, this process has been observed only recently in 2009, by the Tevatron experiments [52, 53]. The so-called single-top production directly involves the Wtb vertex and therefore allows for a *direct* measurement of V_{tb} of the Cabibbo-Kobayashi-Maskawa (CKM) matrix [54], a unitary matrix describing the mismatch of quantum states of quarks when treated as freely propagating particles and when taking part in the weak interaction. The three main single-top production modes are:

t-channel As illustrated by the leading order (LO) Feynman diagram in Figure 2.4(a), a virtual W boson interacts with a bottom quark from the *sea* inside the proton and turns it into a top quark. This mode, dominant at LHC energies, is, due to the bottom quark originating from a gluon splitting into a $b\bar{b}$ pair, also referred to as W-gluon fusion.

Associated Production In associated or Wt production the top quark is produced together with a real or quasi-real W boson from a bottom quark of the *sea* inside the proton. The LO Feynman diagram is shown in Figure 2.4(b).

s-channel Similar to the on-shell production, a W boson is produced by the fusion of two quarks. Due to the decay into a bottom and a top quark the W boson has to be off-shell (time-like). This results in a noticeable reduction of the cross-section. The corresponding LO Feynman diagram is depicted in Figure 2.4(c).

Despite the fact that single-top production is via the electroweak interaction the cross-section is by far not negligible, even similar to that of top-quark pair production. In

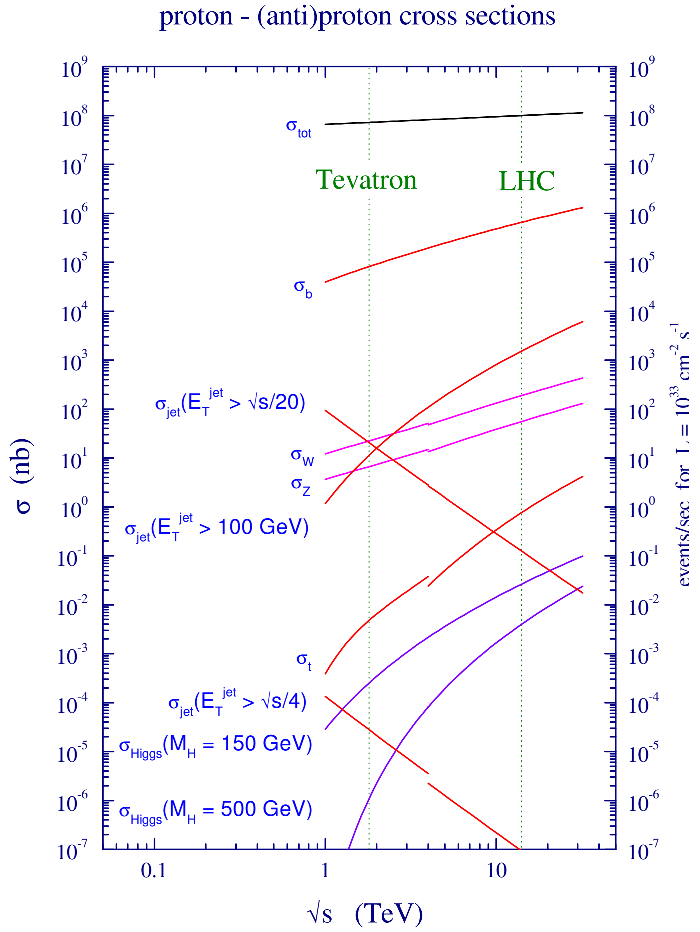

Figure 2.3.: QCD predictions for cross-sections of various processes at hadron colliders, such as the Tevatron and the LHC (using the MRST PDF set) [51]. Here σ_{tot} and σ_t denote the total and top-pair production cross-section, respectively. The steps in the curves represent the transition from $p\bar{p}$ to pp scattering.

contrast to pair production via the strong interaction single-top production is less phase space suppressed and allows for the production of real W bosons. In particular the t-channel does not suffer from colour suppression. A summary of cross-section predictions at next-to-leading order (NLO) for the three mechanisms stated above is given in Table 2.3.

2.1.2. Decay

Assuming unitarity of the CKM matrix and exactly three quark flavours, top quarks decay almost exclusively to a W boson and a bottom quark, via the weak interaction. Since $|V_{tb}| \simeq 1$, the branching fraction/ratio for this process ($BR(t \to Wb)$) is, within the *Standard Model*, predicted to be above 0.998. Thereby V_{tb} can be determined indirectly by measuring the ratio between branching fractions of $t \to Wb$ to $t \to Wq$ and directly by measuring the single-top cross-section, being proportional to $|V_{tb}|^2$ (see Section 2.1.1). In the indirect measurement q denotes diagonal CKM decay to a bottom quark as well as

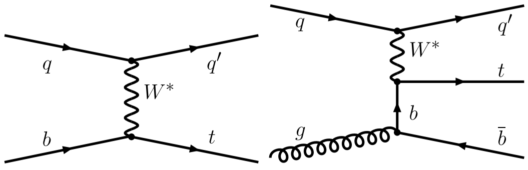

(a) t-channel

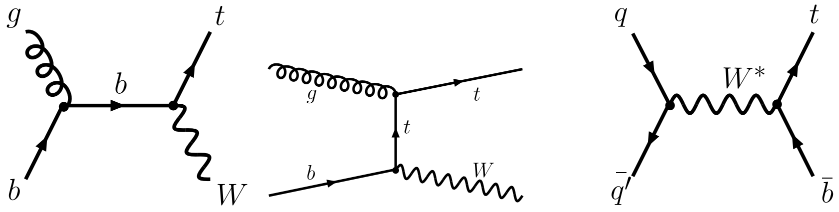

(b) Associated production

(c) s-channel

Figure 2.4.: Feynman diagrams for electroweak single-top production in (a) the t-channel, (b) associated production and (c) the s-channel.

Table 2.3.: Total cross-section predictions for single-top production at LHC design energy ($\sqrt{s} = 14$ TeV) assuming a top mass of $m_t = 175$ GeV.

Mechanism	**NLO cross-section [pb]**		
	t	$\bar{t}$	
t-channel	$155.9^{+7.5}_{-7.7}$	$90.7^{+4.3}_{-4.5}$	[55]
s-channel	$6.56^{+0.69}_{-0.63}$	$4.09^{+0.43}_{-0.39}$	[55]
Wt production	66±2	66±2	[56]

the off-diagonal to down and strange quarks and it follows

$$R = \frac{BR(t \to Wb)}{BR(t \to Wq)} = \frac{|V_{tb}|^2}{|V_{tb}|^2 + |V_{ts}|^2 + |V_{td}|^2}. \tag{2.7}$$

For the purpose of this thesis V_{tb} and therefore $BR(t \to Wb)$ are assumed to be exactly one. Neglecting the mass of the bottom quark, the total top quark width Γ_t can be expressed as

$$\Gamma_t = \frac{G_F m_t^3}{8\pi\sqrt{2}} \left(1 - \frac{m_W^2}{m_t^2}\right)^2 \left(1 + 2\frac{m_W^2}{m_t^2}\right) \left[1 - \frac{2\alpha_s}{3\pi}\left(\frac{2\pi^2}{3} - \frac{5}{2}\right)\right]. \tag{2.8}$$

With a top quark mass of 175 GeV this yields a width of approximately 1.5 GeV, which in turn results via

$$\tau_t = \frac{1}{\Gamma_t} \tag{2.9}$$

in a lifetime of about 5×10^{-25} s. As stated in Section 2.1.3, this has several implications and leads to the fact that the top quark decays as a *quasi-free* quark. The final state of the top quark decay depends upon the decay of the W boson. While all three lepton

Table 2.4.: Branching fractions for the decay of a real W boson [57]. The last column states the value used for the analyses presented in this thesis, where ℓ denotes e, μ and τ (not their sum).

W **decay**	$q\bar{q}$	$e\nu$	$\mu\nu$	$\tau\nu$	$\ell\nu$
BR [%]	67.60±0.27	10.75±0.13	10.57±0.15	11.25±0.20	10.80±0.09

families (e, μ and τ) are kinematically allowed, the hadronic W decays are kinematically limited to the first two generations (ud and cs pairs). At LO all three leptonic W decay modes have the same probability. Due to an additional colour factor, this probability is three times larger for the hadronic W decays. This gives in total nine possible decay modes with a probability of 1/9 each. Including higher order corrections this symmetry is slightly broken, as stated in Table 2.4.

2.1.3. Properties

Approximately 40 times larger than bottom quark, its weak isospin partner and next heaviest quark, the top quark takes a special place within the group of *Standard Model* matter particles. As a result of this large mass, the top quark obtains a few other distinct properties compared to the other *Standard Model* particles. The top quark is a spin $\frac{1}{2}$ fermion with an electric charge of $\frac{2}{3}e$. Under the SU(3) gauge group of strong interaction it transforms as a colour anti-triplet.

Top Quark Mass

Despite the limited statistics at the Tevatron, the top quark mass is measured with better relative precision than that of any other quark. The latest measurement, using data from both Tevatron experiments, yields a top quark mass of $m_t = 173.1 \pm 0.6$ (stat.) $\pm$ 1.1 (syst.) GeV [58] and is in good agreement with indirect measurements from *Standard Model* fits (see [58]). A retrospect on the evolution of indirect measurements via radiative correction compared to direct measurements at the Tevatron is shown in Figure 2.5(a). These radiative corrections appear as higher order contributions to a perturbation series, for example in the W boson mass:

$$m_W^2 = \frac{\pi\alpha}{\sqrt{2}G_F} \cdot \frac{1}{\sin^2\theta_W(1-\Delta r)}, \tag{2.10}$$

where G_F is the Fermi constant, θ_W is the electroweak mixing angle, defined as

$$\sin^2\theta_W = 1 - m_W^2/m_Z^2 \tag{2.11}$$

at tree level, and Δr are electroweak corrections. The Feynman diagram representation of the lowest order radiative correction to the W boson mass (m_W) involving the top quark is given in Figure 2.6(a), where a virtual top-antibottom pair is created. It is through these radiative corrections that a precise measurement of the top quark mass, in combination

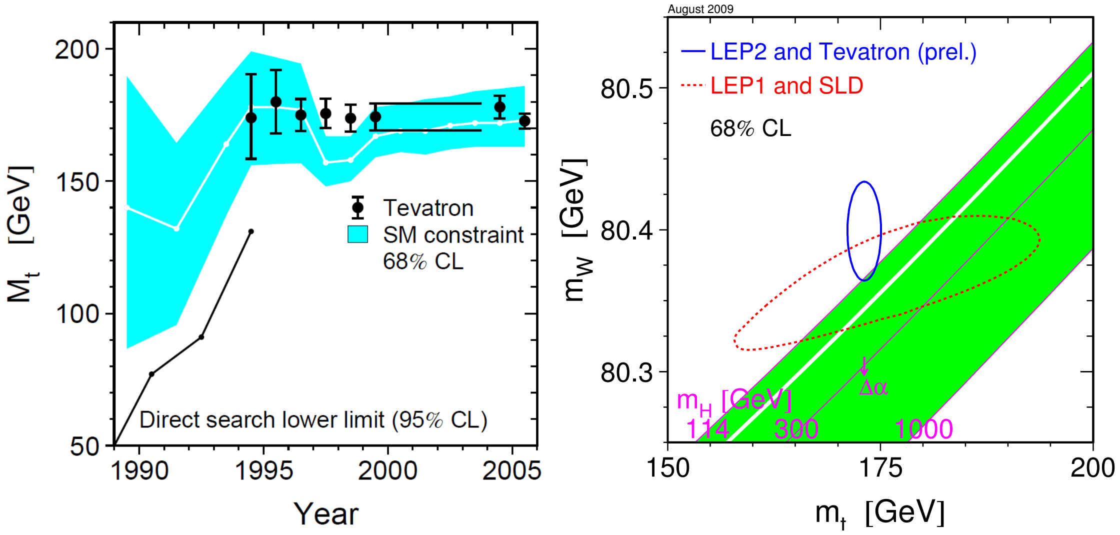

(a) (b)

Figure 2.5.: (a) Comparison between direct (points; from Tevatron data) and indirect (shaded; from radiative corrections) measurements of the top mass versus time [60]. (b) 68% confidence level contours of both indirect constraints on m_W and m_t based on LEP-I/SLD data (dashed contour) and the direct measurements from the LEP-II/Tevatron experiments (solid contour). Also shown is the SM relationship for the masses as a function of the mass of the Higgs boson [61].

with an accurate determination of the W boson mass, can provide a constraint on the Higgs boson mass. Both the top quark mass and the Higgs boson mass enter the radiative corrections: $\Delta r \propto m_t^2$ and $\Delta r \propto \log m_H$ [4]. The latter case is depicted in Figure 2.6(b). The constraint on the Higgs boson mass using recent data is shown in Figure 2.5(b).

The expected precision of the top quark measurement at the LHC is of the order of 1 GeV, completely dominated by systematic uncertainties [43]. To improve the constraint on the Higgs boson mass via radiative corrections the precision on the W boson mass measurement has to be reduced from about 25 MeV to below 15 MeV, seemingly feasible at the LHC [59].

Spin Correlations and W Helicity

As a consequence of its very short lifetime of about 5×10^{-25} s, the top quark is the only quark that decays before it hadronises. The timescale to form hadronic bound states is $O(10)$ times longer than the lifetime. As a result, the spin information is transmitted from the top quark to its decay products, and can be measured in the leptonic W boson decay. While top quarks produced in pairs are themselves unpolarised, the spins of both are correlated. Depending on the definition of the spin quantisation axis the strength of the correlation differs, but its measurement can in any case be helpful in the search for *new physics* [62].

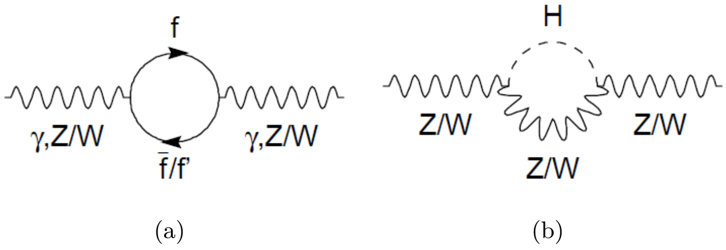

Figure 2.6.: Higher-order corrections to the gauge boson propagators due to boson and fermion loops. In (a) the top quark enters as a $t\bar{t}$-pair in the Z propagator or in combination with a $\bar{b}$ in the W propagator.

Analysing the angular distribution of the top quark and the successive W boson decay one can measure the polarisation of the W boson[1]. This serves a as complement to the top quark spin studies. Deviations from the SM predictions for the longitudinal ($F_0 = m_t^2/(2m_W^2 + m_t^2 + m_b^2) \approx 0.7$), left-handed ($F_L$) and right-handed ($F_R = 0$) helicity fractions, would bring into question the validity of the Higgs mechanism of spontaneously symmetry breaking and offer sensitivity to *new physics*. Recent measurements from the Tevatron experiments show good agreement with the SM expectations [63, 64].

Top Quark Charge

In hadron colliders such as the LHC or the Tevatron the electric charge of the top quark can be measured either directly by identifying the charge of its decay products in the main decay channel $t \to Wb$ or indirectly by studying radiative top quark processes. In the former case the determination of the charge of the associated bottom jet poses a challenging task, while measuring the charge of the W boson is *easy*, at least for the leptonic decay. In the indirect measurement, assuming the *Standard Model* electromagnetic coupling, one can infer the charge from the rate at which the top quark radiates a photon. Studies at the Tevatron experiments showed a large preference for the SM prediction of $\frac{2}{3}|e|$ over scenarios with an exotic quark of charge $-\frac{4}{3}|e|$ and similar mass (about 170 GeV) [65, 66] .

2.2. Signatures of Signal and Background

The signature of the top-quark decay is defined by the decay of the W boson, as described in the previous section. In this section, the topologies of events containing top quarks, either produced in pairs (see Section 2.1.1) or singly (see Section 2.1.1), are described. Signatures of the most important background processes, that is to say processes that give similar event topologies, are introduced as well in the order of importance.

---

[1] In detail, the angle between the lepton and the fully reconstructed top quark is measured in the W rest frame.

2.2.1. Top-Antitop Events

The possible final states of $t\bar{t}$ events can be categorised, according to the decays of the two W bosons, into three channels:

Fully-leptonic or di-leptonic ($t\bar{t} \to ll$) The so-called fully-leptonic $t\bar{t}$ decay describes the case in which both W bosons decay leptonically. In this case the final state contains two charged leptons, two neutrinos and two bottom quarks. The fact that neutrinos are not detectable by experiments makes this mode impossible to reconstruct without an ambiguity. It makes up only about 9% of all $t\bar{t}$ decays, but offers a very clean signature, at least for electrons and muons.

Semi-leptonic or lepton+jets ($t\bar{t} \to l$+jets) The semi-leptonic $t\bar{t}$ decay is the case in which one W boson decays leptonically while the other decays hadronically. Therefore the final state contains one charged lepton, one neutrino, a $q\bar{q}'$ pair and two bottom quarks. About 45% of all $t\bar{t}$ decays belong to this channel.

Fully-hadronic or alljets ($t\bar{t} \to$ jets) In the fully-hadronic $t\bar{t}$ decay ($t\bar{t}_{\mathrm{had}}$) both W bosons decay hadronically, creating a final state that contains two $q\bar{q}'$ pairs and two bottom quarks. While there is no ambiguity due to missing energy, the large number of quarks makes it hard to disentangle the decay products of each of the two top quarks. With about 46% of all $t\bar{t}$ decays this is the biggest fraction of all possible topologies. Still, due to the absence of leptons, this decay mode suffers very large background from QCD multi-jet production (described in the following).

The first two channels are commonly referred to as leptonic decay modes ($t\bar{t}_{\mathrm{lep}}$). The number of jets given for each channel is thereby derived neither considering higher order effects, such as gluon radiation, nor detector or reconstruction effects. These effects might increase the number of jets in the final state. The leptons produced in $t\bar{t}$ events usually carry high transverse momentum p_T, while the neutrinos can only be characterised in sum and in the transverse plane by missing transverse energy ($E_{\mathrm{T}}^{\mathrm{miss}}$, defined as the negative vectorial sum of all energy deposits in the calorimeters and the p_{T} of reconstructed muon tracks), a very error-prone measurement especially in first years of an experiment.

For the major fraction of studies concerning properties of the top quark, fully-leptonic and fully-hadronic $t\bar{t}$ decays hold too many difficulties, as indicated above, and are therefore often neglected[2]. The same applies for final states containing τ leptons, due to challenging reconstruction of especially the hadronic τ decay. This leaves a still sizeable fraction of about 30% of all $t\bar{t}$ decays with one high p_T charged lepton (e or μ), missing energy from the neutrino, two jets from the $q\bar{q}'$ pair and two b-jets from the bottom quarks in the final state, the so-called *Golden Channel* for top-quark physics. A summary of all possible $t\bar{t}$ decay modes and their branching fractions is shown in Figure 2.7.

2.2.2. W+Jets Events

At a hadron collider such as the LHC the main mechanism for creating W bosons is the exclusive direct production through $q\bar{q}'$ annihilation via the electroweak interaction. The

---

[2] Due to the low (essentially missing) background the fully-leptonic (especially e-μ) decay mode is still suitable for studies of top quark properties.

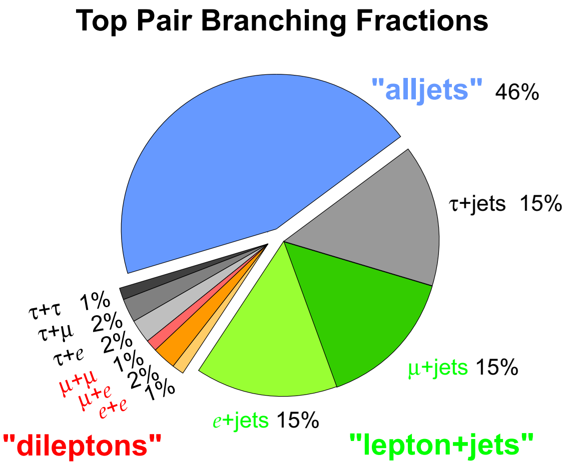

Figure 2.7.: Summary of all possible $t\bar{t}$ decay modes and their branching fractions [67].

corresponding Feynman diagram is shown in Figure 2.8(a). W bosons produced via this leading order process are produced with zero transverse momentum. Including higher orders, W bosons can be produced via processes such as depicted in Figures 2.8(b) and 2.8(c) and thereby obtain transverse momentum. The former one shows a gluon from one proton splitting into a quark-antiquark pair, with one of the two quarks interacting with a quark from the other proton, to create a W boson. The latter one illustrates a process where one incoming quark radiates a gluon before interacting with the quark from the other proton. Examples of Feynman diagrams for processes with two additional partons in the final state are shown in Figure 2.9. It has been shown [68], though at proton-antiproton colliders, that there exists an effective scaling law relating the cross-section for the W+(n+1) partons process to that of the W+n partons one via:

$$\frac{\sigma(W\text{+}(n\text{+}1)\text{ partons})}{\sigma(W\text{+}n\text{ partons})} = \alpha, \tag{2.12}$$

where α is at lowest order related to strong coupling constant α_s.

With the W boson decaying leptonically, the final state, especially with four additional partons, looks exactly as semi-leptonic $t\bar{t}$ events, discussed above. Due to this and the large cross-section of W boson production compared to $t\bar{t}$ production (see σ_W in Figure 2.3), W+Jets events make up the dominant background in a $t\bar{t}$ analysis (using the semi-leptonic channel). Minor differences such as an increased transverse momentum of the W boson in $t\bar{t}$ events compared to the direct production, due to the large top quark mass; an increased scalar sum of the transverse momentum of all jets in $t\bar{t}$ events; or a decreased number of b-tagged jets in W+Jets events; have to be exploited to separate both types of events. These differences in the properties of the W boson also propagate to the final state leptons, where in this example the pseudo-rapidity[3] distribution tends to be more narrow for $t\bar{t}$ events. The analysis presented in Chapter 7 of this thesis is partly utilising this distinction.

---

[3] A definition of pseudo-rapidity follows in Section 3.2.2.

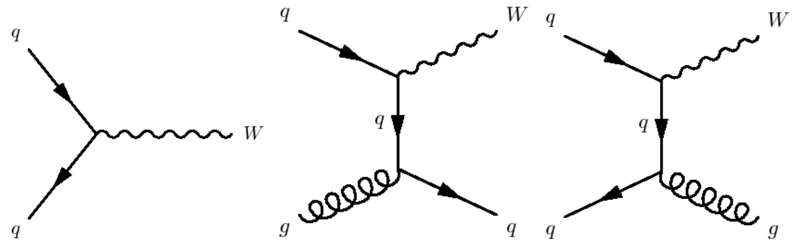

(a) W+0 partons (b) W+1 parton (c) W+1 parton

Figure 2.8.: Feynman diagrams for W boson production at the LHC: (a) for the W+0 partons process; (b) and (c) examples for the W+1 parton process.

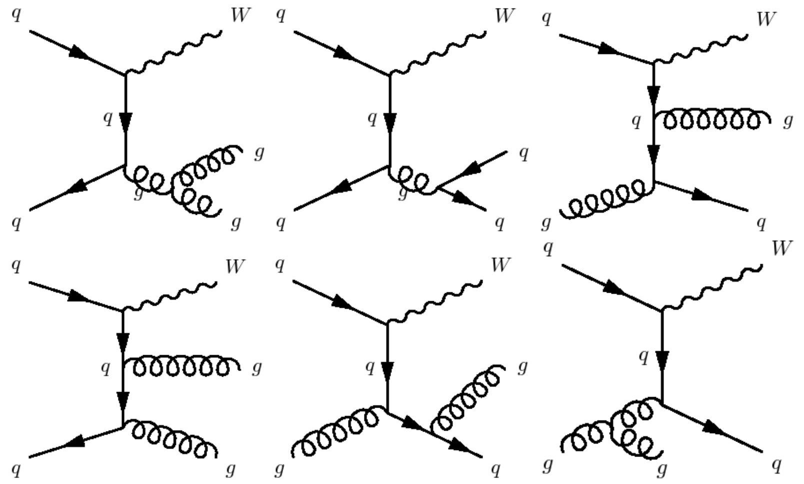

Figure 2.9.: Examples of Feynman diagrams for the W+2 partons process.

2.2.3. Single-Top Events

In case of the leptonic W boson decay single-top production, as introduced in Section 2.1.1, can also feign the semi-leptonic $t\bar{t}$ event signature: one charged lepton, one neutrino (resulting in $E_{\mathrm{T}}^{\mathrm{miss}}$) and at least one bottom quark or an additional light quark, depending on the production channel, accompanied by possible extra partons from QCD bremsstrahlung. Though this topology is possible, the average jet multiplicity in single-top events is expected to be lower than for $t\bar{t}$ events.

2.2.4. QCD-Multi-jet Events

The cross-section for QCD-multi-jet events is the largest at the LHC (see various single jet cross-sections σ_j in Figure 2.3). The mechanism to produce high parton multiplicity events works analog to the W+Jets production via QCD bremsstrahlung, i.e. gluon splitting and gluon emission. Though having no lepton in the hard process these events can still look like leptonic $t\bar{t}$ signatures. This is caused on the one hand by jets containing a large electromagnetic fraction looking like electrons in the detector, caused to a large extend by neutral and charged pions creating electromagnetic clusters ($\pi \to \gamma\gamma$) and tracks, respectively. On the other hand, misreconstruction of jets as well as mismeasurements of the energies of jets and decay products of heavy quarks[4] can lead to missing transverse energy ($E_{\mathrm{T}}^{\mathrm{miss}}$), having the same effect as a neutrino in the final state. Still it is possible to reduce the fraction of events with topologies similar to $t\bar{t}$ events to a level marginal compared to the total cross-section and to that of $t\bar{t}$ production itself.

2.2.5. Z+Jets Events

The Z+Jets production is nearly identical to the W+Jets case. Also because of the larger mass, the cross-section is about a factor ten smaller than for W+Jets. In terms of Z+Jets as a background for $t\bar{t}$ events, the leptonic decay modes can be combed out to a large extend, due to the near perfect reconstruction of the Z boson, with simple cuts on the reconstructed invariant mass of the leptons. An event signature similar to semi-leptonic $t\bar{t}$ events appears only in cases with four or more associated jets and one of the leptons undetected by the experiment, thereby creating missing energy.

---

[4] Leptons from a semi-leptonic quark decay can appear isolated in case the remaining jet is too soft.

Chapter 3.

Experimental Environment

In this chapter the experimental apparatus, used for the studies presented later in this thesis, is described. After an overview on the Large Hadron Collider (LHC) and the connected accelerator complex, the chapter concludes with an outline of the global design concept of the ATLAS experiment. This includes all subdetectors, with an emphasis on those parts of special interest for this thesis.

3.1. The Large Hadron Collider

The Large Hadron Collider (LHC) is a proton-proton collider located at the European Laboratory for Particle Physics (CERN) near Geneva, Switzerland. It is situated in the former Large Electron Positron (LEP) collider [69–71] tunnel with a circumference of about 27 km, between 50 and 100 m under ground. A hadron collider was chosen to overcome the energy limit of the LEP, caused by energy loss due to synchrotron radiation. Since this loss is inversely proportional to the particle mass to the forth, protons, compared to electrons and positrons, can be accelerated to higher energies using the given physical dimensions of the LEP tunnel. High centre-of-mass energies are required for the production of heavy particles such as the top quark, a possible *Standard Model* Higgs boson or those predicted by *new physics* models. Due to the requirement of very high event rates and particle densities, necessary for the discovery of rare processes, a proton-proton collider was chosen in favour of a proton-antiproton machine such as the Tevatron. Whilst the latter technique would allow both beams to be counter-rotating in the same pipe, it has strong limitations on the number of bunches per beam due to beam-beam interactions and on the possible production rate of antiprotons. Since at energies of the LHC, it is to a large extend sea quarks and gluons colliding, there is no significant difference in the physics between both types of colliders. In addition the substructure of the proton leads to collisions of partons with different momentum fractions (see Section 2.1.1), thus covering a large kinematic range, but limiting the knowledge of the precise centre-of-mass energy of the interaction.

The protons are pre-accelerated to an energy of 450 GeV by the existing accelerator facilities at CERN, depicted in Figure 3.1. After the injection into the LHC ring the protons will be further accelerated up to 7 TeV, resulting in a centre-of-mass energy of 14 TeV. However, in the first year of operation only energies of about 7 TeV in the centre-of-mass will be obtained. With the given size of the ring the energy of the protons is limited by the strength of the magnetic field holding the beams inside the ring. A field of 8.33 T

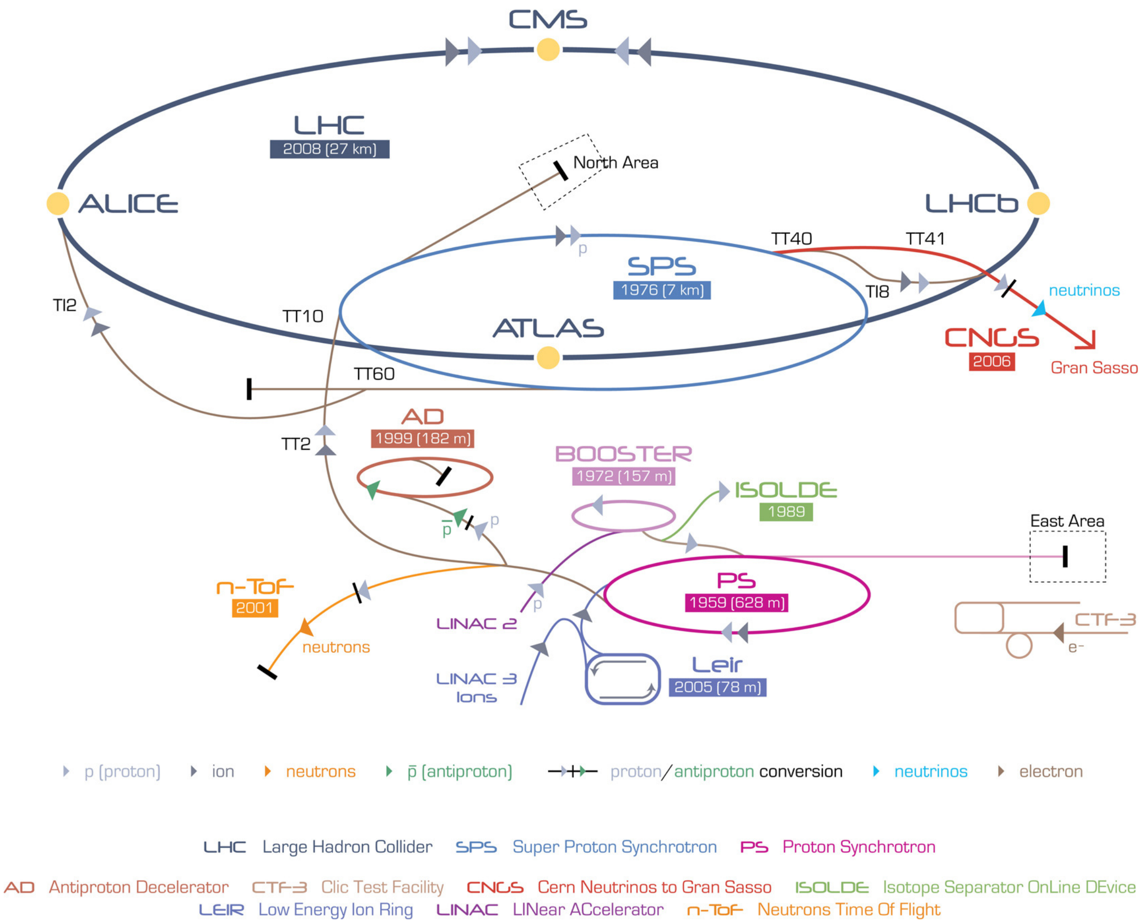

Figure 3.1.: The LHC is the last ring (largest ring) in a complex chain of particle accelerators. The smaller machines are used in a chain to help boost the particles to their final energies and provide beams to a whole set of smaller experiments. The dots imbedded in the large ring indicate the locations of the four main experiments. [72]

has to be produced to cope with 7 TeV protons. A field strength only achievable with superconducting magnets. 1232 superconducting dipole magnets made of niobium-titanium (NbTi) are therefore cooled down to a temperature of 1.9 K using super-fluid helium. At the final design stage 2808 bunches, each counting about 10^{11} particles, are to circulate in the two beams in opposite direction. Every 25 ns the two proton beams are brought into collision at four interaction points, determining the locations of the four main experiments at the LHC (see Figure 3.1). Due to the large number of particles per bunch, more than one collision will occur simultaneously. The resulting overlap is referred to as “pile-up” of events.

As mentioned above, a high event rate R is necessary for the discovery of rare processes, i.e. processes with a small cross-section σ_{int}. The so-called instantaneous luminosity defines the proportionality between both physical quantities:

$$R = L\sigma_{\text{int}}. \tag{3.1}$$

For two bunches with N_1 and N_2 particles colliding at a frequency f, the luminosity can be expressed as:

$$L = f\frac{N_1 N_2}{4\pi\sigma_x\sigma_y}, \tag{3.2}$$

where σ_x and σ_y define the widths of the transverse beam profiles in the horizontal and vertical direction, respectively. In the first year of data taking the luminosity is foreseen to be about 10^{31} cm^{-2} s^{-1} . In the following years it is going to be increased up to the design luminosity of 10^{34} cm^{-2} s^{-1} . To define the size of a data sample one typically refers to the integrated luminosity

$$\mathcal{L} = \int dtL \tag{3.3}$$

instead of simply stating the number of events. One year of data taking at a luminosity of 10^{31} cm^{-2} s^{-1} (10^{34} cm^{-2} s^{-1}) corresponds to about 100 pb^{-1} (100 fb^{-1})[1].

3.2. The ATLAS Detector

The ATLAS (A Toroidal LHC ApparatuS) experiment, illustrated in Figure 3.2, is a so-called general purpose particle physics detector of about 44 m length, 25 m height and a weight of about 7000 tons. In this section the ATLAS detector will be described. After a general overview, the geometry and coordinate system as well as all subsystems will be presented. Special emphasis will be put on systems of interest for this thesis. Still this chapter will not impart full knowledge on all the subsystems of ATLAS, therefore the reader is referred to [73] for a more complete description.

3.2.1. Detector Overview

The overall task of a general purpose detector is to reconstruct the primary interaction. Therefore it is necessary to collect all possible information on the primary vertex as well as on all final state particles passing through the detector. These final states can be of all kind, but mainly due to their lifetime comprise photons, electrons, muons, neutrinos, hadrons (e.g. pions and neutrons) and so-called jets. Jets are narrow cones of mainly hadrons, created by the hadronisation of a quark or gluon, due to QCD confinement [75].

To successfully identify and reconstruct all final states, the ATLAS detector consists of several subdetectors dedicated to specific tasks. Not to loose any information it is build in a cylindrical and forward-backward symmetric design, consisting of a barrel and two end-cap parts. The subdetectors can be categorised in two groups: either they measure the tracks of charged particles and by the help of a magnetic field allow for momentum reconstruction (trackers), or they measure the energy of the particle (calorimeters).

The ATLAS detector is designed in an onion-shell-like structure, as illustrated in Figure 3.3. Different types of tracking detectors are placed in a magnetic field around the interaction point, allowing for the reconstruction of tracks and therefore the measurement

---

[1] Assuming a data taking period of 10^7 s.

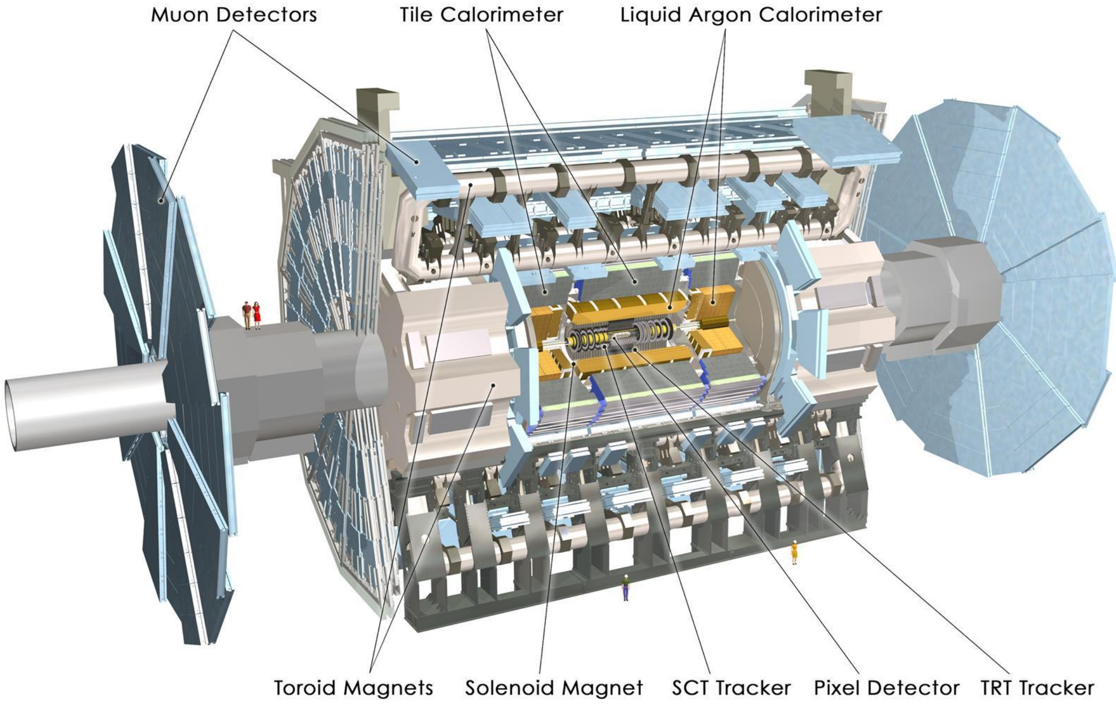

Figure 3.2.: Computer generated image of the whole ATLAS detector. [74]

of the momentum of charged particles. Behind the tracking detectors, the calorimeter system tries to stop both neutral and charged particles and thereby measures their energy. The outermost layer is an additional tracking detector specifically designed for the measurement of the momenta of muons. Since muons are very weakly interacting particles, they will not be absorbed by the calorimeters (in case $p_T^\mu > 5\mathrm{GeV}$).

3.2.2. Geometry and Coordinate System

The ATLAS geometry is defined by a coordinate system having its origin in the nominal interaction point. The z-axis is defined by the anti-clockwise beam direction and the x-y-plane is the one transverse to that. The two halves of the detector separated by the x-y-plane at $z = 0$ are often referred to as A-side and C-side for $z > 0$ and $z < 0$, respectively. The positive x-axis is defined as pointing from the interaction point towards the centre of the LHC ring, while the positive y-axis is pointing upwards. Alternatively, space points can be described by a radial distance $r = \sqrt{x^2 + y^2}$ to the interaction point, a polar angle θ and an azimuthal angle ϕ, measured around the beam axis (in the x-y-plane). The polar angle θ defines the pseudo-rapidity $\eta = -\ln\tan(\theta/2)$, which together with the azimuthal angle ϕ defines the distance ΔR between two objects in the pseudo-rapidity-azimuthal angle space as $\Delta R = \sqrt{\Delta\eta^2 + \Delta\phi^2}$.

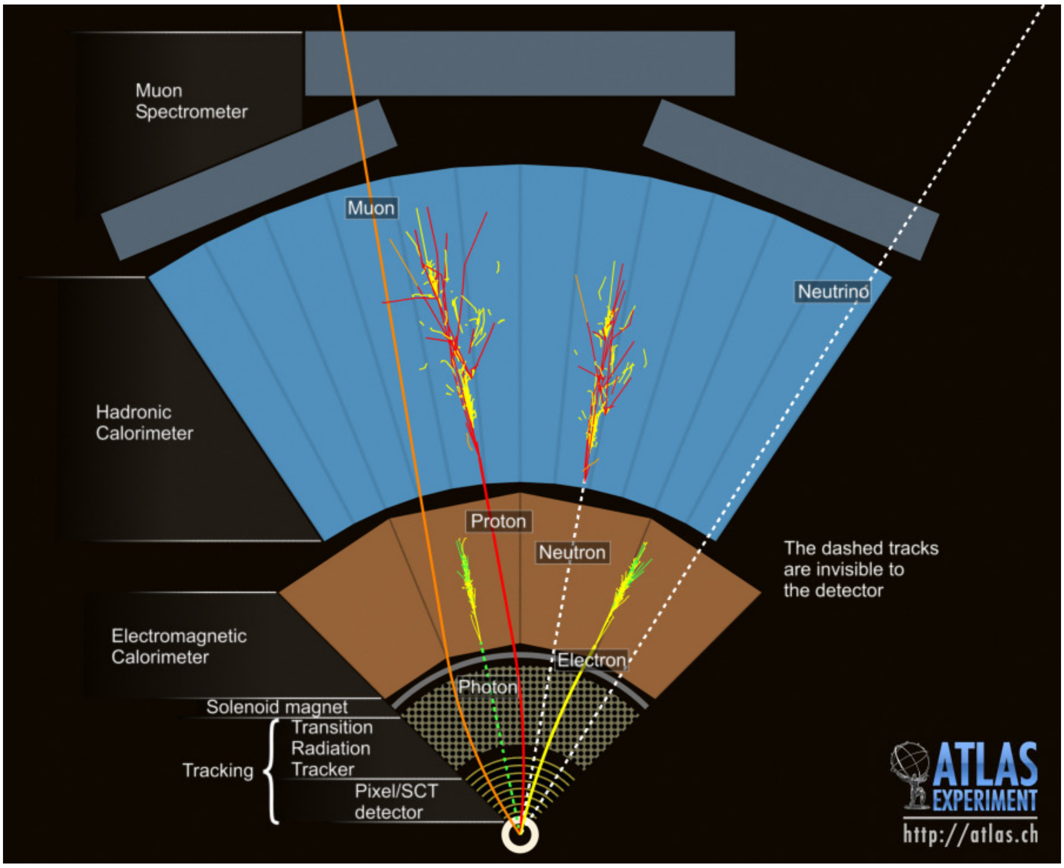

Figure 3.3.: Drawing of a slice of the ATLAS detector, including all sub-systems and illustrating the path of various types of particle through the detector. [76]

3.2.3. Magnet System

The ATLAS magnet system features four major components, a Central Solenoid (CS), a Barrel Toroid (BT) and two End-Cap Toroids (ECT). Aligned on the beam axis, the CS provides a 2 T axial magnetic field for the tracking detectors. The three toroid parts produce a magnetic field of approximately 0.5 T and 1 T for the muon detectors in the central and end-cap regions, respectively. Each of them consists of eight coils located radially and symmetrically around the beam axis.

3.2.4. Inner Detector

The Inner Detector (ID), illustrated in Figure 3.4, utilises two different detector types to provide measurements of the momenta of charged particles, the primary and possible secondary vertices as well as the sign of the electric charge. The inner part of the ID consists of high-resolution semiconductor detectors, whereas the outer part, a straw tube tracker, delivers continuous tracking and particle identification possibilities. The whole system extends over a length of about 6.2 m with a diameter of approximately 2.1 m and is placed in a 2 T solenoidal magnetic field (see Section 3.2.3).

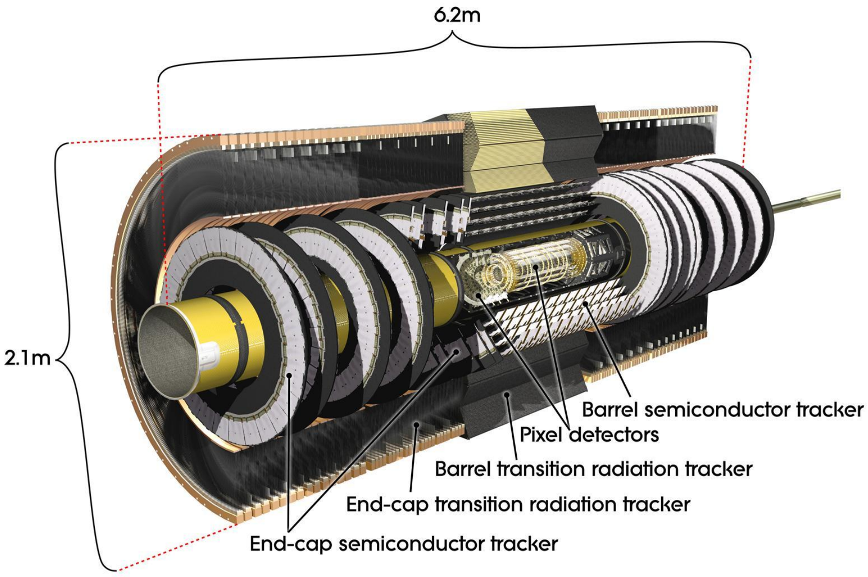

Figure 3.4.: Cut-away view of the ATLAS inner detector. [77]

Pixel Detector

The Pixel Detector, the innermost part of ATLAS, was designed to allow for a precise measurement of the position of the primary as well as possible secondary vertices and to give three precise space points for each track. Therefore it features very high granularity and is placed as close as possible to the interaction point. It consists of three concentric barrel layers (see Figure 3.5) and three discs in each end-cap (see Table 3.1). With its about 80 million readout channels the Pixel Detector amounts for about 90% of the total number of readout channels in ATLAS. Since a detailed analysis of the thermal performance of the Pixel Detector is part of this thesis (see Appendix A), more details are given in the following paragraphs. More information can be found in [73, pp. 53] and [78].

Modules and Sensors The Pixel Detector is composed of 1744 modules, distributed as shown in Table 3.1. A pixel module, as illustrated in Figure 3.6, consists of a stack of the following structural elements (from the bottom up):

- 16 front-end (FE) electronics chips [79, 80] of 180 μm thickness, with 2880 channels each;
- bump bonds (In or PbSn), which connect the FE channels to the pixel sensors;
- a n^+-n-p^+-sensor tile about 250 μm thick;
- a flexible polyimide printed-circuit board (flex-hybrid) with a module-control chip (MCC) glued to it;
- a polyimide pig-tail with a connector (barrel modules) or a wire micro-cable (end-cap modules) bonded to the flex-hybrid.

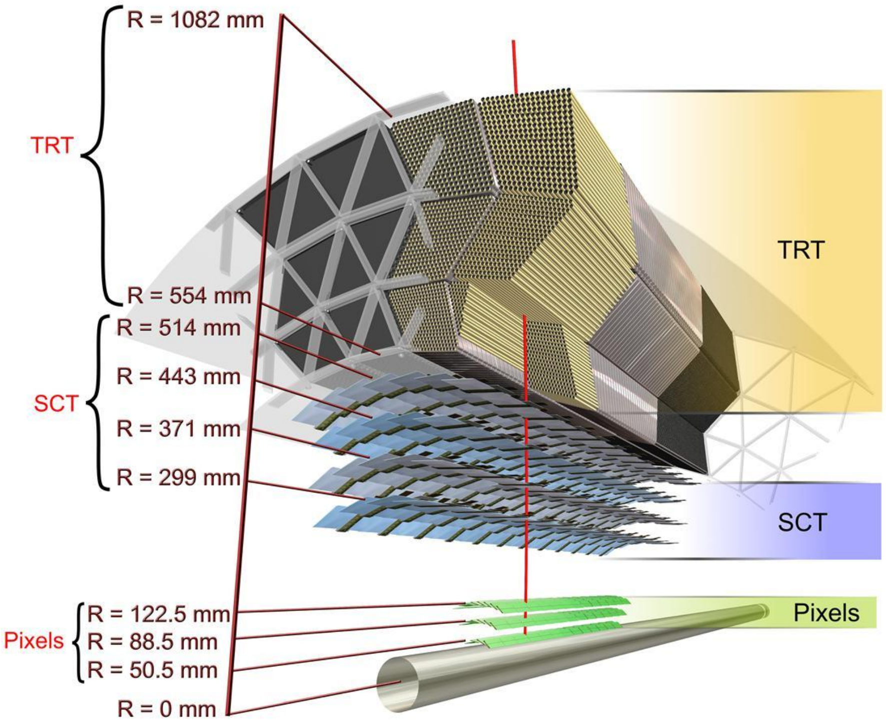

Figure 3.5.: Sensors and structural elements of the Inner Detector barrel part. Starting from centre: the beryllium beam-pipe, the three cylindrical silicon-pixel layers, the four cylindrical double layers of barrel silicon-microstrip sensors (SCT) and the barrel TRT modules within their support structure. [77]

The n^+-n-p^+-sensor technique, combining an oxygenated n-type wafer, readout pixels as n^+ implants on the front side and a p^+ doped back side, has been chosen because of the good charge-collection performance of the n^+ implanted side even after type inversion through irradiation[2], the increased radiation tolerance of highly oxygenated materials and because of the fact that this design allows for charge collection even in partial depletion. The nominal size of the 16×2952 pixels on each sensor is $50 \times 400\ \mu\text{m}^2$. While this applies to about 90% of the pixels, the remaining ones, mainly located at the FE borders, have a size of $50 \times 600\ \mu\text{m}^2$. Each FE also contains 72 ganged pixels, thus leading to a total number of 46080 readout channels per module. The sensors will be operated with an initial bias voltage of about 150 V, which can be increased to above 500 V depending on the level of irradiation during running. To chasten the growth of the effective doping concentration with time and to minimise leakage currents, the sensors operate at temperatures between -5°C and -10°C. The intrinsic hit resolution of the sensors is given by 10 μm in r-

---

[2] The n-type material effectively turns into p-type, due to a change of the effective doping caused by irradiation, after a 1 MeV neutron equivalent fluence F_{neq} of $\sim 2 \times 10^{13}$ cm^2 [73, p. 44/53].

Table 3.1.: Parameters of the Pixel Detector. Number of staves/sectors and modules for each part of the detector. The quoted barrel radii are average values due to the 20°C stave-tilt with respect to a tangent vector. [73]

Barrel	**Radius [mm]**	**Staves**	**Modules**
Layer 0 (L0)	50.5	22	286
Layer 1 (L1)	88.5	38	494
Layer 2 (L2)	122.5	52	676
End-cap (one side)	**z [mm]**	**Sectors**	**Modules**
Disc 1 (e.g. D1A)	±495	8	48
Disc 2 (e.g. D2A)	±580	8	48
Disc 3 (e.g. D3A)	±650	8	48

ϕ and 115 μm in z (r) for the barrel (end-caps) [73]. Within the carbon-fibre made Pixel Support Tube, the modules are mounted (glued) on 112 staves (13 modules each) and 48 sectors (eight per disc, six modules each) in the barrel and end-cap, respectively. Each stave consists of high-stiffness, thermally conducting, carbon-carbon (C-C) laminate plates, an aluminium cooling tube with a flat surface at the interface with the C-C material that supports the modules, and a carbon-fibre composite piece glued to the C-C pieces, capturing the aluminium tube. To guarantee full ϕ coverage the staves, and thereby the modules upon, overlap and are mounted at a tilt angle[3] of 20 degrees. In the end-caps, the sectors are composed of thin C-C faceplates carrying a rectangular aluminium cooling tube.

Readout and Power Supply The signal transmission to the outside is done both electrically and optically. The conversion from the former, using the Low Voltage Differential Signalling (LVDS) standard, to the latter takes place at the optoboards [81] mounted on Patch Panels (PP0s) just outside the pixel package. Hereby each PP0 handles one half-stave with six or seven modules each in the barrel[4] or one sector with six modules in the end-caps. From the PP0s, the signal is transferred directly to the Readout Drivers (RODs), via fibre optical cables. The low-voltage (LV) cables for the analogue and the digital part of the FEs as well as the high-voltage (HV) cables for the pixel sensor depletion voltage and the cables connected to the Detector Control System[5] (DCS) [82] are routed via the PP0 and up to three more Patch Panels (PP1, PP2 and PP3) as illustrated in Figure 3.7. The different types of cables are chosen for each section based on a compromise between radiation length of the material in use and the powering efficiency. Default values for all voltages and currents are shown in Table 3.2.

Cooling System During the first years, the cooling system has to remove about 24 kW of power dissipation from the Pixel Detector. To master this task two different cooling

---

[3] The angle to the tangent to the support cylinder surface in the x-y-plane.

[4] Alternating in ϕ, staves are separated into half-staves of six and seven modules connected from opposite sides (A/C) of the detector.

[5] In previous experiments often referred to as 'Slow Control'.

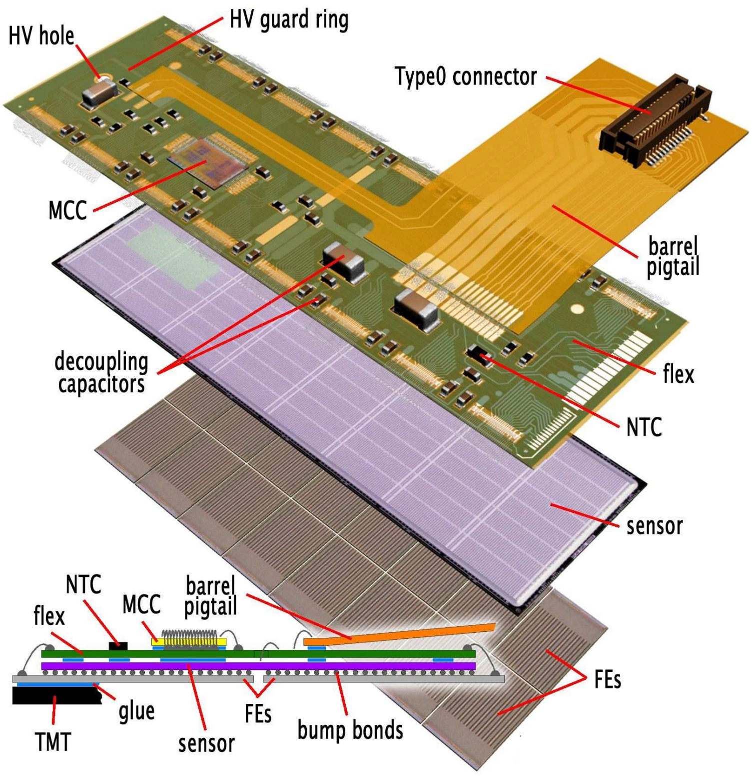

Figure 3.6.: Schematic view of a barrel pixel module (top) illustrating the major pixel hybrid and sensor elements, including the MCC (module-control chip), the front-end (FE) chips, the NTC thermistors, the high-voltage (HV) elements and the Type0 signal connector. Also shown (bottom) is a plan view showing the bump-bonding of the silicon pixel sensors to the polyimide electronics substrate. [73]

systems are used in the Pixel Detector. While the cables and Patch Panels outside of the ID volume (PP2) are cooled by a standard mono-phase cooling system, using a room-temperature C_6F_{14} fluorinert coolant, the detector itself is cooled using an evaporative cooling system. The coolant of choice for the evaporative cooling system is non-flammable, electrical non-conductive, chemically inert and radiation stable octafluoropropane (C_3F_8). Most of the 88 Pixel Detector cooling circuits (loops) serve either two staves (26 modules) forming a bi-stave in the barrel or two sectors (12 modules) forming a bi-sector in the end-caps. Eight of the loops are dedicated to cooling each 36 of the optoboards situated at PP0. Each individual cooling circuit has a fixed flow. The coolant, arriving at the detector at room temperature, in liquid form at an absolute pressure of 11 to 14 bar absolute, is delivered by four distribution racks, each serving one quadrant[6] of the ID. The delivery pressure is regulated at the distribution racks by pneumatically-controlled pressure regulators (PR). By guiding the liquid through a small-diameter capillary the pressure starts to fall and the coolant emerging from the capillary, now in two-phase form, starts to boil, thereby lowering the temperature of detector modules connected to the

---

[6] Quadrants (Q1-Q4) and also octants (O1-O8) define clockwise numbered (following the azimuthal angle ϕ) detector segments in the x-y-plane.

Table 3.2.: List of characteristic voltages and currents along with their default values for barrel (end-cap) modules. Currents in brackets denote the values for unconfigured modules.

Level	**Name**	**Explanation**	**U [V]**	**I [mA]**
Module	HV	depletion voltage for sensors	150 to 600	$O(\mu\text{A})$
	VDD	digital voltage for FEs and MCCs	2.1 (2.0)	$\sim$700 [$\sim$350]
	VDDA	analogue voltage for FEs	1.7 (1.6)	$\sim$1200 [$\sim$80]
PP0	VVDC	optoboard supply voltage	6	260
	VPin	optoboard PIN diode[a]	10	3.5
	VISet	optoboard laser power	0.9	1

[a] Positive-Intrinsic-Negative diode

thin-wall cooling structures. The evaporation temperature, set by the pressure of the coolant, is regulated by a pneumatically-controlled back-pressure regulator (BPR) in the exhaust line. Further details on the Pixel Detector cooling system can be found e.g. in [73]. A detailed study on the thermal performance of the Pixel Detector is presented in Appendix A.

It has to be noted that half of the Layer-2 cooling loops have an additional cooling pipe inserted into the normal cooling pipe, due to a corrosion problem only detected after the production of the first batch of staves. This affects in total 26 staves always located at the inlet side of the Layer-2 cooling loops. Also three circuits in the end-caps (17, 66 and 71) have been switched off during the 2008 operation period due to leaks, not allowing for reliable conditions.

Nomenclature To locate modules within the Pixel Detector a naming scheme using the following conventions is used for the barrel and the end-caps, respectively:

$$\text{L\#}_1\text{\_B\#\#}_2\text{\_S\#}_3\text{\_\#}_4\text{\#}_5\text{\_M\#}_6, \qquad \text{D\#}_1\text{\#}_4\text{\_B\#\#}_2\text{\_S\#}_3\text{\_M\#}_6.$$

Hereby $\#_1$ denotes the layer/disc, $\#\#_2$ the bi-stave/bi-sector, $\#_3$ the stave/sector, $\#_4$ indicates the side (A/C) on which the PP0 is located, while $\#_5$ and $\#_6$ state the number of modules on a given stave (in the barrel only) and the module-id, respectively. To locate a PP0 the last item is neglected. Since the module-id is counted from the centre of the detector towards the end-caps starting with zero, L2_B3_S1_C7_M0 would point to the central module of the first stave on bi-stave number three in Layer 2. C7 suggests that the connected PP0 (L2_B3_S1_C7) handles seven modules in this case.

Semiconductor Tracker

The Semiconductor Tracker (SCT), positioned in the intermediate radial range in the ID, is build out of four double layers of silicon microstrip detectors (see Figure 3.5). Each of these 6.4 cm long[7] p-on-n detectors, is designed to provide a precise measurement of the r-ϕ coordinates, when aligned to the beam axis. Modules of four detectors, with

---

[7] The width varies between 5.4 and 6.6 cm depending on the module type (placement).

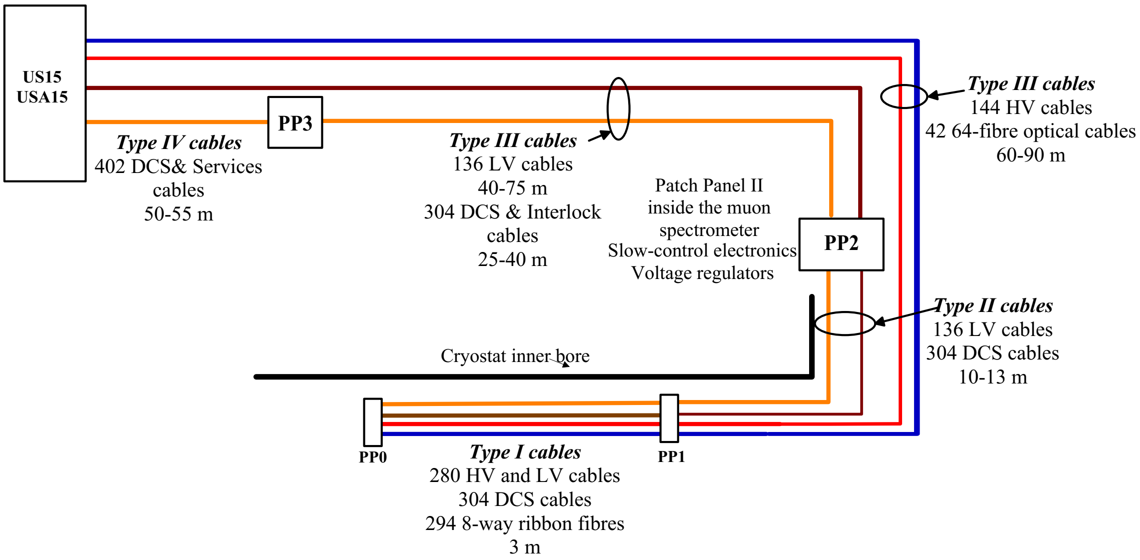

Figure 3.7.: The routing of data links (red) and power supply cables (high voltage: blue, low voltage: brown, DCS and services: orange) from each side of the pixel detector to the off-detector electronics and power supplies in the service caverns, together with the number, type and utilisation of the cables and optical links. [73]

two daisy-chained and rotated by a 40 mrad angle with respect to the other two, allow for an additional measurement of the z coordinate. In the end-cap region, the modules are distributed over nine discs on each side with one set of detectors with strips running radially and one set of stereo strips at an angle of 40 mrad. A total of 4088 modules (2112 barrel and 1976 end-caps) add up to approximately 6.3 million readout channels. With a coverage of $|\eta| \leq 2.5$ an intrinsic hit resolution of 17 μm in r-ϕ and 580 μm in z and r is reached for each barrel and end-cap module, respectively.

Transition Radiation Tracker

The outermost part of the ID is the Transition Radiation Tracker (TRT). The TRT is a straw-tube detector combined with transition-radiation detection. Each of the approximately 300,000 straws acts as a small proportional drift-chamber with a hit resolution of 130 μm in r-ϕ. The 4 mm diameter straws are filled with a gas mixture of Xe (70%), CO_2 (27%) and O_2 (3%) to allow both for optimal drift properties and the detection of transition radiation, created by relativistic particles in the radiator material interleaved between the straws. In the barrel region, straws with a length of 144 cm are arranged parallel to the beam axis and split in half to reduce the occupancy and readout at each end (see Figure 3.5). Here the radiator consists of foam-like polypropylene fibres squeezed between the straws. In the end-cap region straws of 37 cm length are arranged radially in nine wheels, interleaved with regular polypropylene foils. The total number of readout channels is approximately 351,000. The TRT enables to measure tracks with a long lever arm over a range of $|\eta| \leq 2.0$.

Since transition radiation only occurs for relativistic particles with a Lorentz factor $\gamma =$

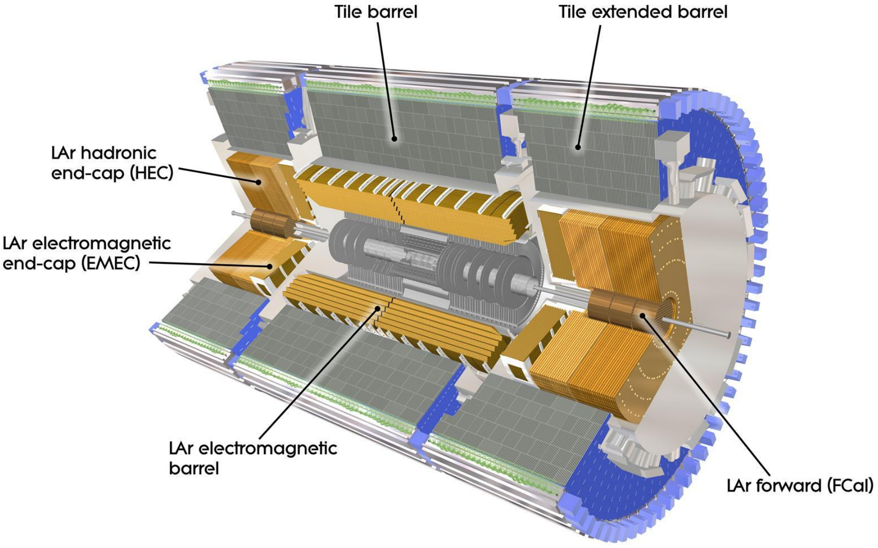

Figure 3.8.: Cut-away view of the ATLAS calorimeter system. [84]

E/mc^2 above 1000, which is essentially only fulfilled for electrons, the TRT allows for the separation between electrons[8] and hadrons (mainly pions), at highly relativistic energies. Further details on the issue of particle identification in the TRT can be found in [83].

3.2.5. Calorimetry

Outside of the Central Solenoid magnet two kinds of calorimeters measure the position and energy of charged and neutral particles over a range of $|\eta| \leq 4.9$. Figure 3.8 illustrates both the Electromagnetic Calorimeter (EMC) and the Hadronic Calorimeter (HC).

Electromagnetic Calorimeter

The EMC is a lead liquid argon (LAr) sampling detector built in an accordion-shaped geometry to provide full ϕ symmetry. Made of alternating layers of lead (absorber) and LAr (active material), it consists of a barrel part ($|\eta| \leq 1.475$) and two coaxial end-cap wheels on each side (outer wheel: $1.375 \leq |\eta| \leq 2.5$, inner wheel: $2.5 \leq |\eta| \leq 3.2$). To provide good containment for showers originating from electrons and photons the EMC has a total thickness of above 22 radiation lengths[9] (X_0) in the barrel and above 24 X_0 in the end-caps. Up to the outer wheel, matching the coverage of the ID, the EMC is segmented into three radial (longitudinal) sections called samplings in the barrel (end-cap) part, as illustrated in Figure 3.9. The first sampling acts as a pre-shower detector for photon separation. It has the highest granularity and a depth of about 4.3 X_0. With a

---

[8] Here and in the following this includes positrons if not stated otherwise.

[9] The mean distance over which a high-energy electron loses all but $1/e$ of its energy or $7/9$ of the mean free path for e^+e^--pair production by a high-energy photon.

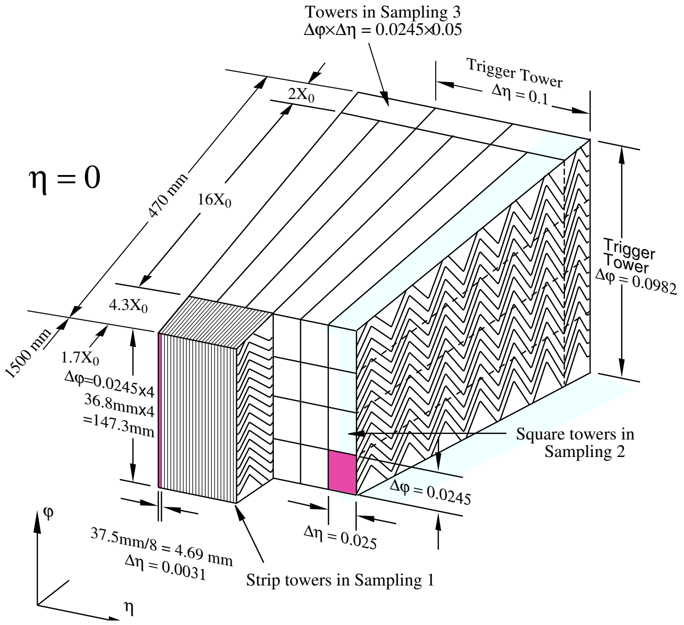

Figure 3.9.: Illustration of an Electromagnetic Calorimeter barrel section along with the cell granularity in η and ϕ of the three different layers. [85]

depth of about 16 X_0 the second sampling is the largest section of the EMC and therefore most of the energy will be deposited here. Its granularity is reduced by a factor of about eight in η while increased by a factor of four in ϕ, with respect to the first sampling. This granularity of $\Delta\eta \times \Delta\phi = 0.025 \times 0.025$ allows for a precise position measurement in the range of $|\eta| \leq 2.5$. Due to the wide spread of electromagnetic showers in the last and third sampling (2 X_0), its η granularity is further reduced by a factor of two compared to the previous section (see Figure 3.9). To correct for the loss of energy in the ID and the cryostat an additional pre-sampler is added in front of the EMC in the range of $|\eta| \leq 1.8$. The energy resolution of the EMC is $\sigma_E/E = 10\%/\sqrt{E[\text{GeV}]} \oplus 0.7\%$ [73].

Hadronic Calorimeter

The ATLAS Hadronic Calorimeter (HC) system, directly following the EMC, is illustrated in Figure 3.8. It is composed out of four subsystems, using two different calorimeter techniques. The barrel and extended barrel calorimeters (Tile), covering a range of $|\eta| \leq 1.7$, are made of alternating scintillating plastic (active material) and iron (absorber) tiles. Due to the higher radiation level at large η, the hadronic end-cap calorimeter (HEC) and the forward calorimeter (FCAL) use the LAr technique, with absorbers made of copper or a copper-tungsten, respectively. HEC and FCAL cover ranges of $1.5 \leq |\eta| \leq 3.2$ and $3.1 \leq |\eta| \leq 4.9$. With depths of approximately 9.7 interaction lengths[10] (λ) in the Tile and HEC part and about 11 λ in the FCAL, the HC is able to minimise the number

---

[10] The mean free path of a particle before undergoing an interaction that is neither elastic nor quasi-elastic (diffractive), in a given medium.

of hadrons reaching into the muon system and provides good resolution (Tile and HEC: $\sigma_E/E = 50\%/\sqrt{E[\mathrm{GeV}]}\oplus 3\%$, FCAL: $\sigma_E/E = 100\%/\sqrt{E[\mathrm{GeV}]}\oplus 10\%$ [73]) for high-energy jets.

3.2.6. Muon System

The Muon System (MS) shown in Figure 3.10 is the outermost subsystem of the ATLAS detector, essentially only reached by muons, due to the upstream material. It is instrumented with separate trigger and high-precision tracking chambers using four different types of detectors. Based on the magnetic deflection of muon tracks in the large superconducting air-core toroid magnets (see Section 3.2.3) the MS allows a stand-alone measurement of the muon momenta, which can be combined with a measurement made in the ID. Over most of the pseudo-rapidity range ($|\eta| \leq 2.7$, $|\eta| \leq 2.0$ for innermost layer) the track measurement is performed by Monitored Drift Tubes (MDTs). At large pseudo-rapidities ($2.0 \leq |\eta| \leq 2.7$), Cathode Strip Chambers (CSCs) are used, mainly due to higher rates and background conditions. The MDTs are mechanically isolated aluminium drift tubes, each 30 mm in diameter and filled with a gas mixture of Ar (93%) and CO_2 (7%), with a central W-Re wire. The CSCs are multi-wire proportional chambers with cathode strip readout, offering a higher granularity. The average drift-times, between 30 ns for the CSCs and 300 ns for the MDTs, are larger than the expected time between two successive interactions (25 ns), therefore these detector types can not be used for fast trigger decisions. Thus the two remaining detector types compose a dedicated trigger system covering a range of $|\eta| \leq 2.4$. Three concentric cylindrical layers of gaseous parallel electrode plate detectors, called Resistive Plate Chambers (RPCs), cover a range of $|\eta| \leq 1.05$, while the pseudo-rapidity range up to $|\eta| \leq 2.7$ ($|\eta| \leq 2.4$ for trigger) is covered by Thin Gap Chambers (TGCs), slightly modified multi-wire proportional chambers. Both systems provide drift-times of around 10 ns and therefore allow for fast decisions and measure the muon coordinate in the direction orthogonal to the one obtained by the MDTs and CSCs. The spatial resolution of the different subsystems is: 35 μm in z for the MDTs, 40 μm in R and 5 mm in ϕ for the CSCs, 10 mm in z and ϕ for the RPCs and 2-6 mm in R and 3-7 mm in ϕ for the TGCs.

3.2.7. Forward Detectors

In addition to the main ATLAS detector systems described in the previous sections, three smaller sets of detectors cover the forward region of ATLAS. About ±17 m from the interaction point, the LUCID (LUminosity measurement using Cerenkov Integrating Detector [87]) detector acts as the main relative luminosity monitor for ATLAS, by detecting inelastic proton-proton scattering in the forward direction. The second system, the Zero-Degree Calorimeter (ZDC), located where the LHC beam-pipe is divided into two separate pipes at ±140 m, is mainly used to detect forward neutrons in heavy-ion collisions. The third component, at a distance of ±240 m, is the ALFA (Absolute Luminosity for ATLAS [87]) detector. It consists of scintillating fibre trackers located inside Roman pots which can be moved as close as 1 mm to the beam and provides a measurement of the absolute luminosity in the Coulomb interference region.

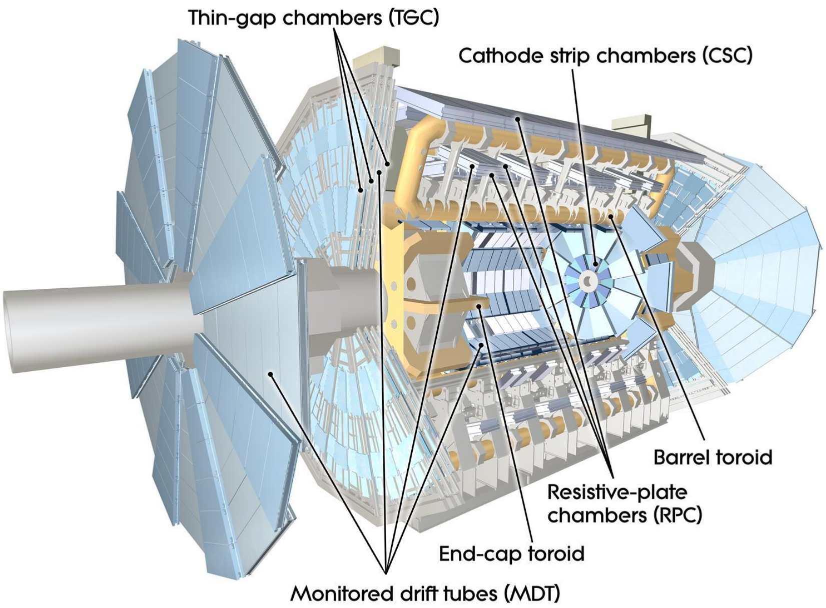

Figure 3.10.: Cut-away view of the ATLAS muon system. [86]

3.2.8. Trigger System

To obtain substantial event numbers to reach the physics goals of ATLAS and the other experiments, the LHC was designed to operate with a bunch-crossing rate of 40 MHz. In contrast to this, the highest achievable rate to read out the about ninety million channels of ATLAS is about 75 kHz, while writing the data to storage is further limited to 200 Hz. To achieve the task of reducing the initial rate while selecting all *interesting* events ATLAS utilises a three-stage trigger system. Level 1 (LVL1) [88] is hardware-based and directly integrated into the detector-electronics. Level 2 (LVL2) and Event Filter (EF), collectively referred to as High-Level Trigger (HLT) [89], are based on software algorithms running on dedicated computing farms. Each level refines the selection made on the previous level and applies additional selection criteria where needed.

Level 1

With an input rate of 40 MHz the Level-1 (LVL1) trigger must take a decision within 2.5 μs to reduce the rate to 75 kHz (about 40 kHz at start-up). It has dedicated access to reduced-granularity information from the calorimeters ($\Delta\eta \times \Delta\phi = 0.1 \times 0.1$, compare to 3.2.5) and the Muon System. The LVL1 calorimeter decision is based on multiplicities and energy thresholds of: electromagnetic clusters, taus, jets, missing transverse energy[11] ($E_{\mathrm{T}}^{\mathrm{miss}}$), scalar sum E_{T} ($\sum E_{\mathrm{T}}$) and the total transverse energy of jets ($\sum^{\mathrm{N_{jets}}} E_{\mathrm{T}}$). The

---

[11] Where transverse energy denotes the transverse component of a vector pointing back from the energy deposition in the calorimeter to the interaction vertex, with magnitude defined by the amount of energy deposited.

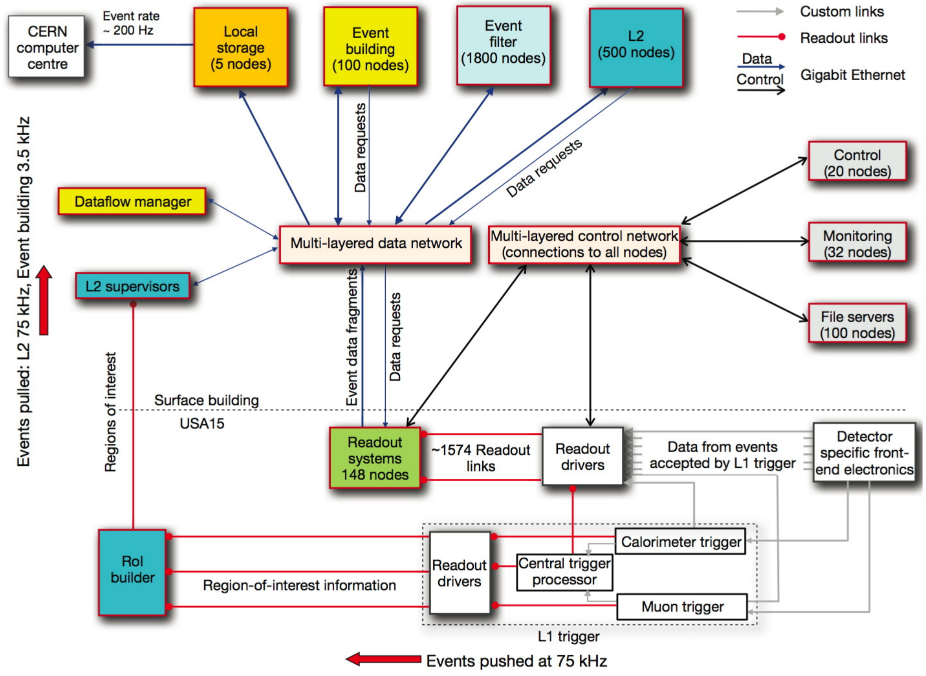

Figure 3.11.: Block diagram of the ATLAS trigger and data acquisition systems. [73]

selection of muons is based on multiplicities of transverse momentum (p_T) thresholds[12], obtained by only the RPCs and TGCs of the Muon System. If accepted by the LVL1 trigger the event data is moved through the Readout Driver (ROD) into the Readout Buffer (ROB), acting as a temporary storage.

Level 2

The Level-2 (LVL2) trigger decision is largely based on regions seeded by the LVL1 trigger accepts. These so-called Regions-of-Interest (ROI's), defined by a p_T threshold and an η-ϕ position, are analysed in full granularity. With only about two percent of the full detector data, given by the data in the ROI's, LVL2 is able to reduce the event rate to below 3.5 kHz, using an average processing time of approximately 40 ms per event.

Event Filter

The final online selection is carried out by the Event Filter (EF). Seeded by LVL2 accepts the EF has direct access to the complete event data and typically uses the same algorithms as the offline reconstruction. It reduces the input rate of 2 kHz (1 kHz) coming from the

---

[12] The number of particles measured with a p_T above the certain value (threshold).

LVL2 in nominal (start-up) conditions to about 200 Hz, roughly 300 MB/s, with an average event-processing time of 4 s.

Nomenclature for Trigger Items and Chains

In ATLAS trigger chains define the connection of trigger items on one level to those of other levels. While an item usually only has one connection on a previous level it can have several on a subsequent level. The naming of trigger items used within ATLAS and in this thesis thereby adopts the following scheme:

$$\#_1\_[\#_2]\#_3\#_4[\#_5] \quad \text{e.g. L1\_2EM25I or EF\_j35},$$

where $\#_1$ defines the trigger level in a two-character notation (L1, L2 or EF), $\#_2$ specifies the required multiplicity (optional integer, if not given set to one), $\#_3$ sets the type of the requested object (e.g. EM, J, XE for electromagnetic clusters, jets and missing energy, respectively), $\#_4$ determines the threshold (integer in GeV) and $\#_5$ decides whether an isolation is needed or not (optional)[13]. So the first stated L1_2EM25I trigger item is fulfilled if and only if an event at LVL1 contains at least two isolated electromagnetic clusters with at least 25 GeV transverse energy each, while the L2_J35 item requires at least one jet with at least 35 GeV transverse energy at LVL2. To ask for higher multiplicities with different threshold several items can be combined such as:

$$\text{L2\_4J25\_L2\_3J35}.$$

An event will only be accepted by this item if it contains at least three jets with a minimum transverse energy of 35 GeV and one additional with 25 GeV. The definition of trigger chains is given in a so-called trigger menu[14] and can be written e.g. as:

$$\text{L1\_3J20}\rightarrow\text{L2\_3j30}\rightarrow\text{EF\_3j40},$$

which implies that an event can only be accepted by this trigger chain in case all three items have accepted the event.

Prescale and Pass-Through

To be able to analyse data from trigger items with too large rates to store, the trigger system allows to introduce prescale factors. A prescale factor N defines that only one out of N events passing a certain trigger condition is really accepted and processed further. Prescales can be applied on all three levels of the ATLAS trigger system.

In addition, certain items can be set to *pass-through*, on one or more levels. In *pass-through*, each event is accepted through this item in any case. This feature is mainly used to study the performance of one specific level in a given trigger chain and therefore usually implies that two out of three levels are in this mode.

---

[13] $\#_3$ and $\#_5$ are stated as upper-case characters at LVL1 and lower-case characters at LVL2 and EF.

[14] Collections of trigger chains, usually defined for specific beam conditions, such as different luminosities or beam energies.

Chapter 4.

Monte Carlo Samples

Monte Carlo (MC) simulations are an essential part of data analyses in experimental high energy physics. Implying all knowledge about the physics and the experiment, MC simulations try to emulate the outcome of particle collision as realistic as possible. Common MC simulations in particle physics consist of three parts: Event Generation, Detector Simulation and Event Reconstruction. Various algorithms for each of the three parts are implemented in a common ATLAS software framework, called Athena [90], and will be discussed briefly in this chapter, following References [43, 91, 92]. The technique of PDF re-weighting as well as all MC samples used for the analyses presented later in this thesis are detailed at the end of this chapter. With the LHC not having produced any data suitable for the analyses presented in this thesis, MC data are the only data available. Once data taking has started, each step in the production of the MC simulation has to be corrected for and adjusted to the real data.

4.1. Event Generation

Based on theoretical predictions, MC simulation tools, used for the process of Event Generation, try to mimic the collision processes taking place in a real experiment as closely as possible. In general these tools can be divided into two types of codes: event generator codes and cross-section integrators. Both approaches are based on the knowledge of the parton-level cross-section formula of the process in question, e.g. Equations (2.5) or (2.6) for top quark pair production via the strong interaction, and a few common initial steps. In a first step, the phase space, spanning all degrees of freedom of the problem (i.e. the cross-section formula), is identified. This is followed by a step choosing values for each degree of freedom from a uniformly distributed random number generator, thereby defining a so-called candidate event. In a third step, the differential cross-section or event weight of this candidate event is derived, again utilising the cross-section formula. To derive physical predictions from these candidate events, cross-section integrators and event generator codes exploit different approaches. Cross-section integrators, on one hand, produce histograms representing physical distributions by using the event weights calculated in the previous step. In the limit of infinite statistics these are identical with the ones predicted by the cross-section formula, while individual events have no physical meaning. Event generator codes, on the other hand, utilise a so-called *un-weighting* technique to distribute the events as theoretically predicted. In this approach, individual events correspond to single observable measurements, produced at a frequency predicted by theory.

Even though physical information can be extracted by using the techniques addressed above, the process described by the cross-section formula itself remains non-physical. This is due to the fact that, at a hadron collider such as the LHC, neither the incoming partons can be prepared nor the outgoing partons can be detected as isolated particles. Higher-order effects such as initial- and final-state radiation both from QED and QCD as well as hadronisation effects have to be accounted for.

To address hadronisation effects, describing the parton-hadron/hadron-parton transition, one can either use a QCD-improved version of the factorisation theorem described in Section 2.1.1 or use phenomenological, non-perturbative models. The latter technique is exploited by so-called showering and hadronisation generators, such as PYTHIA [93] and HERWIG [94]. Starting with a leading order hard subprocess, higher order effects are included by means of a parton shower, allowing partons to split into pairs of other partons, which themselves can split again until a cut-off energy is reached. The partons resulting from this shower are then grouped into colour-singlet hadrons and short-lived resonances are decayed subsequently. The phenomenological models used for hadronisation as well as parameters such as the cut-off energy are tuned to experimental data. In a last step the underlying event structure; including beam remnants, interaction with other partons within the colliding protons, and collisions of additional protons in the same bunch crossing (pile-up); is added to the event. In this final step the simulation of beam remnants and parton interaction within the colliding protons can also be carried out by dedicated tools such as Jimmy [95].

One possible approach to address higher-order corrections in perturbation theory, pursued by so-called Tree Level Matrix Element generators such as AcerMC [96] and ALPGEN [97], is by exact fixed-order computations only of diagrams corresponding to the emission of real particles, thereby neglecting all virtual contributions, e.g. from loop diagrams. This approach has the disadvantage of introducing a cut on the parton level, necessary to avoid soft and collinear singularities in the tree-level matrix elements, that influences the physical observables. Commonly, Tree Level Matrix Element generators are used in combination with showering and hadronisation generators, taking separate care of hard-process computation and the soft and collinear emission, respectively. A more detailed description of this so-called matching procedure is given in Section 4.5.2.

A more advanced approach that combines a NLO Matrix Element generator, taking into account both real and virtual emissions at NLO, and a parton shower programme, is pursued by the MC@NLO [98] event generator. Special care is taken while merging the soft and collinear and the hard emission, to avoid double counting of portions of phase space, due to overlaps between higher-order processes and parton showers.

Most available MC generators do not employ the latest theoretical calculations and precision, e.g. by not including higher-order corrections. A common procedure, to compensate for this, exploits the fact that the shape of kinematic distributions remains relatively constant, while only the overall normalisation has to be corrected. So-called K-factors are introduced to scale MC samples to the desired normalisation, usually taken from the most precise calculation available. K-factors used for the MC samples employed in this thesis are given below.

4.2. Detector Simulation

In the step of Detector Simulation the detector response to the events generated previously is simulated. In the so-called ATLAS Full Simulation embedded within Athena via the GEANT4 simulation toolkit [99], this implies a precise description of the detector geometry (position, dimension and material of all detector parts) as well as a detailed simulation of the various physics processes, caused by the interaction of the particles with the detector material. This includes processes ranging from energies of a few eV, such as the ionisation in gases, up to TeV energies, to provide a detector-response model as realistic as possible. Due to this high level of sophistication these simulations are commonly the most time-consuming step in the production of Monte Carlo samples. Depending on the physics process in question and the necessary amount of simulated events, Athena provides Fast Simulation tools, such as ATLFAST [100, 101] and ATLFASTII [102], using simplified parametrisations and smearing routines as well as look-up tables to simulate parts or all of the detector response. In a subsequent Digitisation step, the previously obtained information is processed in order to emulate the detector electronics output one would expect from the real experiment.

For the purpose of this thesis only samples using the ATLAS Full Simulation have been used.

4.3. Event Reconstruction

The Event Reconstruction is carried out in two sequential steps. In a stand-alone reconstruction step, only information from a single subsystem is used to reconstruct objects such as track segments in the Muon System or the $E_{\mathrm{T}}^{\mathrm{miss}}$-vector from the calorimeters. In the following combined reconstruction step, these information are combined, e.g. by matching track segments of the Muon System to those in the ID, to provide an accurate measurement and identification of final state objects, such as photons, leptons and jets. Details on the reconstruction of these objects will given in Chapter 5.

4.4. PDF Re-weighting

Since the production of fully simulated MC samples is very time consuming, it is not feasible to produce samples for every available PDF set at various energies. To still be able to evaluate uncertainties due to and differences between various PDF sets or centre-of-mass energies, PDF re-weighting techniques can be exploited. Even though these techniques are by far not exact they still give reasonable results within acceptable time scales. In the following, PDF re-weighting techniques, also utilised in the analyses presented in this thesis, are explained in more detail. For the implementation of both techniques the Les Houches Accord PDF Interface [103, 104] was used.

4.4.1. Re-weighting between PDF Sets

The re-weighting of samples created with one specific PDF set $f_{i,j}^{\text{old}}$ to another PDF set $f_{i,j}^{\text{new}}$, can be useful to estimate the uncertainty of a result due to the uncertainties within the PDF set of choice. It can also help to understand the influence of and the difference between various PDF sets. To re-weight MC events from one set to another, one weights each event with a factor w_{PDF}, given by:

$$w_{\text{PDF}} = \frac{f_i^{\text{new}}(x_i, \text{f}_i, \mu^2) \cdot f_j^{\text{new}}(x_j, \text{f}_j, \mu^2)}{f_i^{\text{old}}(x_i, \text{f}_i, \mu^2) \cdot f_j^{\text{old}}(x_j, \text{f}_j, \mu^2)}, \tag{4.1}$$

with both PDFs being functions of the momentum fractions $x_{i,j}$ and the flavours $\text{f}_{i,j}$ of the incoming partons i and j as well as the factorisation scale μ^2. The latter one is given, depending on the process, by:

$$\mu^2 = (m^{\text{X}})^2 + (p_T^{\text{X}})^2 \tag{4.2}$$

in case of W, Z and single-top production (with X=W, Z or t) and

$$\mu^2 = \frac{(m^t)^2 + (m^{\bar{t}})^2}{2} + \frac{(p_T^t)^2 + (p_T^{\bar{t}})^2}{2} \tag{4.3}$$

in case of $t\bar{t}$ production (with $m^t = m^{\bar{t}}$).

4.4.2. Re-weighting between Energies

To re-weight MC events created at one specific centre-of-mass energy $\sqrt{s}^{\text{old}}$ to another $\sqrt{s}^{\text{new}}$, one applies a weight factor w_E, similar to the previous section, given by:

$$w_E = \frac{f_i(x_i/R, \text{f}_i, \mu^2) \cdot f_j(x_j/R, \text{f}_j, \mu^2)}{f_i(x_i, \text{f}_i, \mu^2) \cdot f_j(x_j, \text{f}_j, \mu^2)} \cdot \frac{1}{R^2}, \tag{4.4}$$

with $R = \sqrt{s}^{\text{new}}/\sqrt{s}^{\text{old}}$ being the ratio of the desired energy divided by the one the sample was produced at. In the specific case of re-weighting from $\sqrt{s}^{\text{old}} = 10$ TeV to $\sqrt{s}^{\text{new}} = 7$ TeV this yields a ratio of $R = 7/10$.

4.5. Specific Monte Carlo Samples

At the time of performing the analyses presented in this thesis, the energies of both beams were expected to be 5 TeV, therefore most of the ATLAS MC samples have been redefined and regenerated for physics studies at 10 TeV, in contrast to the 14 TeV at the LHC design energy. These samples are commonly referred to as the ATLAS MC08 production, while 14 TeV samples are know as CSC (Computing System Commissioning) samples. During the process of writing this thesis it was decided, mainly to ensure safe operation of the LHC, to further limit the available energy to 3.5 TeV per beam. Since the data sets introduced in more detail in the following sections were not yet available at the new

Table 4.1.: $t\bar{t}$ and single-top samples used in this thesis (if not stated otherwise). For each sample, the generator used, the product of the final production cross-section and the relevant branching ratio (BR), the K-factor (that has to be applied to the cross-section), the number of MC events and an internal sample ID, is given.

MC@NLO+HERWIG+Jimmy $t\bar{t}$	**K-factor**	**σ [pb]×BR**	**Events**	**ID**
Fully leptonic and semi-leptonic	1.07	202.86	499743	5200
Fully hadronic	1.07	170.74	488264	5204
AcerMC+PYTHIA single-top	**K-factor**	**σ [pb]×BR**	**Events**	**ID**
t-channel, leptonic decay	1.05	41.12	29961	5502
Associated production, semi-leptonic	0.99	14.41	19963	5500

centre-of-mass energy, the PDF re-weighting technique introduced in Section 4.4.2 was used to give an estimate of the expected results. All samples introduced in the following were produced with Athena version 15.3.1.6 from 25 Sep 2009. Further details on the production can be found in [92].

4.5.1. Top-Antitop Events

The $t\bar{t}$ MC samples used in this thesis were produced with MC@NLO version 3.1, where the $t\bar{t}$ decay and the parton shower was carried out by HERWIG version 6.51 and the underlying event was simulated using Jimmy version 4.1. The common PDF set in use was CTEQ6M (see Section 2.1.1). The samples were split up into a leptonic and a hadronic part, containing only events with at least one W boson decaying leptonically or only hadronic W boson decays, respectively. An overview on the available number of MC events, the cross-sections and K-factors applied is given in Table 4.1. The K-factors have been chosen to scale the result to the approximate NNLO cross-section [47] introduced in Section 2.1.1.

4.5.2. W+Jets Events

The W+Jets samples have been produced using the matrix element (ME) generator ALPGEN version 2.13, where, similar to the $t\bar{t}$ samples introduced above, parton shower, hadronisation effects and underlying event have been simulated using HERWIG and Jimmy, respectively. To combine the parton shower and the ME calculation the MLM[1] matching algorithm [105, 106] has been utilised. This allows to combine the benefits of both techniques while avoiding double counting of events. By matching[2] the N partons from the hard process created by the ME generator to jets just and only after the parton showering (no hadronisation yet) and rejecting events with un/double-matched or additional jets, an exclusive W+N-jets sample is obtained. By implementing this for $N = 0 \dots 5$ and allowing additional jets from the showering, with energies even above those of the ME jets,

---

[1] MLM = Michelangelo L. Mangano

[2] The MLM matching requires a $\Delta R \leq 0.3$ between the ME parton and the shower jet.

Table 4.2.: W+Jets samples used in this thesis (if not stated otherwise). For each sample, the generator used, the product of the final production cross-section and the relevant branching ratio (BR), the K-factor (that has to be applied to the cross-section), the number of MC events and an internal sample ID, is given.

ALPGEN+HERWIG+Jimmy W+Jets	**K-factor**	**σ [pb]$\times$BR**	**Events**	**ID**
$W \to e\nu$ + 0 partons	1.22	10184.7	488292	7680
$W \to e\nu$ + 1 parton	1.22	2112.3	260924	7681
$W \to e\nu$ + 2 partons	1.22	676.0	455160	7682
$W \to e\nu$ + 3 partons	1.22	203.3	214619	7683
$W \to e\nu$ + 4 partons	1.22	56.1	58872	7684
$W \to e\nu$ + $\geq$5 partons	1.22	16.6	16992	7685
$W \to \mu\nu$ + 0 partons	1.22	10125.7	459573	7690
$W \to \mu\nu$ + 1 parton	1.22	2155.5	268747	7691
$W \to \mu\nu$ + 2 partons	1.22	682.3	490893	7692
$W \to \mu\nu$ + 3 partons	1.22	202.0	211344	7693
$W \to \mu\nu$ + 4 partons	1.22	55.5	57928	7694
$W \to \mu\nu$ + $\geq$5 partons	1.22	16.3	16975	7695
$W \to \tau\nu$ + 0 partons	1.22	10178.3	498990	7700
$W \to \tau\nu$ + 1 parton	1.22	2106.9	263827	7701
$W \to \tau\nu$ + 2 partons	1.22	672.8	492248	7702
$W \to \tau\nu$ + 3 partons	1.22	202.7	222162	7703
$W \to \tau\nu$ + 4 partons	1.22	55.5	58765	7704
$W \to \tau\nu$ + $\geq$5 partons	1.22	17.0	15913	7705

only in the $N = 5$ sample, an inclusive W+Jets sample is obtained by the combination of these six samples. The CTEQ6L1 PDF set was used and the K-factors were derived to adjust the normalisation to NLO calculations. A summary of the subsamples according to different final state flavours and parton multiplicities (exclusive subsamples), their K-factors, cross-sections and available number of MC events is given in Table 4.2. It has to be stated that only the combination of all subsamples using proper weights, according to their cross-section, gives a physical data sample.

4.5.3. Z+Jets Events

The production of the Z+Jets samples was analogous to the production of the W+Jets samples described in the previous section. A summary of available samples along with their K-factors, cross-sections and statistics is given in Table 4.3.

4.5.4. Single-Top Events

The single-top samples, including only the leptonic decays of W bosons from t-channel production and the semi-leptonic final states of the associated production, were produced using AcerMC, while PYTHIA was used to simulate initial- and final-state parton showers as well as the underlying event, hadronisation and particle decays. K-factors, based on NLO calculations, available statistics for both channels and the cross-sections are stated

Table 4.3.: Z+Jets samples used in this thesis (if not stated otherwise). For each sample, the generator used, the product of the final production cross-section and the relevant branching ratio (BR), the K-factor (that has to be applied to the cross-section), the number of MC events and an internal sample ID, is given.

ALPGEN+HERWIG+Jimmy Z+Jets	**K-factor**	**σ [pb]×BR**	**Events**	**ID**
$Z \to e^+e^-$ + 0 partons	1.22	898.18	269280	7650
$Z \to e^+e^-$ + 1 parton	1.22	206.57	61767	7651
$Z \to e^+e^-$ + 2 partons	1.22	72.50	206945	7652
$Z \to e^+e^-$ + 3 partons	1.22	21.08	63412	7653
$Z \to e^+e^-$ + 4 partons	1.22	6.00	18470	7654
$Z \to e^+e^-$ + $\geq$5 partons	1.22	1.73	5500	7655
$Z \to \mu^+\mu^-$ + 0 partons	1.22	900.21	270098	7660
$Z \to \mu^+\mu^-$ + 1 parton	1.22	205.21	61936	7661
$Z \to \mu^+\mu^-$ + 2 partons	1.22	69.35	207173	7662
$Z \to \mu^+\mu^-$ + 3 partons	1.22	21.63	64956	7663
$Z \to \mu^+\mu^-$ + 4 partons	1.22	6.08	18470	7664
$Z \to \mu^+\mu^-$ + $\geq$5 partons	1.22	1.70	5471	7665
$Z \to \tau^+\tau^-$ + 0 partons	1.22	902.71	270649	7670
$Z \to \tau^+\tau^-$ + 1 parton	1.22	209.26	61928	7671
$Z \to \tau^+\tau^-$ + 2 partons	1.22	70.16	59404	7672
$Z \to \tau^+\tau^-$ + 3 partons	1.22	21.07	63434	7673
$Z \to \tau^+\tau^-$ + 4 partons	1.22	6.04	18500	7674
$Z \to \tau^+\tau^-$ + $\geq$5 partons	1.22	1.71	5479	7675

in Table 4.1. The CTEQ6L1 PDF set was used for the production of these samples, since the production itself only included LO (LO+NLO tree level diagrams) calculations for the associated production (t-channel) production.

4.5.5. QCD-Multi-jet Events

The QCD sample was produced entirely by using PYTHIA version 6.4 with the CTEQ6L1 PDF set. To cope with the overwhelming rate of QCD events especially at low p_T and to allow for studies of the QCD background and due to the fact that QCD samples cannot be produced inclusively in useful amounts of integrated luminosity, a *slicing* technique has been applied in these samples. The QCD dijet process is sliced into multiple samples (J0 to J7), corresponding to bins of the transverse jet p_T of the di-jets in the event. The various subsamples with their p_T ranges, cross-section and available statistics are stated in Table 4.4. Hereby it is only on account of the *slicing* technique that the given statistics could be achieved for the high-p_T subsamples without the necessity to produce the corresponding amount of events in low-p_T samples. No K-factors were available for these samples.

Table 4.4.: QCD dijet samples used in this thesis (if not stated otherwise). For each sample the slicing p_{T} range, the final production cross-section and the number of MC events, is given.

PYTHIA QCD Dijet	σ **[pb]**	**Events**	**#**
J0 (8 GeV $\leq p_T^{\text{dijet}} \leq$ 17 GeV)	1.17×10^{10}	509456	5009
J1 (17 GeV $\leq p_T^{\text{dijet}} \leq$ 35 GeV)	8.67×10^{8}	497574	5010
J2 (35 GeV $\leq p_T^{\text{dijet}} \leq$ 70 GeV)	5.60×10^{7}	496594	5011
J3 (70 GeV $\leq p_T^{\text{dijet}} \leq$ 140 GeV)	3.28×10^{6}	499323	5012
J4 (140 GeV $\leq p_T^{\text{dijet}} \leq$ 280 GeV)	1.52×10^{5}	496326	5013
J5 (280 GeV $\leq p_T^{\text{dijet}} \leq$ 560 GeV)	5.12×10^{3}	498379	5014
J6 (560 GeV $\leq p_T^{\text{dijet}} \leq$ 1120 GeV)	1.12×10^{2}	386529	5015
J7 (1120 GeV $\leq p_T^{\text{dijet}} \leq \infty$)	1.075	376320	5016

Chapter 5.

Event Reconstruction and Selection

In this chapter the reconstruction algorithms, exploited in the analyses presented later in this thesis, are presented. This includes the reconstruction and identification of all final state particles of events containing top quarks and possible backgrounds to those, as described in Section 2.2. These final state particles include electrons and muons[1], jets and neutrinos resulting in missing transverse energy $E_{\mathrm{T}}^{\mathrm{miss}}$. The chapter concludes with a discussion of trigger efficiencies for the various objects.

5.1. Electrons

The reconstruction of electrons follows two different approaches depending on the energy of the particle. The first one, used for low-energy electrons, is a track seeded algorithm, starting from Inner Detector (ID) tracks looking for a matching isolated energy deposition in the Electromagnetic Calorimeter (EMC). In the second approach, used for high-p_{T} electrons with transverse energies of above approximately three GeV, the electron candidate is seeded from the EMC and is the default algorithm in ATLAS. Starting from clusters in the calorimeters a matching track, not coming from a photon-conversion pair reconstructed in the ID, is searched for. After extrapolation of the track into the EMC, the cluster has to be matched within a $\Delta\eta \times \Delta\phi$ window of 0.05×0.10, while the energy-over-momentum fraction (E/p) has to be below ten. For high-p_{T} electrons three sets of quality cuts (loose, medium, tight) have been defined and are explained in detail in [43, pp. 72].

If not stated otherwise, to consider an object an electron the analyses presented below require:

- transverse momentum above 20 GeV (p_{T} >20 GeV),
- pseudo-rapidity within the ID range ($|\eta|$<2.5),
- calorimeter-seeded reconstruction,
- isolation: less than six GeV and less then ten percent additional transverse energy E_{T} in a cone of ΔR=0.2 around the electron axis ($E_{\mathrm{T}}^{\mathrm{cone20}}$ <6 GeV, $E_{\mathrm{T}}^{\mathrm{cone20}}/E_{\mathrm{T}}$ <10%),
- the medium cuts fulfilled (isEM=medium).

Optionally one can demand a pseudo-rapidity outside the transition region between barrel and end-cap (1.37<$|\eta|$<1.52) since the reconstruction and identification efficiencies suffer

---

[1] τ leptons are, due to their difficult reconstruction, not considered in this thesis.

due to an increased amount of material.

5.2. Muons

Due to the design of the ATLAS detector muons are measured twice on their way from the interaction point. This fact allows for a variety of muon identification and reconstruction algorithms. The easiest approach is to reconstruct so-called *stand-alone* muons by finding tracks in the Muon System (MS), which are then extrapolated to the beam line. By using information from the ID to match stand-alone muon to nearby tracks in the ID, so-called *combined* muons can be obtained. Vice versa, so-called *tagged* muons are found by extrapolating tracks from the ID into the MS searching for nearby hits. Different techniques exist for the reconstruction of combined muons. The default approach used in this thesis defines a χ^2 variable as the difference between ID and MS track vectors weighted by their combined covariance matrix and a combined track vector from a statistical combination of ID and MS track vectors. This so-called StaCo (Statistical Combination) algorithm then requires the two track segments within a certain ΔR, the χ^2 below a given value and returns only the match with the lowest χ^2. Further details are given in [43, pp. 162].

Muons considered for the analyses presented below are required to fulfil the following conditions, if not stated otherwise:

- transverse momentum above 20 GeV (p_T >20 GeV),
- pseudo-rapidity within the ID range ($|\eta|$<2.5),
- reconstruction as a combined StaCo muon,
- isolation: less than six GeV and less then ten percent additional transverse energy E_T in a cone of ΔR=0.2 around the electron axis ($E_\mathrm{T}^\mathrm{cone20}$ <6 GeV, $E_\mathrm{T}^\mathrm{cone20}/E_\mathrm{T}$ <10%).

5.3. Jets

A selection of jet-finding algorithms, using input from the ATLAS calorimeter system (see Section 3.2.5), is available with the ATLAS software framework, including event-shape based algorithms as well as sequential recombination algorithms and fixed size cone algorithms. Due to the high granularity of the ATLAS calorimeter system with its about 200,000 individual cells, it is necessary to condense the available information[2] into larger physical objects, before applying any reconstruction algorithm. This can either be done by using so-called projective cell towers (signal towers), defined on a static grid of $\Delta\eta \times \Delta\phi$ of 0.1×0.1; or by using so-called topological cell clusters, trying to combine all topologically connected cells connected to each particle entering the calorimeter. Both methods as well as the reconstruction algorithms are described in great detail in [43, pp. 262]. To correct for effects such as detector imperfections, dead material and bent tracks due to a magnetic field and to identify the jets with partons, one needs to apply jet calibration algorithms. The standard algorithm within ATLAS is based on a cell signal weighting

---

[2] Energy deposition in each of the calorimeter cells.

approach adopted from the H1 experiment [107]. The rationale behind this approach is that in a non-compensating calorimeter low signal densities in calorimeter cells indicate a hadronic signal while high signal densities are more likely to be caused by electromagnetic showers. A compensation is performed in the form of a cell signal weight roughly the size of the electron/pion signal ratio e/π. The default reconstruction algorithm for the analyses presented below is a fixed size cone algorithm using a cone size of R_{cone}=0.4 and signal towers as input.

Fixed Size Cone Jet Finder The first step in a fixed size cone algorithm is to create a p_{T}-ordered list of objects based on the input, e.g. signal towers from the calorimeters or partons in MC simulation. Starting from the most energetic candidate, it is first checked whether a seed threshold p_T^{seed} (default: 1 GeV) is passed. In this case an iterative procedure; combining all objects within a given cone (default: R_{cone}=0.4) with the candidate seed, re-calculating a new centroid direction based on the four-momenta of all objects in the cone and re-collecting the objects within the new cone; is repeated until the direction stabilises. Continuing with the second most energetic candidate this routine is applied for all candidates with a p_{T} above p_T^{seed}. Due to the fact that this basic implementation is not infrared safe, i.e. additional soft particles between two particles belonging to the same jet can affect the recombination of these two particles into a jet, an additional split-and-merge step is performed. Hereby jets sharing more than 50% of the p_{T} of the less energetic jet are merged and those sharing less are split into two.

Flavour-tagging, i.e. the identification of the parton type a jet originated from, will be an important input for future analyses, especially in the case of bottom quarks. Jets stemming from the fragmentation and hadronisation of bottom quarks will be important for e.g. Higgs searches or single-top studies trying to veto large backgrounds from $t\bar{t}$ events. Still b-tagging algorithms are not used in the analyses presented below, firstly because good understanding of the detector is necessary and secondly because the methods presented in this thesis deliberately try to be independent from flavour-tagging algorithms.

Within the scope of this thesis jets, to be recognised as such, have to fulfil the following requirements, if not stated otherwise:

- transverse momentum of at least 20 GeV (p_{T} >20 GeV),
- pseudo-rapidity within a $|\eta|<3.2$ range,
- no overlap with an electron within a radius of 0.2 ($\Delta R_e>0.2$),
- no overlap with a muon within a radius of 0.2 ($\Delta R_\mu>0.2$).

5.4. Missing Transverse Energy

Missing transverse energy ($E_{\mathrm{T}}^{\mathrm{miss}}$) to a large extent originates from particles leaving the detector undetected. But also a limited detector coverage; dead regions; noise from electronics or pile-up; or the finite detector resolution contribute to $E_{\mathrm{T}}^{\mathrm{miss}}$ and have to be corrected for. With respect to top quark physics $E_{\mathrm{T}}^{\mathrm{miss}}$ is the only handle on the energy of the neutrino present both in the signal and the major backgrounds. Two $E_{\mathrm{T}}^{\mathrm{miss}}$ reconstruction algorithms are available within the ATLAS software framework. An object-based algorithm using fully reconstructed, identified and calibrated objects as input and a cell-based algorithm based on energy deposits in calorimeter cells surviving a preceding noise suppression method. Due to the minimised dependence on the reconstruction of other objects the cell-based algorithm will be more robust at initial data taking and is therefore the default in this thesis. The noise suppression method that has to be applied for both algorithms is based, similar to the jet reconstruction, either on cell tower or topological cell cluster information. The implementation based on three-dimensional topological clusters, being the default one in this thesis, starts from a seed cell with an absolute energy above a given multiple of the noise width[3] and requires decreasing contributions from neighbouring cells.

The final cell-based $E_{\mathrm{T}}^{\mathrm{miss}}$ is obtained by including corrections due to energy losses in the calorimeter cryostat and contributions from measured muons[4]. It is commonly referred to as final refined missing transverse energy and is the measure used for the analyses presented below. Further details on the determination of $E_{\mathrm{T}}^{\mathrm{miss}}$ and the various corrections and calibrations can be found in [43, pp. 368].

5.5. Object Matching

After the offline reconstruction of leptons and jets, to access the properties of the corresponding object on a given level of the ATLAS trigger system or in the MC truth information available in MC samples, it is necessary to apply a matching procedure. The simplest approach, also applied as default in this thesis, is to identify the two objects (one from each group, e.g. MC truth and reconstructed electrons) closest to each other in the η-ϕ-plane. An upper limit on the distance is given by $\Delta R < 0.2$, illustrated in Figure 5.1.

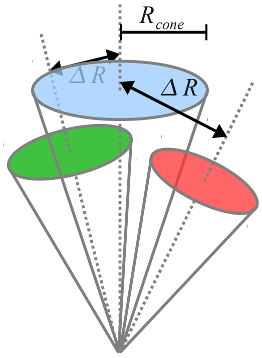

Figure 5.1.: Illustration of the cone radius R_{cone} for the central object (e.g. jet) and the ΔR, used for matching, between the central and each of the other two objects (e.g. trigger and MC truth jet).

---

[3] The noise width is expected to be about 13 GeV only from the electronics of the about 200,000 readout channels [43, p. 369].

[4] Combined muons within a range of $|\eta|<2.5$ and stand-alone muons within $2.5<|\eta|<2.7$.

Table 5.1.: Number and fraction of expected signal (semi-leptonic $t\bar{t}$) events passing each individual preselection cut as well as their sequential combination and the signal-to-background ratio (S/B) at $\sqrt{s}$ = 10 TeV and $\mathcal{L}$=100 pb^{-1}. The efficiency calculation is based on formulas introduced in Appendix B.1.

Cut	$N^{\mathbf{cut}}$	$f^{\mathbf{cut}}$ [%]	$N^{\mathbf{comb}}$	$f^{\mathbf{comb}}$ [%]	$\mathbf{(S/B)^{comb}}$
all events	21716		21716		$O(10^{-8})$
one lepton	10522	48.45±0.07	10522	48.45±0.07	$O(10^{-3})$
$E_{\mathrm{T}}^{\mathrm{miss}}$ >20 GeV	19949	91.86±0.04	9547	43.96±0.07	$O(10^{-3})$
$N_{\mathrm{jet}}^{E_{\mathrm{T}}>20\ \mathrm{GeV}} > 3$	15069	69.39±0.07	6178	28.45±0.06	0.18
$N_{\mathrm{jet}}^{E_{\mathrm{T}}>40\ \mathrm{GeV}} > 2$	12185	56.11±0.07	4261	19.62±0.06	0.78

Table 5.2.: Number and fraction of expected events passing all preselection cuts for signal and background processes at $\sqrt{s}$ = 10 TeV and $\mathcal{L}$=100 pb^{-1}. The efficiency calculation is based on formulas introduced in Appendix B.1.

Sample	$N^{\mathbf{comb}}$	$f^{\mathbf{comb}}$ [%]
$t\bar{t}_{\mathrm{lep}}$	4261	19.62±0.06
W+Jets	2696	0.0600±0.0004
single-top	389	6.8±0.1
Z+Jets	223	0.0500±0.0008
$t\bar{t}_{\mathrm{had}}$	19	0.100±0.005
QCD	2104	$O(10^{-7})$
S/B	0.78±0.02	

5.6. Preselection

Based on the event topology introduced in Section 2.2.1 and the object definitions given in the previous sections, a candidate semi-leptonic $t\bar{t}$ event can be defined as having an isolated reconstructed high-p_{T} lepton (e or μ), a certain amount of missing energy and at least four reconstructed jets. The default preselection, or offline event selection, criteria comprise the following requirements:

- exactly one reconstructed lepton (e or μ) as indicated above,
- missing transverse energy $E_{\mathrm{T}}^{\mathrm{miss}}$ of at least 20 GeV (to account for the neutrino),
- at least four jets with a transverse energy E_{T} above 20 GeV,
- three of those with a transverse energy E_{T} above 40 GeV.

The expected number of semi-leptonic $t\bar{t}$ (signal) events passing each individual preselection cut as well as their sequential combination and the signal-to-background ratio (S/B), considering all samples introduced in Section 4.5, are stated in Table 5.1, while Table 5.2 gives an overview on the number of events after all preselection cuts for various processes. The uncut multiplicity of electrons and muons, as defined in the previous sections, and

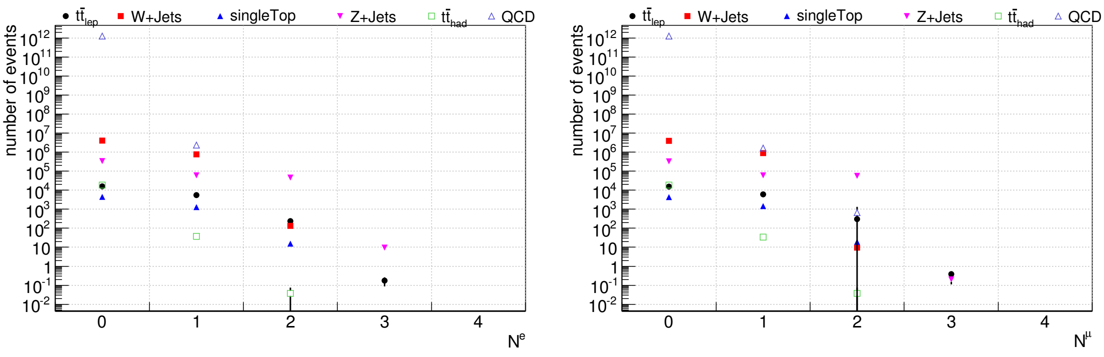

(a) (b)

Figure 5.2.: Multiplicity of (a) electrons and (b) muons, as defined in the text, before applying the preselection cuts, both for an integrated luminosity of 100 pb^{-1}.

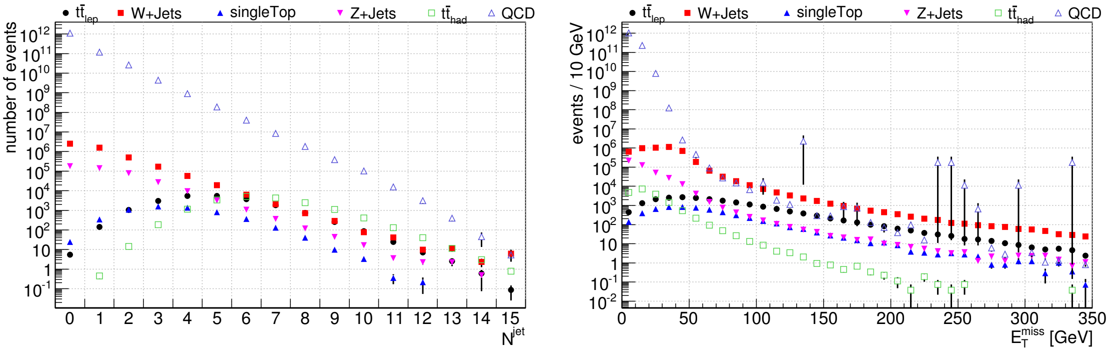

(a) (b)

Figure 5.3.: (a) Multiplicity of jets with p_{T}>5 GeV and (b) $E_{\mathrm{T}}^{\mathrm{miss}}$ distribution before applying the preselection cuts, both for an integrated luminosity of 100 pb^{-1}. The spikes in the $E_{\mathrm{T}}^{\mathrm{miss}}$ distribution for the QCD-multi-jet sample are an artefact of the merging of the p_{T}-sliced MC samples (see Section 4.5.5).

jets with a p_{T}>5 GeV is shown in Figure 5.2(a), 5.2(b) and 5.3(a), respectively, for the signal and the main backgrounds. Figure 5.3(b) shows the uncut $E_{\mathrm{T}}^{\mathrm{miss}}$ distribution for the same samples. The numbers stated and the plots shown assume a centre-of-mass energy $\sqrt{s}$ = 10 TeV and an integrated luminosity of $\mathcal{L}$=100 pb^{-1}, and include all MC samples introduced in Section 4.5 ($t\bar{t}$, W+Jets, Z+Jets, single-top and QCD multi-jets). If not stated otherwise this default offline event selection for semi-leptonic $t\bar{t}$ events is used throughout this thesis. The exclusion of events containing taus is based on their more complicated final state, typically resulting in a low purity of the selection due to bad QCD rejection.

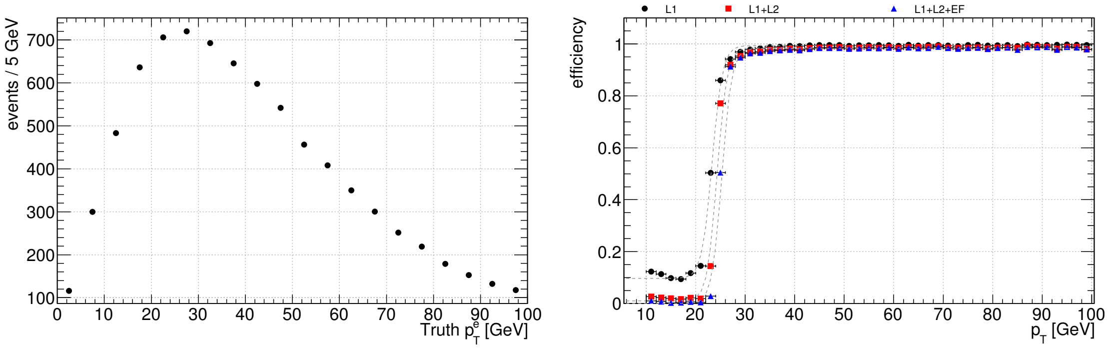

(a) (b)

Figure 5.4.: (a) Transverse momentum (p_T) spectrum of MC truth electrons originating from the leptonic decay of a W boson in top pair, scaled to an integrated luminosity of 100 pb^{-1}. (b) Exemplary trigger efficiency turn-on curves, with respect to the reconstructed transverse momentum, for the e25i_medium trigger chain in leptonic top pair events. The curves are fitted with a Fermi-Dirac-like function.

5.7. Trigger Efficiencies

As introduced in Section 3.2.8 only events passing the three-stage ATLAS trigger system are recorded by the storage system. An efficient selection of the objects discussed in the previous sections is therefore essential for any top quark related analysis. In this section a few details on the selection of electrons, muons, jets and $E_\mathrm{T}^\mathrm{miss}$ will be given, also serving as an introduction to the analyses presented in the next chapter. Due to the use of weighted MC events, the calculation of efficiencies and more importantly their according uncertainties differs from the case of unweighted events. The utilised formulas are discussed in more detail in Appendix B.1. In cases where the trigger efficiency is plotted as a function of the p_T threshold value, these so-called turn-on curves are fitted with a Fermi-Dirac-like function as described in Appendix B.2.

Electrons Semi-leptonic events with one W boson decaying into an electron and a neutrino and the other W boson decaying hadronically amount for about fifteen percent of all top pair final states. The transverse momentum (p_T) spectrum of electrons originating from the leptonic decay of a W boson in top pair events expected from MC truth is shown in Figure 5.4(a). From this plot the fraction of events expected to be evaluated by the trigger system above a given p_T value can be estimated. To avoid prescaling, single electron triggers are expected to have a p_T threshold of about 20 GeV and above or have to be combined with other trigger items, forming complex multi-object triggers. The LVL1 electron trigger is exclusively based on information from the EMC and operates on reduced granularity trigger towers as introduced in Section 3.2.8. Clusters of four central (2×2) and twelve surrounding ($4 \times 4 - 4$) towers are formed in the EMC and HC over a pseudo-rapidity range of $|\eta| < 2.5$. The ring of surrounding towers is used to define isolation criteria cutting on a maximum energy deposit in this area. At LVL2 electromagnetic clusters are matched to tracks reconstructed in the ID. At EF, cluster and track

Table 5.3.: Event selection efficiencies for three exemplary single electron trigger chains for leptonic $t\bar{t}$ events with a MC truth $W \to e\nu$ decay at $\sqrt{s} = 10$ TeV and an integrated luminosity of 100 pb^{-1}. The numbers stated for LVL2 and EF include a positive trigger decision on all preceding levels. The index *total* denotes quantities derived from all reconstructed events, while *preselect* refers to quantities derived from reconstructed events that pass the preselection.

Trigger Item	N^{total}	$\varepsilon^{\mathrm{total}}$ [%]	$N^{\mathrm{preselect}}$	$\varepsilon^{\mathrm{preselect}}$ [%]
all	7157		1835	
L1_EM23I	5348	74.7±0.1	1731	94.4±0.1
L2_e25i_loose	4915	68.8±0.1	1679	91.5±0.1
EF_e25i_loose	4676	65.3±0.1	1653	90.1±0.1
L1_EM23I	5348	74.7±0.1	1731	94.4±0.1
L2_e25i_medium	4907	68.6±0.1	1677	91.4±0.1
EF_e25i_medium	4580	64.0±0.1	1646	89.7±0.1
L1_EM18	6838	95.55±0.05	1833	99.88±0.02
L2_e55_loose	2827	39.5±0.1	942	51.3±0.2
EF_e55_loose	2243	31.3±0.1	777	42.3±0.2

reconstruction are refined, by using more advanced but time consuming algorithms.

The event selection efficiencies for three exemplary single electron trigger chains for leptonic $t\bar{t}$ events with a MC truth $W \to e\nu$ decay at an integrated luminosity of 100 pb^{-1} are given in Table 5.3. These examples have been chosen since they are expected to represent the non-prescaled trigger chains with the lowest threshold on p_{T}. The efficiencies are calculated with respect to the total number of expected signal events N^{total} and to the number of reconstructed and preselected events $N^{\mathrm{preselect}}$, respectively. Turn-on curves, showing the fraction of events passing the p_{T} threshold as a function of the reconstructed p_{T}, are shown for all three levels of the e25i_medium trigger chain[5] in Figure 5.4(b). The LVL1 acceptance is non-zero even at energies below the threshold, which is mainly due to a choice, adjusted to the crude energy measurement at LVL1, not to veto on good events too early in the trigger chain. A selection efficiency of above 90% is reached almost instantly at the threshold value of 25 GeV. The high efficiency is partly due to jets faking electron signatures at the various levels. The number of jets reconstructed as electrons can be minimised by using tighter isolation criteria and has to be corrected for eventually. For these studies primarily a high efficiency is required, therefore this effect is not studied in more detail here. The efficiencies stated for LVL2 and EF include a positive trigger decision on all preceding levels.

Muons Similar to the electron case, semi-leptonic events with one W boson decaying into an muon and a neutrino and the other W boson decaying hadronically amount for about 15% of all top pair final states. The spectrum of the rather large expected transverse momentum (p_{T}) of muons originating from the leptonic decay of a W boson in top pair events obtained from MC truth is shown in Figure 5.5(a), again allowing to estimate the

---

[5] L1_EM23I→L2_e25i_medium→EF_e25i_medium

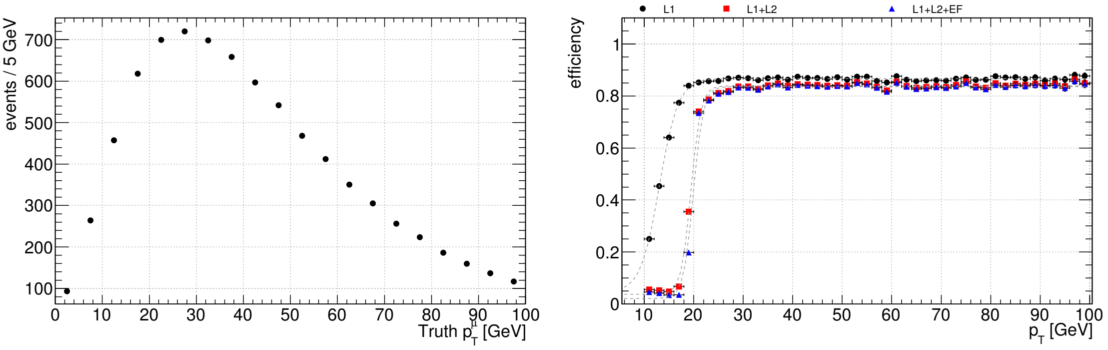

(a)

(b)

Figure 5.5.: (a) Transverse momentum (p_T) spectrum of MC truth muons originating from the leptonic decay of a W boson in top pair, scaled to an integrated luminosity of 100 pb^{-1}. (b) Exemplary trigger efficiency turn-on curves, with respect to the reconstructed transverse momentum, for the mu20 trigger chain in leptonic top pair events. The curves are fitted with a Fermi-Dirac-like function.

fraction of events facing the trigger system above a given p_T value. Due to the large W boson mass, the mean p_T of muons in $t\bar{t}$ events is expected to be rather large, allowing for non-prescaled single muon triggers. As for electrons, the p_T threshold of a single muon trigger can be lowered by forming multi-object triggers. The LVL1 muon trigger is based solely on information from the Muon System (MS), introduced in Section 3.2.6, and assigns one of six programmable and discrete p_T values to the muon candidate without actually reconstructing the muon. The reconstruction is for the first time done at LVL2. In a first step, a muon candidate is reconstructed, again only using information from the MS. In the following steps, tracks are reconstructed in the Inner Detector (ID) around the previously obtained MS muon candidate and combined with the tracks from the MS. The LVL2 decision is then based entirely on the p_T of these combined muon candidates[6]. At EF various possible algorithms, more time consuming and also used for the offline reconstruction of muons, deliver a trigger decision also based exclusively on the p_T of the muon candidate.

The event selection efficiencies for three exemplary single muon trigger chains for leptonic $t\bar{t}$ events with a MC truth $W \to \mu\nu$ decay at an integrated luminosity of 100 pb^{-1} are given in Table 5.4. While these examples are chosen to give an overview on the trigger efficiency over a wide p_T-range, it is the mu20 trigger chain[7] that will be most relevant for selecting semi-leptonic $t\bar{t}$ events. The efficiencies are calculated with respect to the total number of expected signal events N^{total} and to the number of reconstructed and preselected events $N^{\mathrm{preselect}}$, respectively. Figure 5.5(b) shows turn-on curves for all three levels of the mu20 trigger chain. The efficiencies stated for LVL2 and EF include a positive trigger decision on all preceding levels. Due to only using information from the MS and using discrete p_T values, as indicated above, the LVL1 acceptance is already quite high

---

[6] In a possible upgrade of the system the LVL2 decision might consider isolation requirements as well as constraints on the quality of the track combination in addition to the p_T threshold.

[7] L1_MU20→L2_mu20→EF_mu20

Table 5.4.: Event selection efficiencies for three exemplary single muon trigger chains for leptonic $t\bar{t}$ events with a MC truth $W \to \mu\nu$ decay at $\sqrt{s} = 10$ TeV and an integrated luminosity of 100 pb^{-1}. The numbers stated for LVL2 and EF include a positive trigger decision on all preceding levels. The index *total* denotes quantities derived from all reconstructed events, while *preselect* refers to quantities derived from reconstructed events that pass the preselection.

Trigger Item	N^{total}	$\varepsilon^{\text{total}}$ [%]	$N^{\text{preselect}}$	$\varepsilon^{\text{preselect}}$ [%]
all	6780		2078	
L1_MU6	5711	84.24±0.09	1899	91.4±0.1
L2_mu6	5596	82.54±0.10	1873	90.2±0.1
EF_mu6	5546	81.81±0.10	1862	89.6±0.1
L1_MU20	5077	74.9±0.1	1796	86.4±0.2
L2_mu20	4517	66.6±0.1	1728	83.2±0.2
EF_mu20	4444	65.5±0.1	1717	82.6±0.2
L1_MU40	4601	67.8±0.1	1704	82.0±0.2
L2_mu40	2908	42.9±0.1	1125	54.2±0.2
EF_mu40	2733	40.3±0.1	1060	51.0±0.2

even for muons reconstructed below the given threshold of 20 GeV. Similar to the electron trigger example, this strategy was chosen not to veto on good muons too early in the process. Due to geometrical regions of the MS not covered by RPCs, used for the muon trigger, the efficiency saturates slightly above 80% [43, pp. 647].

Jets A broad discussion of analyses concerning jet triggers in top quark events is given in Chapter 6. Also these results have been published in [43].

Missing Transverse Energy All semi-leptonic top pair events contain a non-negligible amount of missing transverse energy ($E_{\mathrm{T}}^{\mathrm{miss}}$), due to the neutrino stemming from the leptonic W boson decay. The $E_{\mathrm{T}}^{\mathrm{miss}}$ spectrum expected from MC truth and turn-on curves for various $E_{\mathrm{T}}^{\mathrm{miss}}$ trigger chains featuring different thresholds are shown in Figure 5.6(a) and 5.6(b), respectively. As can be seen from the latter plot, especially low thresholds $E_{\mathrm{T}}^{\mathrm{miss}}$ trigger items have to be taken with a grain of salt, due to the high acceptance even below threshold. Since this will lead to an increased selection of background events not containing missing energy coming from a neutrino, such as hadronic $t\bar{t}$ or QCD-multi-jet events, higher thresholds of 50 GeV and above are required for single $E_{\mathrm{T}}^{\mathrm{miss}}$ trigger items. As an alternative, complex multi-object triggers, as introduced for electron and muon triggers, can be used to allow for lower thresholds both for the $E_{\mathrm{T}}^{\mathrm{miss}}$ and the combined object items.

At LVL1, the decision is based on calorimeter information covering the full $|\eta| < 5$ range using reduced granularity information, as introduced in Section 5.4. While the LVL1 $E_{\mathrm{T}}^{\mathrm{miss}}$ trigger decision is not refined at LVL2, which only uses the information from the ROIs, the EF trigger utilises the same refined algorithms as the offline reconstruction, introduced

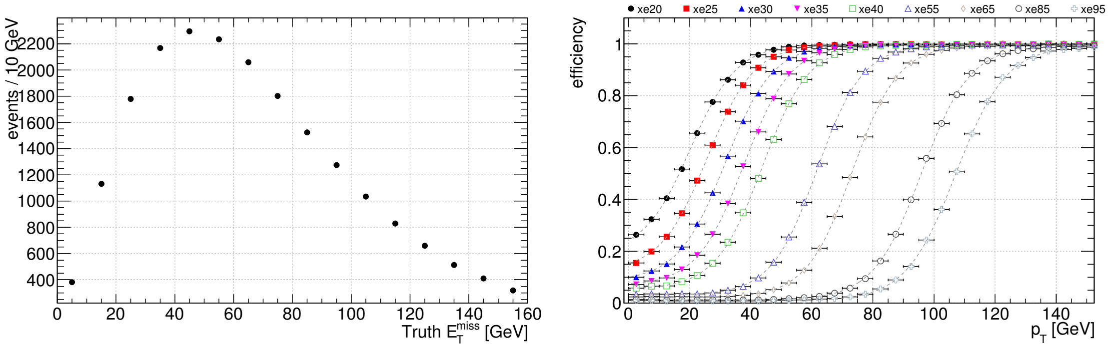

(a)

(b)

Figure 5.6.: (a) $E_{\mathrm{T}}^{\mathrm{miss}}$ spectrum expected from MC truth, scaled to an integrated luminosity of 100 pb^{-1} and (b) trigger efficiency turn-on curves for various $E_{\mathrm{T}}^{\mathrm{miss}}$ EF trigger items. The curves are fitted with a Fermi-Dirac-like function.

before.

The event selection efficiencies for three exemplary $E_{\mathrm{T}}^{\mathrm{miss}}$ trigger chains at an integrated luminosity of 100 pb^{-1} at $\sqrt{s} = 10$ TeV are given in Table 5.5. As for the electron and muon triggers, the efficiencies are calculated with respect to the total number of expected signal events N^{total} and to the number of reconstructed and preselected events $N^{\mathrm{preselect}}$, respectively, and the efficiencies stated for LVL2 and EF include a positive trigger decision on all preceding levels. Especially during the first months of running the experiment, single $E_{\mathrm{T}}^{\mathrm{miss}}$ trigger chains are not expected to play an important role, due to the level of detector understanding required to fully control this quantity, though items as stated in Table 5.5 might be used to form complex multi-object trigger items in combination with lepton or jet triggers.

Table 5.5.: Event selection efficiencies for three exemplary $E_{\mathrm{T}}^{\mathrm{miss}}$ trigger chains for leptonic $t\bar{t}$ events at an integrated luminosity of 100 pb^{-1} at $\sqrt{s} = 10$ TeV. The numbers stated for LVL2 and EF include a positive trigger decision on all preceding levels. The index *total* denotes quantities derived from all reconstructed events, while *preselect* refers to quantities derived from reconstructed events that pass the preselection.

Trigger Item	N^{total}	$\varepsilon^{\mathrm{total}}$ [%]	$N^{\mathrm{preselect}}$	$\varepsilon^{\mathrm{preselect}}$ [%]
all	21716		4261	
L1_XE30	16629	76.57±0.06	3467	81.4±0.1
L2_xe30	15419	71.00±0.06	3142	73.7±0.1
EF_xe40	12545	57.77±0.07	2530	59.4±0.2
L1_XE40	13473	62.04±0.07	2924	68.6±0.1
L2_xe40	11947	55.01±0.07	2478	58.1±0.2
EF_xe55	8678	39.96±0.07	1693	39.7±0.2
L1_XE50	10404	47.91±0.07	2353	55.2±0.2
L2_xe50	8805	40.54±0.07	1845	43.3±0.2
EF_xe65	6334	29.16±0.06	1220	28.6±0.1

Chapter 6.

Trigger Studies for Top-Antitop Events

This chapter summarises studies of the performance of the ATLAS trigger system, which is described in Section 3.2.8, with an emphasis on jet trigger items using top quark events. Since they offer a large set of different and complex event signatures, as introduced in Section 2.2, top quark events are not only interesting from a physics point of view, but also from a trigger perspective. With a considerable overlap of trigger signatures top quark events will provide ideal means to determine trigger efficiencies in real data. Trigger efficiencies of single lepton triggers as well as trigger items using quantities such as $E_{\mathrm{T}}^{\mathrm{miss}}$ have been briefly discussed in Section 5.7. Here the attention will be directed to single and multi-jet triggers in Section 6.1 and the overlap of various trigger items in Section 6.2. Finally, methods for a data-driven determination of the trigger efficiency will be presented in Section 6.3, again putting an emphasis on jet trigger items (Section 6.3.2).

The studies presented in this chapter and performed in the course of this thesis have been published in [43] using $\sqrt{s}$ =14 TeV MC samples as input. For consistency within this thesis and to verify the previously obtained outcomes, the results shown here have been obtained with a more recent release of the ATLAS software framework (see Section 4.5) at a centre-of-mass energy $\sqrt{s}$=10 TeV and an assumed integrated luminosity $\mathcal{L}$=100 pb^{-1}, if not indicated otherwise.

6.1. Jet Triggers

Jet triggers for $t\bar{t}$ events pose an enormous difficulty, due to the immense background of QCD-multi-jet events, with cross-sections several orders of magnitude larger than those for top production. The possibility of using trigger items solely based on jets is therefore not self-evident and the definition of complex multi-object triggers, containing jet as well as lepton or $E_{\mathrm{T}}^{\mathrm{miss}}$ triggers seems much more obvious. To characterise the jet distributions in $t\bar{t}$ events the p_{T} distribution of the six leading jets (ordered by p_{T} and p_{T} >5 GeV) after the ATLAS Full Simulation is shown in Figures 6.1(a) and 6.1(b) for leptonic and fully-hadronic $t\bar{t}$ events, respectively. The characteristic increase of the mean jet energy in fully-hadronic compared to leptonic $t\bar{t}$ events can be easily observed. This is due to the W boson decay yielding, in the fully-hadronic case, high-p_{T} jets instead of leptons. In the same way this difference offers some power to discriminate between fully-hadronic and leptonic $t\bar{t}$ events, it is the general large number of jets that allows to differentiate between $t\bar{t}$ events as a whole and the major backgrounds, mainly featuring steeply falling p_{T} spectra. The latter is shown in Figure 5.3(a) for $t\bar{t}$ events and the major backgrounds.

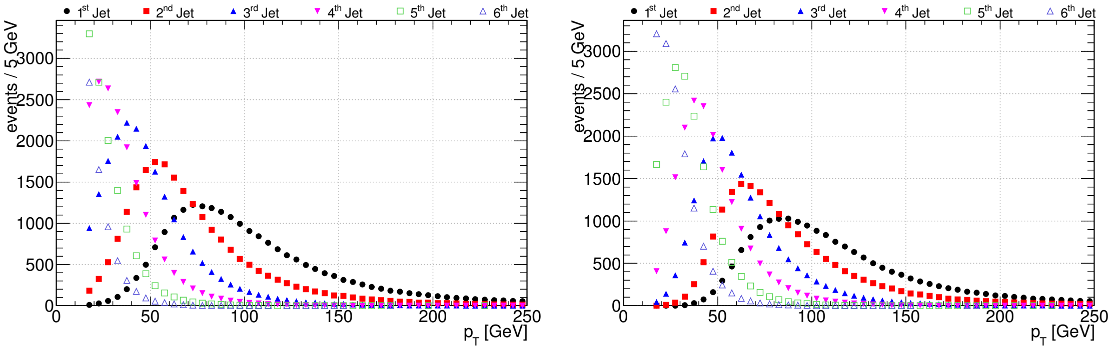

(a)

(b)

Figure 6.1.: p_T distribution of the six leading jets (ordered by p_T) for (a) leptonic and (b) fully-hadronic $t\bar{t}$ events.

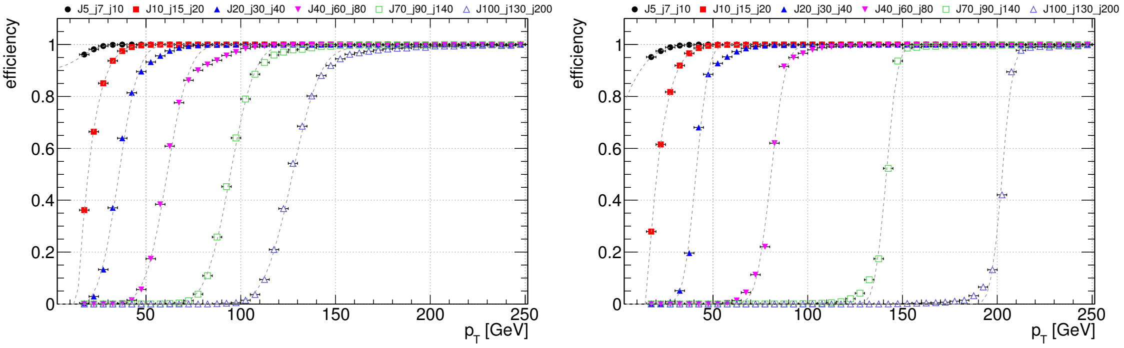

(a)

(b)

Figure 6.2.: Trigger efficiency turn-on curves of (a) various LVL1 jet trigger items and (b) their corresponding complete trigger chains for leptonic $t\bar{t}$ events. The p_T thresholds for all three levels of each of the plotted chains are stated in the legend (e.g. chain L1_J10→L2_j15→EF_j20 shown as full red boxes).

The LVL1 jet trigger is based on reduced granularity trigger towers from the HC as introduced in Section 3.2.8. Clusters of four (2×2) towers both in the EMC and HC, representing a local maximum compared to their surrounding counterparts, are formed and compared to predefined jet energy thresholds. The LVL1 jet trigger decision is then based only on the multiplicity of trigger clusters passing a certain E_T threshold. This information is refined at LVL2 and EF as introduced in Section 3.2.8, offering various reconstruction algorithms at the last level. As indicated in Section 5.3 the default jet reconstruction algorithm used in the following is a fixed size cone algorithm with a cone of R_cone=0.4.

Matching jet trigger objects at a given level with the reconstructed jets after the ATLAS Full Simulation allows to illustrate the turn-on behaviour as well as the differential efficiency for a certain trigger threshold. Figure 6.2(a) shows turn-on curves of various LVL1

Table 6.1.: Jet trigger efficiencies, calculated with respect to the total number of events, and expected rates (without prescaling), assuming an instantaneous luminosity of 10^{31} cm^{-2} s^{-1} , for different jet trigger chains. Note that the W+Jets sample only contains events with leptonically decaying W bosons.

Trigger Chain		$t\bar{t}_{\mathbf{lep}}$	$t\bar{t}_{\mathbf{had}}$	W**+Jets**	**QCD**
L1_J20→L2_j30→EF_j40	$\varepsilon^{\text{trig}}$ [%]	99.15±0.01	99.898±0.005	27.29±0.03	0.456±0.002
	R [Hz]	$O(10^{-3})$	$O(10^{-3})$	$O(10^{-1})$	$O(10^{2})$
L1_J70→L2_j90→EF_j140	$\varepsilon^{\text{trig}}$ [%]	28.74±0.06	34.49±0.07	0.601±0.002	≈0.002
	R [Hz]	$O(10^{-4})$	$O(10^{-4})$	$O(10^{-3})$	$O(1)$
L1_J100→L2_j130→EF_j200	$\varepsilon^{\text{trig}}$ [%]	11.27±0.05	14.03±0.05	0.183±0.001	<0.001
	R [Hz]	$O(10^{-4})$	$O(10^{-4})$	$O(10^{-4})$	$O(10^{-1})$
L1_3J20→L2_3j30→EF_3j40	$\varepsilon^{\text{trig}}$ [%]	71.12±0.06	90.10±0.04	0.842±0.002	≈0.009
	R [Hz]	$O(10^{-3})$	$O(10^{-3})$	$O(10^{-3})$	$O(10)$
L1_3J40→L2_3j60→EF_3j80	$\varepsilon^{\text{trig}}$ [%]	19.74±0.06	32.95±0.07	0.114±0.001	≈0.001
	R [Hz]	$O(10^{-4})$	$O(10^{-4})$	$O(10^{-4})$	$O(10^{-1})$
L1_4J10→L2_4j20→EF_4j30	$\varepsilon^{\text{trig}}$ [%]	69.57±0.07	94.02±0.03	0.605±0.002	≈0.009
	R [Hz]	$O(10^{-3})$	$O(10^{-3})$	$O(10^{-3})$	$O(10)$
L1_4J20→L2_4j30→EF_4j40	$\varepsilon^{\text{trig}}$ [%]	39.97±0.07	68.93±0.07	0.161±0.001	≈0.001
	R [Hz]	$O(10^{-4})$	$O(10^{-3})$	$O(10^{-4})$	$O(1)$

jet trigger items featuring different p_{T} thresholds. In Figure 6.2(b) the same kind of plot is given for the corresponding trigger chains for jets passing all three levels. Both plots are shown for leptonic $t\bar{t}$ events. It can be seen that especially at LVL1 the jet energies are underestimated, resulting in a large fraction of jets, reconstructed below the given threshold, being selected at this stage. The underestimation is caused by the lack of an online jet calibration at LVL1. To compensate for this, items with low enough thresholds have to be selected at LVL1 to allow for an efficient overall selection. Also it has to be noted that a given trigger chain provides about 90% efficiency only to jets with reconstructed p_{T} about 10 GeV above the given threshold.

Jet trigger efficiencies, calculated with respect to the total number of events, and rates, assuming an instantaneous luminosity of 10^{31} cm^{-2} s^{-1} , are stated in Table 6.1, for a selection of jet trigger chains. As introduced in Section 3.2.8, passing a whole trigger chain implies that the requirements of the trigger items have been met on all three levels and the event will be written to permanent storage. Depending on the jet trigger threshold, the efficiency of single jet trigger chains varies between about 10 to 100%, though only chains with thresholds above 100 GeV will remain non-prescaled. For example, at an integrated luminosity of 10^{31} cm^{-2} s^{-1} the prescale factor for the LVL1 item L1_J70 is expected to be about 15, resulting in a rate after prescaling of $O(1)$ Hz. About the same order of magnitude is expected for the L1_J100 trigger item, though without any prescaling. Comparing the rates expected especially from low-p_{T} chains in the QCD sample to the maximum data output rate of 200 Hz (see Section 3.2.8) the need for high threshold, higher multiplicity or complex multi-object triggers becomes apparent.

To investigate the performance of higher multiplicity triggers, Figures 6.3(a) and 6.3(b) show the trigger efficiency for different jet multiplicities as a function of the trigger p_{T}

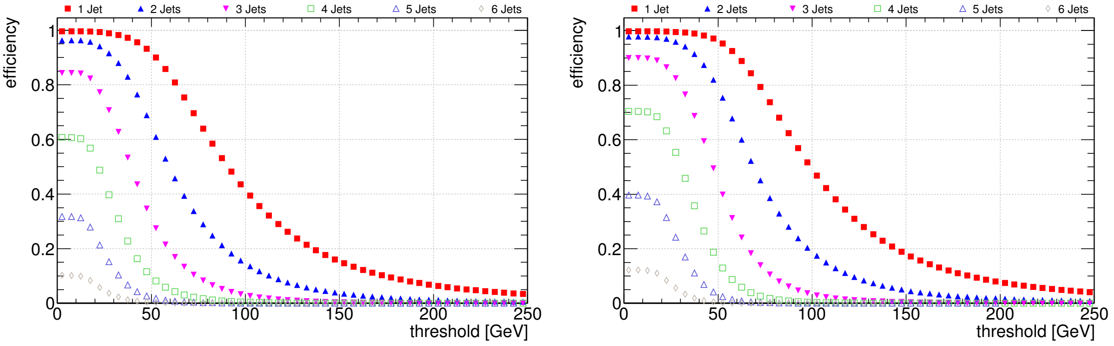

(a)

(b)

Figure 6.3.: Trigger efficiency for different jet multiplicities as a function of the trigger p_T threshold (same threshold for all jets) for leptonic (a) and fully-hadronic (b) $t\bar{t}$ events.

threshold for leptonic and fully-hadronic $t\bar{t}$ events, respectively. It can be seen that up to thresholds of about 50 GeV (60 GeV) a single jet trigger will be more than 90% efficient in selecting leptonic (hadronic) $t\bar{t}$ events, though encountering the huge background discussed above. At about 100 GeV the efficiency drops to roughly 40% (50%). In particular interesting for the selection of hadronic $t\bar{t}$ events, due to the lack of leptons to trigger on and the increased mean p_T and multiplicity of jets, is the possibility to create high-multiplicity jet triggers with varying thresholds (e.g. EF_4j60_EF_2j100_EF_j170[1]), to further suppress the background contamination while keeping the same level of signal selection efficiency. Table 6.2 states selection efficiencies and expected rates at an instantaneous luminosity of 10^{31} cm^{-2} s^{-1} for a few exemplary high-multiplicity jet trigger items at EF. The subject of high-multiplicity jet triggers with varying thresholds and optimised for the selection of hadronic $t\bar{t}$ events is further discussed in [43]. As for the single jet trigger also high-multiplicity jet trigger chains with low thresholds have to be prescaled in order to reduce the event rate to a level manageable by the storage system. Due to the required multiplicity this threshold can be as low as about 20 GeV at LVL1 for simple 3 and 4 jet combinations, such as L1_3J20 and L1_4J20, to avoid prescaling.

6.2. Trigger Item Overlap

As introduced above, $t\bar{t}$ events offer considerable overlap between various trigger signatures, caused by the rich event topologies featuring both leptons and a sizeable number of jets as well as substantial amounts of missing transverse energy in the final state. This redundancy allows both for the enhancement of the signal-to-background ratio, by creating complex multi-object triggers, and to monitor or measure the trigger efficiency. The latter case will be discussed in the next section.

When triggering events using single object trigger items, the corresponding efficiency can

---

[1] This item would require four jets with p_T >60 GeV, two jets with p_T >100 GeV and one jet with p_T >170 GeV at EF level.

Table 6.2.: EF efficiencies, calculated with respect to the total number of events, and rates, assuming an instantaneous luminosity of 10^{31} cm^{-2} s^{-1} , for different jet trigger items.

EF Trigger Item		$t\bar{t}_{\mathbf{lep}}$	$t\bar{t}_{\mathbf{had}}$	W**+Jets**	**QCD**
EF_4j60_EF_2j100_EF_j170	$\varepsilon^{\text{trig}}$ [%]	16.69±0.05	20.21±0.06	≈0.06	≈0.001
	R [Hz]	$O(10^{-4})$	$O(10^{-4})$	$O(10^{-4})$	$O(10^{-1})$
EF_5j45_EF_2j60_EF_j100	$\varepsilon^{\text{trig}}$ [%]	49.71±0.07	51.51±0.07	≈0.09	≈0.004
	R [Hz]	$O(10^{-3})$	$O(10^{-4})$	$O(10^{-4})$	$O(1)$
EF_6j35_EF_5j45_EF_4j50_EF_3j60	$\varepsilon^{\text{trig}}$ [%]	64.57±0.07	51.15±0.07	≈0.06	≈0.006
	R [Hz]	$O(10^{-3})$	$O(10^{-4})$	$O(10^{-4})$	$O(1)$

only be increased by lowering the threshold and thereby increasing the rate. The aim of multi-object or combined triggers is to enrich the selection of signal physics channels without modifying the given thresholds of individual trigger items, while at the same time minding the rate constraints of the experiment. This can be achieved by designing trigger combinations following the event topologies of the signal processes and vetoing on unmatched background events. To avoid complications in the trigger efficiency determination, combinations of trigger items are best based on non-correlated (orthogonal) individual items. Since the combination through a logical AND operator limits the maximum acceptance to that of the lowest individual item, it is also desirable to incorporate low threshold trigger items. In addition all individual items used for the combined trigger must be included in the trigger menu, if necessary with a prescale factor, to allow for a data-driven determination of the individual trigger efficiencies.

To identify possible candidates for combined triggers the overlap, hence the correlation, between various trigger items has been investigated. Figures 6.4(a) and 6.4(b) show the item overlap at LVL1 and the chain overlap after all three levels, respectively, for leptonic $t\bar{t}$ events. In Figure 6.5 the same is plotted for hadronic $t\bar{t}$ events. The selection of trigger items is based on the default trigger menu for the given MC samples. For the leptonic $t\bar{t}$ sample there is a considerable overlap between various object types, clearly illustrating the event topology. Here the overlap between $E_{\mathrm{T}}^{\mathrm{miss}}$ and other trigger items could be potentially useful for complex multi-object triggers. Also expected is the very low acceptance of the lepton trigger items in the hadronic $t\bar{t}$ sample. Only electron triggers at LVL1 (as explained in Section 5.7) and muon triggers with low thresholds have a considerable efficiency. The latter is hereby mainly caused by low-p_{T} muons stemming from the b-jets. As a result, possible complex multi-object triggers to increase the signal-to-background ratio for hadronic $t\bar{t}$ events have to rely on jet triggers only.

6.3. Trigger Efficiencies from Data

To reduce the dependence on MC simulation, trigger efficiencies should be evaluated as much as possible directly from data (data-driven). Especially during the start-up phase, with MC simulations not being adapted to real data yet, the MC description of the absolute as well as the differential trigger efficiency will feature large uncertainties. A common

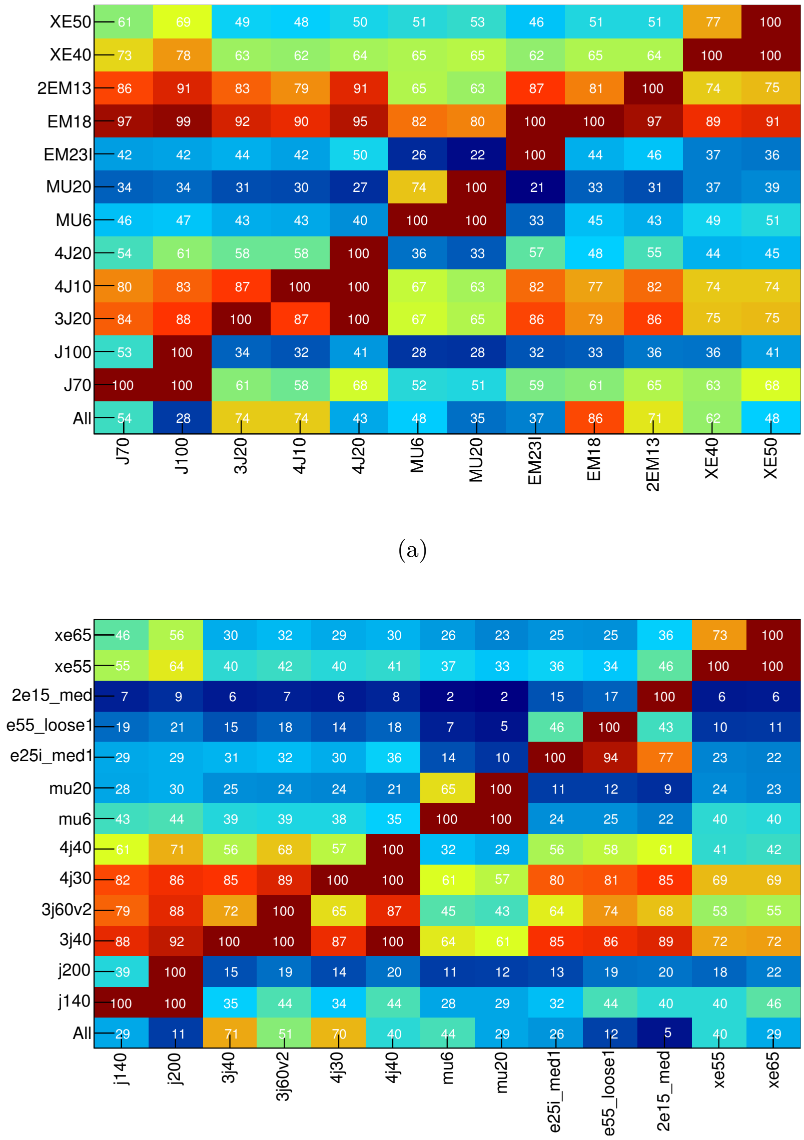

(a)

	J70	J100	3J20	4J10	4J20	MU6	MU20	EM23I	EM18	2EM13	XE40	XE50
XE50	61	69	49	48	50	51	53	46	51	51	77	100
XE40	73	78	63	62	64	65	65	62	65	64	100	100
2EM13	86	91	83	79	91	65	63	87	81	100	74	75
EM18	97	99	92	90	95	82	80	100	100	97	89	91
EM23I	42	42	44	42	50	26	22	100	44	46	37	36
MU20	34	34	31	30	27	74	100	21	33	31	37	39
MU6	46	47	43	43	40	100	100	33	45	43	49	51
4J20	54	61	58	58	100	36	33	57	48	55	44	45
4J10	80	83	87	100	100	67	63	82	77	82	74	74
3J20	84	88	100	87	100	67	65	86	79	86	75	75
J100	53	100	34	32	41	28	28	32	33	36	36	41
J70	100	100	61	58	68	52	51	59	61	65	63	68
All	54	28	74	74	43	48	35	37	86	71	62	48

(b)

	j140	j200	3j40	3j60v2	4j30	4j40	mu6	mu20	e25i_med1	e55_loose1	2e15_med	xe55	xe65
xe65	46	56	30	32	29	30	26	23	25	25	36	73	100
xe55	55	64	40	42	40	41	37	33	36	34	46	100	100
2e15_med	7	9	6	7	6	8	2	2	15	17	100	6	6
e55_loose1	19	21	15	18	14	18	7	5	46	100	43	10	11
e25i_med1	29	29	31	32	30	36	14	10	100	94	77	23	22
mu20	28	30	25	24	24	21	65	100	11	12	9	24	23
mu6	43	44	39	39	38	35	100	100	24	25	22	40	40
4j40	61	71	56	68	57	100	32	29	56	58	61	41	42
4j30	82	86	85	89	100	100	61	57	80	81	85	69	69
3j60v2	79	88	72	100	65	87	45	43	64	74	68	53	55
3j40	88	92	100	100	87	100	64	61	85	86	89	72	72
j200	39	100	15	19	14	20	11	12	13	19	20	18	22
j140	100	100	35	44	34	44	28	29	32	44	40	40	46
All	29	11	71	51	70	40	44	29	26	12	5	40	29

Figure 6.4.: (a) Trigger item overlap at LVL1 and (b) the chain overlap after all three levels, in leptonic $t\bar{t}$ events. The stated numbers represent the percentage of events selected by a trigger item given on the x-axis that is also triggered by a given item on the y-axis. In the bottom row, the numbers denote the total efficiency of the trigger item given on the x-axis. By definition, the values on the diagonal (bottom-left to top-right) have full overlap (100%, red), while uncorrelated item have zero overlap (0%, blue).

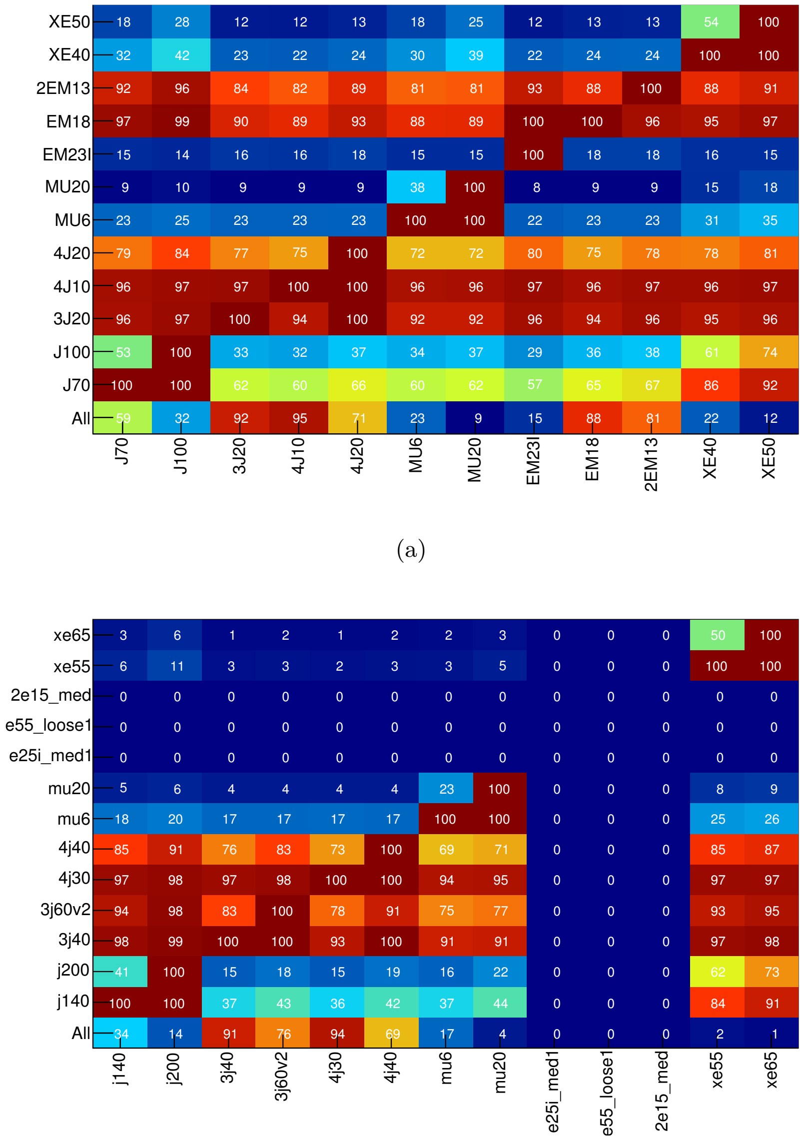

	J70	J100	3J20	4J10	4J20	MU6	MU20	EM23I	EM18	2EM13	XE40	XE50
XE50	18	28	12	12	13	18	25	12	13	13	54	100
XE40	32	42	23	22	24	30	39	22	24	24	100	100
2EM13	92	96	84	82	89	81	81	93	88	100	88	91
EM18	97	99	90	89	93	88	89	100	100	96	95	97
EM23I	15	14	16	16	18	15	15	100	18	18	16	15
MU20	9	10	9	9	9	38	100	8	9	9	15	18
MU6	23	25	23	23	23	100	100	22	23	23	31	35
4J20	79	84	77	75	100	72	72	80	75	78	78	81
4J10	96	97	97	100	100	96	96	97	96	97	96	97
3J20	96	97	100	94	100	92	92	96	94	96	95	96
J100	53	100	33	32	37	34	37	29	36	38	61	74
J70	100	100	62	60	66	60	62	57	65	67	86	92
All	59	32	92	95	71	23	9	15	88	81	22	12

(a)

	j140	j200	3j40	3j60v2	4j30	4j40	mu6	mu20	e25i_med1	e55_loose1	2e15_med	xe55	xe65
xe65	3	6	1	2	1	2	2	3	0	0	0	50	100
xe55	6	11	3	3	2	3	3	5	0	0	0	100	100
2e15_med	0	0	0	0	0	0	0	0	0	0	0	0	0
e55_loose1	0	0	0	0	0	0	0	0	0	0	0	0	0
e25i_med1	0	0	0	0	0	0	0	0	0	0	0	0	0
mu20	5	6	4	4	4	4	23	100	0	0	0	8	9
mu6	18	20	17	17	17	17	100	100	0	0	0	25	26
4j40	85	91	76	83	73	100	69	71	0	0	0	85	87
4j30	97	98	97	98	100	100	94	95	0	0	0	97	97
3j60v2	94	98	83	100	78	91	75	77	0	0	0	93	95
3j40	98	99	100	100	93	100	91	91	0	0	0	97	98
j200	41	100	15	18	15	19	16	22	0	0	0	62	73
j140	100	100	37	43	36	42	37	44	0	0	0	84	91
All	34	14	91	76	94	69	17	4	0	0	0	2	1

(b)

Figure 6.5.: (a) Trigger item overlap at LVL1 and (b) the chain overlap after all three levels, in hadronic $t\bar{t}$ events. The stated numbers represent the percentage of events selected by a trigger item given on the x-axis that is also triggered by a given item on the y-axis. In the bottom row, the numbers denote the total efficiency of the trigger item given on the x-axis. By definition, the values on the diagonal (bottom-left to top-right) have full overlap (100%, red), while uncorrelated item have zero overlap (0%, blue).

method used in this context is the so-called *tag-and-probe* method, based on the definition of a *probe-like* object, used to make the performance measurement, within a properly *tagged* sample of events.

6.3.1. Tag-and-Probe ethod

An exemplary and common application of the *tag-and-probe* method is the determination of the single lepton trigger efficiency using $Z \rightarrow \ell^+\ell^-$ events [108]. This approach is used to describe the principle of the method in more detail in the following. Amongst other applications, such as the single lepton trigger efficiency determination at the lower end of the lepton-p_T spectrum by using J/ψ and Υ resonances [43, pp. 141], it can also be applied to $t\bar{t}$ events to get a handle on the multi-jet trigger efficiency, as described below.

The name *tag and probe* can be understood by outlining the general recipe. In a first step, a subset of events, each containing an object (tag) satisfying a given trigger chain and reconstructed in the offline data, is chosen (*tagged*). In a following step, the complete event is reconstructed and an offline event selection is applied. While both the tag and the probe object are required to be present at the reconstruction level, no demands are put on the probe at the trigger level. At this point both the tag and the event selection criteria can be adjusted to minimise the background contribution to the subset of the events used to determine the probe trigger efficiency. In a final step, the efficiency of another trigger chain to select the probe can be tested (*probed*). Ideally the tag and the probe are independent, though not overlap-free, objects. Hereby independence denotes the fact that the probability for one item to trigger an event does not depend on the probability of the other item to do so and that none of the items is a subset of the other.

Figure 6.6(left) shows a graphical illustration of this recipe for the case of $Z \rightarrow \ell^+\ell^-$ events. In this exemplary case the tag could be given by an electron passing the e15i_medium chain[2] (I). After reconstruction and event selection (II), requiring an invariant mass from two reconstructed electrons within a certain window around the known Z boson mass m_Z, the efficiency of e.g. the e15_medium chain[3] could be determined using the reconstructed probe (III).

Using MC samples, the *tagging* (I) and the selection (II) steps can be swapped without changing the result of the efficiency determination (III). Due to this, a control sample, of selected but not necessarily *tagged* events, can be defined and used to test for possible influences of the tag definition on the efficiency determination, as described later. In real data, this is less straight forward, due to the fact that only events passing a given trigger chain are available for the analysis.

6.3.2. (Multi-)Jet Trigger Efficiency

An approach similar to the *tag-and-probe* method depicted in the previous section can be pursued to estimate the (multi-)jet trigger efficiency using semi-leptonic $t\bar{t}$ events. A measurement being necessary to analyse semi-leptonic $t\bar{t}$ events solely triggered by (multi-

---

[2] L1_EM13I_medium→L2_e15i_medium→EF_e15i_medium

[3] L1_EM13_medium→L2_e15_medium→EF_e15_medium

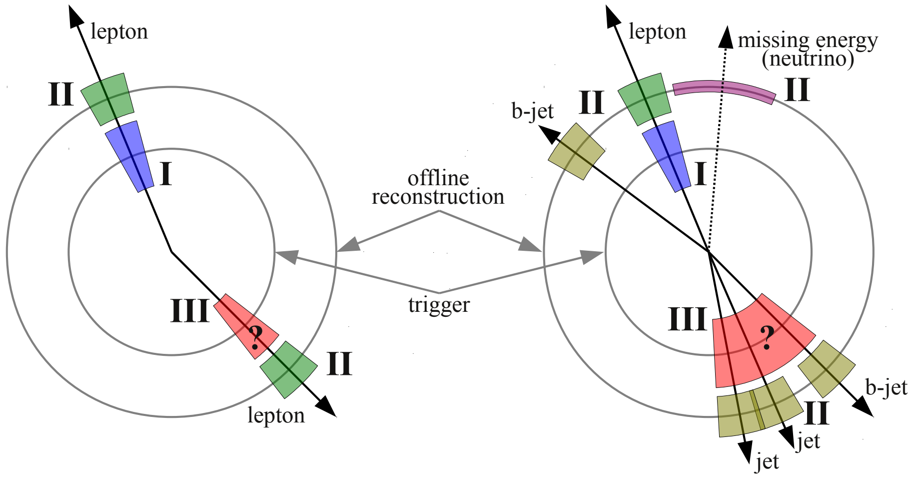

Figure 6.6.: Graphical illustration of the *tag-and-probe* method for $Z \to \ell^+\ell^-$ (left) and semi-leptonic $t\bar{t}$ (right). Hereby the roman numbers indicate the three steps of the *tag-and-probe* method: I - checking for a triggered tag object; II - event reconstruction (including tag and probe objects) and event selection; III - checking for the probe object in the trigger. The different colours indicate the various involved object types: blue - lepton at trigger level; green - reconstructed lepton; yellow - reconstructed jets; purple - reconstructed missing energy; red - probe object in question.

)jet trigger objects in data. With an offline event selection as introduced in Section 5.6, the reconstructed events feature both a high-p_{T} lepton, suitable for serving as a tag with tight selection cuts, and at least four jets to measure the (multi-)jet trigger efficiency. Vice versa the lepton trigger efficiency could be cross-checked using a combination of multi-jet and $E_{\mathrm{T}}^{\mathrm{miss}}$ triggers as tag. In this case including an $E_{\mathrm{T}}^{\mathrm{miss}}$ trigger in a combined tag object is necessary to veto the QCD background that would otherwise infest a sample selected only based on multi-jet triggers.

In analogy to the case of $Z \to \ell^+\ell^-$ events described above, Figure 6.6(right) shows a graphical illustration for the determination of the (multi-)jet trigger efficiency using semi-leptonic $t\bar{t}$ events, where a high-p_{T} lepton is used as tag (I), an event selection as discussed in Section 5.6 is required after the reconstruction of the event (II) and a three-jet trigger is *probed* (III).

The offline event selection, given by the invariant mass requirement in the $Z \to \ell^+\ell^-$ *tag-and-probe* method, is now replaced by a common semi-leptonic $t\bar{t}$ event selection, as introduced above. As a result of the selection, the chosen events contain a forth jet stemming from the bottom quark on the leptonic side of the event, allowing to extend the method to probe four-jet triggers. This is possible since the trigger decision is solely based on jet multiplicities, while directions are ignored.

To allow a valid determination of the trigger efficiency, it has to be shown that neither the tag nor the offline event selection have an influence (bias) on the measured probe efficiency as a result of using only a subset of the data (or MC sample). When applying the obtained efficiencies solely to $t\bar{t}$ events the bias due to the offline event selection, being the same one used for $t\bar{t}$ analyses, plays an subordinate role and a possible bias due to

Table 6.3.: Nomenclature used in Section 6.3.2, where $\mathrm{A} \cap \mathrm{B}$ denotes the intersection of two sets A and B. The index 'xyz' indicates the tag trigger chain used in the determination of the corresponding efficiency.

Variable	**Definition**
N^{total}	total number of events in MC sample or recorded in real data
N^{tagged}	number of events selected by the tag trigger chain
N^{selected}	number of events passing the preselection
N^{probed}	number of events selected by the probe trigger chain
$N^{\mathrm{t+s}}$	$N^{\mathrm{tagged}} \cap N^{\mathrm{selected}}$
$N^{\mathrm{t+p}}$	$N^{\mathrm{tagged}} \cap N^{\mathrm{probed}}$
$N^{\mathrm{s+p}}$	$N^{\mathrm{selected}} \cap N^{\mathrm{probed}}$
$N^{\mathrm{t+s+p}}$	$N^{\mathrm{tagged}} \cap N^{\mathrm{selected}} \cap N^{\mathrm{probed}}$
$\varepsilon^{\mathrm{xyz}} = \frac{N^{\mathrm{t+s+p}}}{N^{\mathrm{t+s}}}$	efficiency of the probe trigger chain determined using the *tag-and-probe* method with the common offline event selection
$\varepsilon^{\mathrm{direct}} = \frac{N^{\mathrm{s+p}}}{N^{\mathrm{s}}}$	efficiency of the probe trigger chain determined directly in the offline event selection sample, not requiring the tag (cross-check only available in MC)
N^{reco}	number of events in which the probe trigger object is reconstructed
$N^{\mathrm{t+s+r}}$	$N^{\mathrm{tagged}} \cap N^{\mathrm{selected}} \cap N^{\mathrm{reco}}$
$N^{\mathrm{t+r+p}}$	$N^{\mathrm{tagged}} \cap N^{\mathrm{reco}} \cap N^{\mathrm{probed}}$
$N^{\mathrm{s+r+p}}$	$N^{\mathrm{selected}} \cap N^{\mathrm{reco}} \cap N^{\mathrm{probed}}$
$N^{\mathrm{t+s+r+p}}$	$N^{\mathrm{tagged}} \cap N^{\mathrm{selected}} \cap N^{\mathrm{reco}} \cap N^{\mathrm{probed}}$
$\varepsilon^{\mathrm{xyz}}_{\mathrm{reco}} = \frac{N^{\mathrm{t+s+r+p}}}{N^{\mathrm{t+s+r}}}$	equal to $\varepsilon^{\mathrm{xyz}}$, but also ensuring the probe to be reconstructed (important in cases where the probe is more demanding than the offline event selection)
$\varepsilon^{\mathrm{direct}}_{\mathrm{reco}} = \frac{N^{\mathrm{s+r+p}}}{N^{\mathrm{s+r}}}$	equal to $\varepsilon^{\mathrm{direct}}$, but also ensuring the probe to be reconstructed (important in cases where the probe is more demanding than the offline event selection)

further selection by requiring the tag trigger becomes the principal item of investigation. The definitions of various quantities used in this study are introduced in Table 6.3.

Various combinations of possible tag and probe trigger chains have been investigated for the leptonic $t\bar{t}$ sample (see Section 4.5.1) and are summarised in Table 6.4. Hereby high-p_{T} muon triggers are preferred tag objects compared to electron triggers, due to the near absence of jets reconstructed as leptons (mainly electrons) in the selection. Again, this can be improved by requiring isolation criteria for electron triggers, still the muon selection is cleaner in that sense and induces less bias in the jet definition and trigger efficiency determination due to correlations with jet objects.

In addition multi-object triggers could be used as tag object, though the efficiency of these combined triggers would have to be determined using data. Due to the obvious correlation between missing energy and jet objects in the event, the latter being used for the calibration of the former, the use of $E_{\mathrm{T}}^{\mathrm{miss}}$ triggers as tag objects is far beyond trivial and for this reason not exploited within this thesis.

Table 6.4 states the total probe efficiency $\varepsilon^{\mathrm{xyz}}$ measured by the *tag-and-probe* method and $\varepsilon^{\mathrm{direct}}$ measured only requiring the offline event selection, as defined in Table 6.3. Also stated are $\varepsilon^{\mathrm{xyz}}_{\mathrm{reco}}$ and $\varepsilon^{\mathrm{direct}}_{\mathrm{reco}}$ denoting the efficiencies obtained from the *tag-and-probe* method and directly with the additional requirement of a reconstructed probe object. Since the probe object definition is in most cases more demanding, e.g. in terms of p_{T}-thresholds,

Table 6.4.: List of tag and probe chains investigated in the leptonic $t\bar{t}$ sample along with the total probe efficiency measured by the *tag-and-probe* method and directly in the offline event selection sample with ($\varepsilon_{\text{reco}}^{\text{xyz}}$ and $\varepsilon_{\text{reco}}^{\text{direct}}$) and without ($\varepsilon^{\text{xyz}}$ and $\varepsilon^{\text{direct}}$) the additional requiring of a reconstructed probe object. The numbers are derived using event trigger flags not requiring matching between the reconstructed and the trigger probe object.

Probe	$\varepsilon^{\text{direct}}$	$\varepsilon^{\text{mu20}}$	$\varepsilon^{\text{mu40}}$	$\varepsilon_{\text{reco}}^{\text{direct}}$	$\varepsilon_{\text{reco}}^{\text{mu20}}$	$\varepsilon_{\text{reco}}^{\text{mu40}}$
3j40	0.974±0.002	0.958±0.005	0.958±0.006	0.965±0.002	0.953±0.004	0.952±0.005
3j60v2	0.818±0.006	0.763±0.010	0.770±0.012	0.991±0.001	0.988±0.003	0.989±0.004
3j80	0.371±0.007	0.317±0.010	0.332±0.014	0.969±0.004	0.968±0.007	0.966±0.010
4j30	0.950±0.003	0.915±0.006	0.914±0.008	0.980±0.001	0.972±0.003	0.971±0.005
4j40	0.738±0.007	0.596±0.011	0.596±0.014	0.930±0.003	0.913±0.008	0.912±0.010
4j80	0.138±0.005	0.100±0.007	0.106±0.009	0.952±0.010	0.941±0.022	0.945±0.027

mu20 = L1_MU20→L2_mu20→EF_mu20, mu40 = L1_MU40→L2_mu40→EF_mu40

3j40 = L1_3J20→L2_3j30→EF_3j40, 3j60v2 = L1_3J20→L2_3j30→EF_3j60v2

3j80 = L1_3J40→L2_3j60→EF_3j80, 4j30 = L1_4J10→L2_4j20→EF_4j30

4j40 = L1_4J20→L2_4j30→EF_4j40, 4j80 = L1_4J40→L2_4j60→EF_4j80

than the offline event selection, $\varepsilon_{\text{reco}}^{\text{xyz}}$ will be used as the trigger efficiency in an analysis of semi-leptonic $t\bar{t}$ events solely triggered by the corresponding probe trigger object in data. As an example, even if an offline selected event will contain at least four jets, these four jets will not necessarily surpass the threshold of a high-p_{T} multi-jet trigger item. By definition $\varepsilon_{\text{reco}}^{\text{xyz}}$ and $\varepsilon_{\text{reco}}^{\text{direct}}$ will be higher than the efficiencies derived omitting the reconstruction requirement, and the discrepancy will rise with increasing threshold values.

While the numbers stated in Table 6.4 are derived from event trigger flags not requiring matching between the reconstructed and the trigger probe object, the values in Table 6.5 are calculated using individual trigger objects on each level matched to the reconstructed probe object, using a matching procedure as introduced in Section 5.5. Due to the matching procedure involved in the latter case, the efficiencies stated in Table 6.5 are, as expected, always lower than those in Table 6.4. While the event-trigger-flag based efficiency is more useful for a possible analysis of semi-leptonic $t\bar{t}$ events solely triggered by (multi-)jet trigger objects in data, the trigger-object based efficiency might be of more interest from a trigger point of view as it allows to study the performance of a trigger item e.g. as a function of the kinematics of the objects in question.

Using the event trigger flags, slight discrepancies between $\varepsilon^{\text{direct}}$ and ε^{xyz} can be found in cases where the probe trigger objects are not required by the offline event selection (see Section 5.6). This disagreement, only a few percent in case of low threshold trigger chains such as 3j40 or 4j30, is expected since the offline event selection does not ensure the existence of all probe trigger objects in the reconstructed event, as indicated above. Adding this requirement, used for the calculation of $\varepsilon_{\text{reco}}^{\text{direct}}$ and $\varepsilon_{\text{reco}}^{\text{xyz}}$, the efficiencies agree within errors in most of the cases. The level of agreement improves even further when requiring a matching between the reconstructed objects and the individual trigger objects on each level, as described above.

In addition to the total efficiency, the differential efficiency as a function of either the leading or N^{th} jet p_{T} ($p_{\text{T}}^{\text{1st}}$ and $p_{\text{T}}^{\text{Nth}}$) and the sum of all N jet-p_{T} ($\sum p_{\text{T}}$) for a N-jet probe

Table 6.5.: List of tag and probe chains investigated in the leptonic $t\bar{t}$ sample along with the total probe efficiency measured by the *tag-and-probe* method and directly in the offline event selection sample with ($\varepsilon^{\mathrm{xyz}}_{\mathrm{reco}}$ and $\varepsilon^{\mathrm{direct}}_{\mathrm{reco}}$) and without ($\varepsilon^{\mathrm{xyz}}$ and $\varepsilon^{\mathrm{direct}}$) the additional requiring of a reconstructed probe object. The numbers are derived using individual trigger objects on each level matched to the reconstructed objects.

Probe	$\varepsilon^{\mathrm{direct}}$	$\varepsilon^{\mathrm{mu20}}$	$\varepsilon^{\mathrm{mu40}}$	$\varepsilon^{\mathrm{direct}}_{\mathrm{reco}}$	$\varepsilon^{\mathrm{mu20}}_{\mathrm{reco}}$	$\varepsilon^{\mathrm{mu40}}_{\mathrm{reco}}$
3j40	0.861±0.005	0.865±0.008	0.866±0.010	0.852±0.003	0.842±0.006	0.840±0.009
3j60v2	0.407±0.008	0.413±0.011	0.428±0.015	0.871±0.005	0.867±0.009	0.868±0.012
3j80	0.150±0.005	0.153±0.008	0.165±0.011	0.790±0.009	0.791±0.017	0.789±0.022
4j30	0.747±0.007	0.755±0.010	0.757±0.013	0.852±0.004	0.837±0.008	0.835±0.010
4j40	0.385±0.007	0.391±0.011	0.400±0.014	0.749±0.006	0.741±0.012	0.742±0.016
4j80	0.029±0.003	0.030±0.004	0.033±0.005	0.699±0.022	0.691±0.042	0.701±0.054

mu20 = L1_MU20→L2_mu20→EF_mu20, mu40 = L1_MU40→L2_mu40→EF_mu40

3j40 = L1_3J20→L2_3j30→EF_3j40, 3j60v2 = L1_3J20→L2_3j30→EF_3j60v2

3j80 = L1_3J40→L2_3j60→EF_3j80, 4j30 = L1_4J10→L2_4j20→EF_4j30

4j40 = L1_4J20→L2_4j30→EF_4j40, 4j80 = L1_4J40→L2_4j60→EF_4j80

chain has been investigated and is illustrated in Figure 6.7 for the exemplary combination of L1_MU20→L2_mu20→EF_mu20 as tag and L1_3J40→L2_3j60→EF_3j80 as probe chain. Both efficiencies, based on the event trigger flags (unstarred) and the individual matched trigger objects (starred), are shown for the case where the probe object is required to be reconstructed. It has to be noted that when plotting $p_{\mathrm{T}}^{\mathrm{Nth}}$ and $\sum p_{\mathrm{T}}$ only events that actually contain at least N jets are filled, while the remaining events are omitted. In the given example this effect can be neglected since all events are required to pass the preselection and thereby contain one more jet than demanded by the trigger chain (four vs. three).

The discrepancy between efficiencies derived using the event trigger flags and those using the decision based on individual trigger objects, is also apparent in all three figures and is caused by the implicit matching requirement in the latter case, as described above. In addition the matching requirement reduces the available statistics and therefore increases the uncertainties. Apart from that, the efficiency determined using the *tag-and-probe* method and the direct measurement (only a MC cross-check) agree within errors also as a function of each of the three variables.

As can be seen in Tables 6.6 and 6.7 as well as Figure 6.8, including the major backgrounds introduced in Section 4.5 results in increased discrepancies between the efficiencies obtained with the *tag-and-probe* method and those measured directly only requiring the preselection. This leads to the conclusion that background events entering the preselection sample behave slightly different compared to semi-leptonic $t\bar{t}$. One possible approach to minimise this effect, though not studied in this thesis, could be to reconstruct the mass of the $t\bar{t}$ system and subtract the background by using side bands in the resulting mass plot.

It could be shown that by using a *tag-and-probe*-like method in semi-leptonic $t\bar{t}$ events the trigger efficiency of multi-jet trigger chains can be approximated from data. Knowing the trigger efficiency of the tag trigger chains from other data-driven methods, such as *tag and probe* in $Z \to \ell^+\ell^-$ events, one can derive multi-jet trigger efficiencies to be used

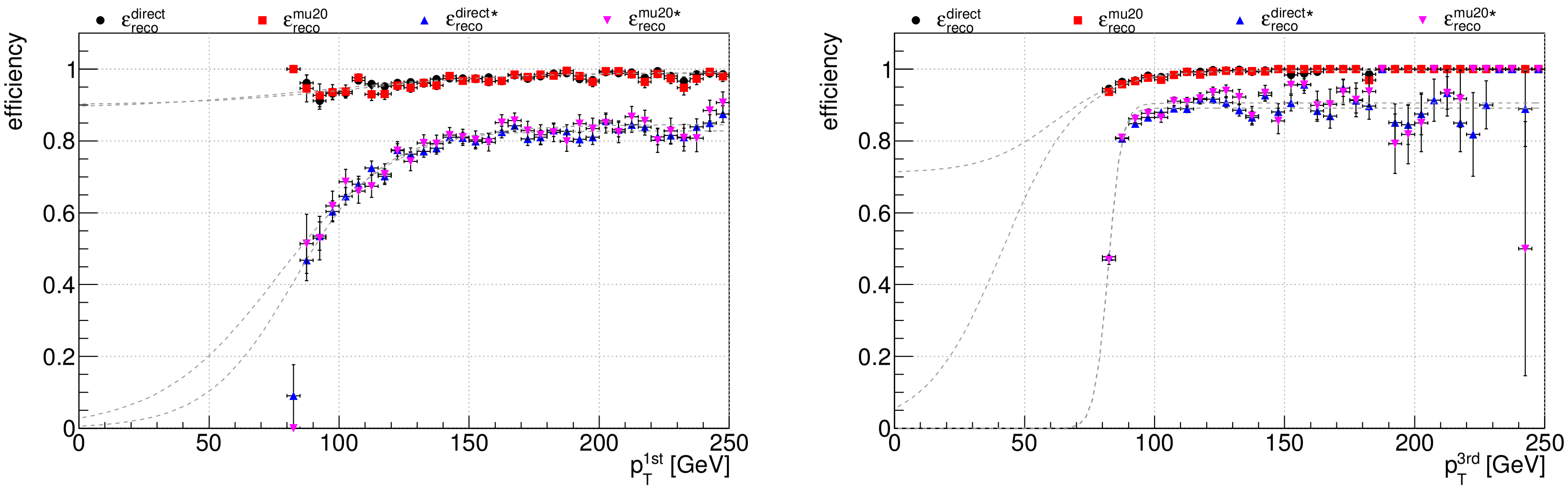

(a)

(b)

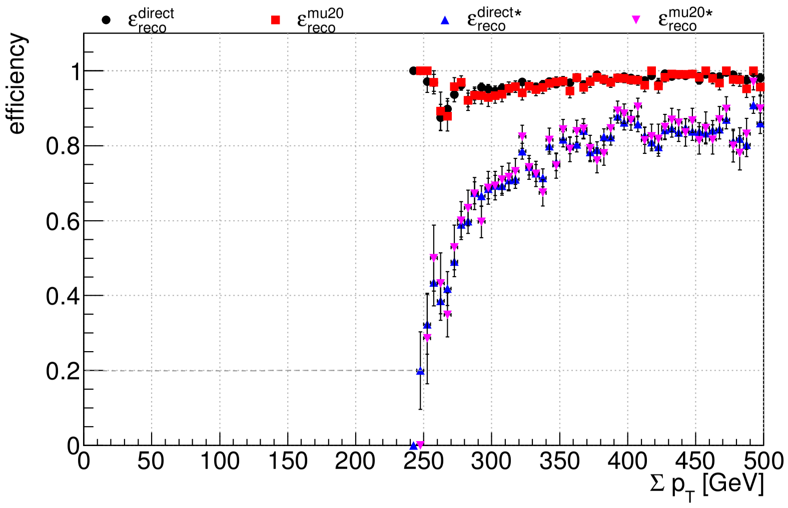

(c)

Figure 6.7.: Differential efficiency in the leptonic $t\bar{t}$ sample as a function of either (a) the leading or (b) 3rd jet p_T and (c) the sum of all three jets ($\sum p_T$) for the exemplary combination of L1_MU20→L2_mu20→EF_mu20 as tag and L1_3J40→L2_3j60→EF_3j80 as probe chain. The starred efficiencies represent efficiencies derived using the decision based on trigger objects matched to the reconstructed objects, while the unstarred plots show those based on the event trigger flags, as described in the text.

Table 6.6.: List of tag and probe chains investigated in a data-like sample mixture along with the total probe efficiency measured by the *tag-and-probe* method and directly in the offline event selection sample with ($\varepsilon^{\text{xyz}}_{\text{reco}}$ and $\varepsilon^{\text{direct}}_{\text{reco}}$) and without ($\varepsilon^{\text{xyz}}$ and $\varepsilon^{\text{direct}}$) the additional requiring of a reconstructed probe object. The numbers are derived using event trigger flags not requiring matching between the reconstructed and the trigger probe object.

Probe	$\varepsilon^{\text{direct}}$	$\varepsilon^{\text{mu20}}$	$\varepsilon^{\text{mu40}}$	$\varepsilon^{\text{direct}}_{\text{reco}}$	$\varepsilon^{\text{mu20}}_{\text{reco}}$	$\varepsilon^{\text{mu40}}_{\text{reco}}$
3j40	0.970±0.002	0.941±0.004	0.961±0.006	$0.810\pm{<10^{-3}}$	0.908±0.001	0.956±0.001
3j60v2	0.832±0.004	0.742±0.007	0.782±0.012	$0.953\pm{<10^{-3}}$	0.979±0.001	0.984±0.001
3j80	0.395±0.005	0.300±0.008	0.342±0.014	$0.929\pm{<10^{-3}}$	0.965±0.001	0.952±0.003
4j30	0.932±0.003	0.873±0.006	0.918±0.008	$0.864\pm{<10^{-3}}$	0.954±0.001	0.970±0.001
4j40	0.732±0.004	0.518±0.008	0.593±0.014	$0.768\pm{<10^{-3}}$	0.738±0.002	0.800±0.005
4j80	0.076±0.003	0.055±0.004	0.100±0.009	0.895±0.001	0.911±0.005	0.901±0.010

mu20 = L1_MU20→L2_mu20→EF_mu20, mu40 = L1_MU40→L2_mu40→EF_mu40
3j40 = L1_3J20→L2_3j30→EF_3j40, 3j60v2 = L1_3J20→L2_3j30→EF_3j60v2
3j80 = L1_3J40→L2_3j60→EF_3j80, 4j30 = L1_4J10→L2_4j20→EF_4j30
4j40 = L1_4J20→L2_4j30→EF_4j40, 4j80 = L1_4J40→L2_4j60→EF_4j80

Table 6.7.: List of tag and probe chains investigated in a data-like sample mixture along with the total probe efficiency measured by the *tag-and-probe* method and directly in the offline event selection sample with ($\varepsilon^{\text{xyz}}_{\text{reco}}$ and $\varepsilon^{\text{direct}}_{\text{reco}}$) and without ($\varepsilon^{\text{xyz}}$ and $\varepsilon^{\text{direct}}$) the additional requiring of a reconstructed probe object. The numbers are derived using individual trigger objects on each level matched to the reconstructed probe object.

Probe	$\varepsilon^{\text{direct}}$	$\varepsilon^{\text{mu20}}$	$\varepsilon^{\text{mu40}}$	$\varepsilon^{\text{direct}}_{\text{reco}}$	$\varepsilon^{\text{mu20}}_{\text{reco}}$	$\varepsilon^{\text{mu40}}_{\text{reco}}$
3j40	0.821±0.004	0.801±0.007	0.873±0.010	$0.638\pm{<10^{-3}}$	0.770±0.001	0.788±0.002
3j60v2	0.361±0.005	0.430±0.008	0.433±0.014	$0.765\pm{<10^{-3}}$	0.828±0.001	0.782±0.003
3j80	0.139±0.004	0.154±0.006	0.159±0.010	$0.729\pm{<10^{-3}}$	0.774±0.003	0.711±0.006
4j30	0.663±0.005	0.636±0.008	0.770±0.012	$0.634\pm{<10^{-3}}$	0.768±0.001	0.775±0.003
4j40	0.268±0.004	0.322±0.008	0.406±0.014	$0.568\pm{<10^{-3}}$	0.608±0.002	0.673±0.005
4j80	0.020±0.001	0.024±0.003	0.032±0.005	0.633±0.001	0.705±0.008	0.700±0.016

mu20 = L1_MU20→L2_mu20→EF_mu20, mu40 = L1_MU40→L2_mu40→EF_mu40
3j40 = L1_3J20→L2_3j30→EF_3j40, 3j60v2 = L1_3J20→L2_3j30→EF_3j60v2
3j80 = L1_3J40→L2_3j60→EF_3j80, 4j30 = L1_4J10→L2_4j20→EF_4j30
4j40 = L1_4J20→L2_4j30→EF_4j40, 4j80 = L1_4J40→L2_4j60→EF_4j80

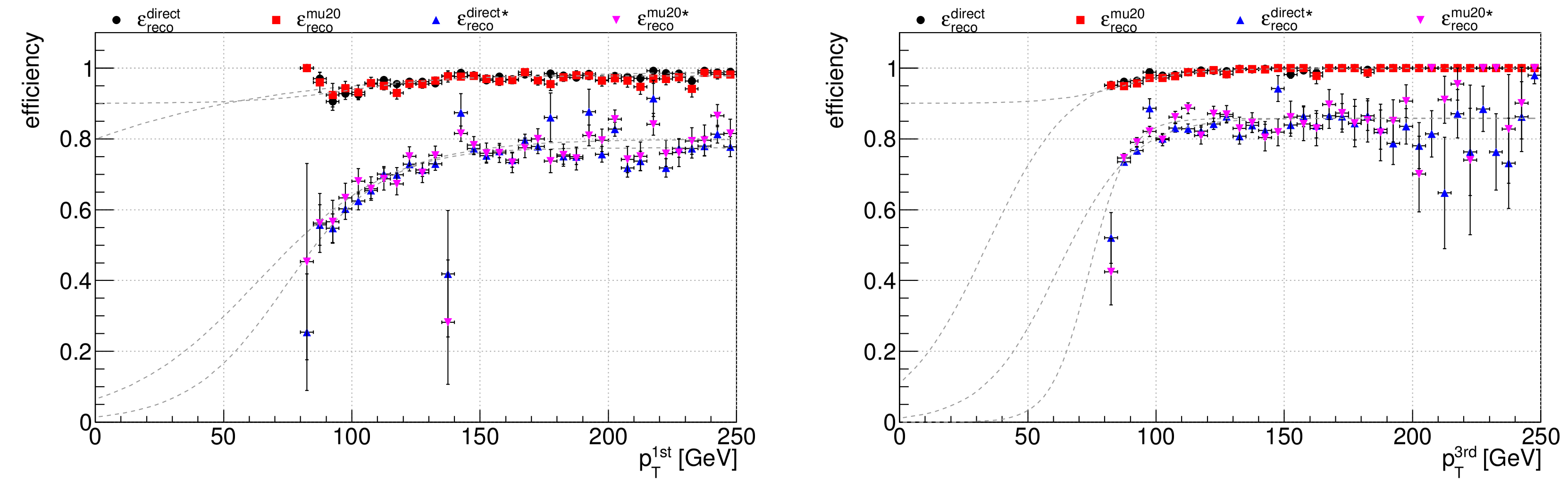

(a)

(b)

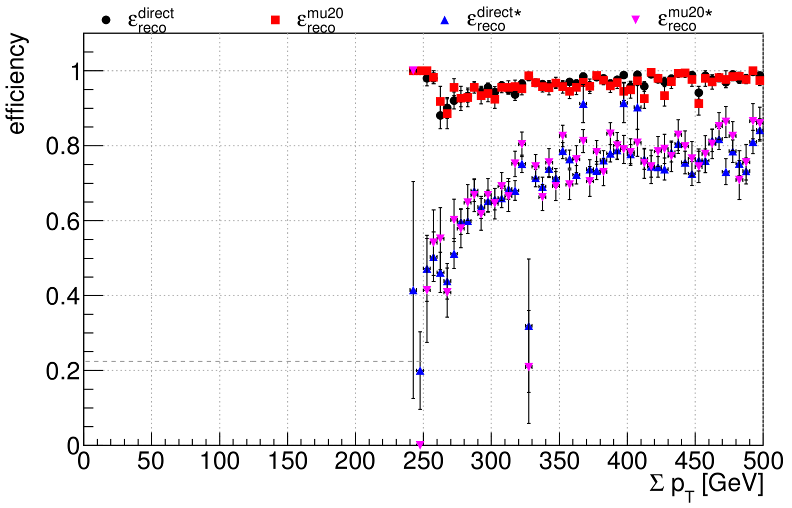

(c)

Figure 6.8.: Differential efficiency in a data-like sample mixture as a function of either (a) the leading or (b) 3rd jet p_{T} and (c) the sum of all three jets ($\sum p_{\mathrm{T}}$) for the exemplary combination of L1_MU20→L2_mu20→EF_mu20 as tag and L1_3J40→L2_3j60→EF_3j80 as probe chain. The starred efficiencies represent efficiencies derived using the decision based on trigger objects matched to the reconstructed objects, while the unstarred plots show those based on the event trigger flags, as described in the text.

in analyses based on a semi-leptonic $t\bar{t}$ preselection without further corrections. To apply the obtained efficiencies to other processes the selection efficiency of the semi-leptonic $t\bar{t}$ preselection has to be unfolded. While data-driven techniques for the determination of this selection efficiency are most desirable, as a first approach it can be obtained from MC simulations.

With the arrival of sufficient collision data this method could be tested in combination with data-driven techniques to measure the tag trigger chain efficiencies and cross-checked e.g. with bootstrap methods in which a measurement of the relative efficiency of low versus high-p_T trigger chains is used to calculate the efficiency of high-p_T trigger chains from the measured efficiency of the low-p_T trigger chain. In addition single jet trigger efficiencies obtained from data can be folded into multi-jet trigger efficiencies using MC simulations taking into account possible correlation amongst the jets. This could serve as another possible cross-check for the method presented.

Chapter 7.

Estimation of the W+Jets Background in Top-Antitop Events

The importance of the top quark, both for a better understanding and testing of the *Standard Model* as well as a key ingredient for the discovery of possible *new physics*, has been discussed previously in this thesis. To be able to accurately measure the properties of the top quark it is necessary to also have a good, if not better, understanding of background. In the case of the semi-leptonic channel in top pair events, the so-called *Golden Channel* for top-quark physics, the major backgrounds are given by W+Jets, single-top, QCD-multi-jet and Z+Jets events, in the order of importance as introduced in Section 2.2. Especially the background stemming from W+Jets events is, due to its nearly identical topology, hard to veto. In addition, today's MC generators are unreliable in predicting the cross-section of W boson production associated with a large number of jets and theoretical calculations at higher orders are only slowly emerging. The uncertainty on the exclusive cross-section of the W+Jets background obtained using ALPGEN, has been found to be as large as 50% [109], especially for jet multiplicities of four and above. It is therefore necessary to develop data-driven methods to estimate the background contribution arising from W+Jets events.

In this chapter, a data-driven approach for the estimation of the W+Jets background in (semi-leptonic) $t\bar{t}$ events is discussed, that can serve as an alternative and orthogonal method to current techniques taking advantage of e.g. the production asymmetry between W^+ and W^- bosons or the ratio between W and Z bosons as a function of the number of associated jets. The former method is based on the fact that W bosons produced in $t\bar{t}$ events occur in equal amounts for both charges, while the direct production of W bosons features a charge asymmetry in favour of positively charged W bosons at all jet multiplicities at a proton-proton collider such as the LHC. The number of W+Jets events contaminating a sample defined by a $t\bar{t}$ selection can be estimated by measuring the asymmetry in the sample and using a ratio of events with opposite W boson charge estimated from W+Jets MC samples. The W/Z ratio method is utilising the assumption that the ratio of event numbers in a signal region and in a control region differs only by a scaling factor between W and Z boson events, due to the mass difference between both bosons. Hereby the signal region is typically defined by a $t\bar{t}$ selection, while the control region is usually given by events with exactly one jet. The number of W+Jets events in the signal region is then extracted by measuring the yield of Z boson events in both regions as well as that of W bosons in the control region and a scaling factor derived from MC simulations. Both methods are expected to yield total uncertainties of below 40% already with about 50 pb^{-1} of integrated luminosity at $\sqrt{s} = 7$ TeV.

The method presented in this chapter, originally introduced by Pavlunin and Stuart [110] in 2008, is the first application of an alternative approach in ATLAS, using fully simulated MC samples as introduced in Section 4.2 instead of an idealised detector geometry as in [110]. After a general introduction further developments, e.g. on the treatment of imperfect signal and background regions, are described in detail.

7.1. Method Overview

The rationale of the method is to define W+Jets background dominated control regions in preselected data and to extrapolate the W+Jets background contribution measured there into the signal dominated regions. While the decay products of top quarks produced in pairs, also due to the large mass of the top quark, distribute nearly uniform over solid angle and are therefore enhanced at central rapidity, the lighter W boson tends to be boosted along the beam direction, hence distributed over a wide rapidity range. Since the rapidity of the W boson, either produced directly or coming from a top quark decay, cannot be reconstructed without ambiguity, due to the neutrino in the final state, the pseudo-rapidity of the lepton, stemming from the W boson decay, is used instead, as it features a similar angular distribution due to the boost and the negligible mass of the lepton. In addition the mean jet multiplicity in top pair events is predicted to be larger compared to direct W+Jets production. Therefore the above mentioned background dominated control regions can be defined as regions in phase space with low jet multiplicity and large lepton pseudo-rapidity. In the following low (high) jet multiplicity N_{jet} is defined as $1 \leq N_{\mathrm{jet}} \leq 2$ ($5 \leq N_{\mathrm{jet}} \leq 8$) and small (large) lepton pseudo-rapidity as $|\eta^{\mathrm{lep}}| \leq 1$ ($1.5 \leq |\eta^{\mathrm{lep}}| \leq 2.5$). The number of events (yield) falling in a small (central) and large (forward) lepton pseudo-rapidity region, for a given N_{jet}, are denoted $Y^{\mathrm{C}}_{N_{\mathrm{jet}}}$ and $Y^{\mathrm{F}}_{N_{\mathrm{jet}}}$, respectively.

The above mentioned preselected sample is represented by events with exactly one reconstructed lepton (electron or muon), as defined in Sections 5.1 and 5.2, and a reconstructed transverse mass of the leptonic W boson

$$m_T^W = \sqrt{2 \cdot p_{\mathrm{T}}^{\mathrm{lep}} \cdot E_{\mathrm{T}}^{\mathrm{miss}} \cdot (1 - \cos \Delta\phi)} \tag{7.1}$$

within a window of ±25 GeV around the current world average of the W boson mass (80.398 GeV [57]), representing the position of the Jacobian edge in an ideal transverse W boson mass distribution. Hereby $p_{\mathrm{T}}^{\mathrm{lep}}$ denotes the transverse momentum of the lepton, the missing transverse energy $E_{\mathrm{T}}^{\mathrm{miss}}$ is used in exchange for the unavailable neutrino p_{T} and $\Delta\phi$ represents the angle between the directions of $p_{\mathrm{T}}^{\mathrm{lep}}$ and $E_{\mathrm{T}}^{\mathrm{miss}}$ in the x-y-plane. Figure 7.1 shows the lepton pseudo-rapidity distribution for selected leptonic $t\bar{t}$ and W+Jets events, separately for electrons and muons. Clearly visible are the drops in efficiency due to the ATLAS detector geometry around $\eta = 1.4$ for both electrons and muons and $\eta = 0$ for muons only. The jet multiplicity distributions for both samples are illustrated in Figure 7.2(a). The m_T^W distribution for both the W+Jets and the leptonic $t\bar{t}$ sample before applying the m_T^W-cut is shown in Figure 7.2(b).

Using the regions defined above, a ratio $R_{N_{\mathrm{jet}}}$ can be defined as the fraction of events

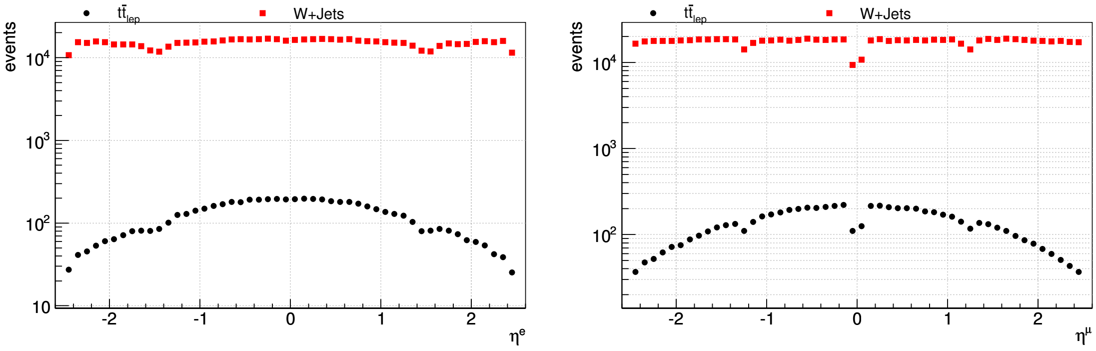

(a) (b)

Figure 7.1.: Pseudo-rapidity distribution of (a) electrons and (b) muons for selected leptonic $t\bar{t}$ and W+Jets events. MC sample: $\sqrt{s} = 10$ TeV, $\mathcal{L} = 100$ pb^{-1}.

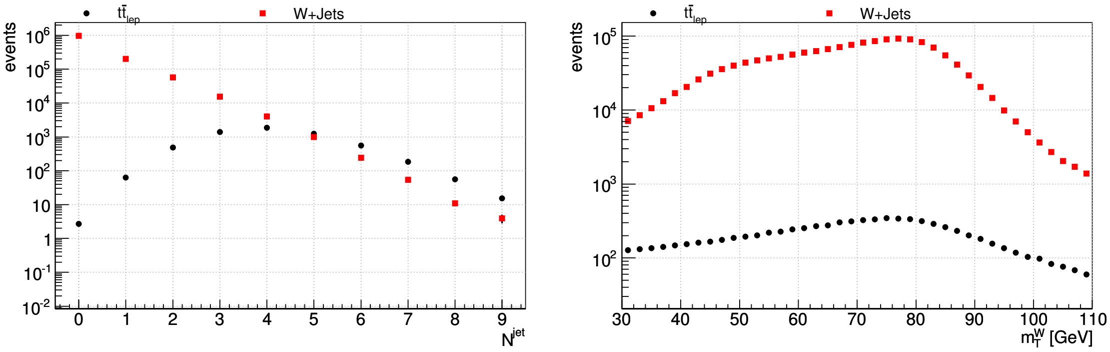

(a) (b)

Figure 7.2.: (a) Jet multiplicity (N_{jet}) distribution for selected leptonic $t\bar{t}$ and W+Jets events. (b) Transverse mass distribution of the leptonic W boson before applying the mass window cut for W+Jets and leptonic $t\bar{t}$ events. MC sample: $\sqrt{s} = 10$ TeV, $\mathcal{L} = 100$ pb^{-1}.

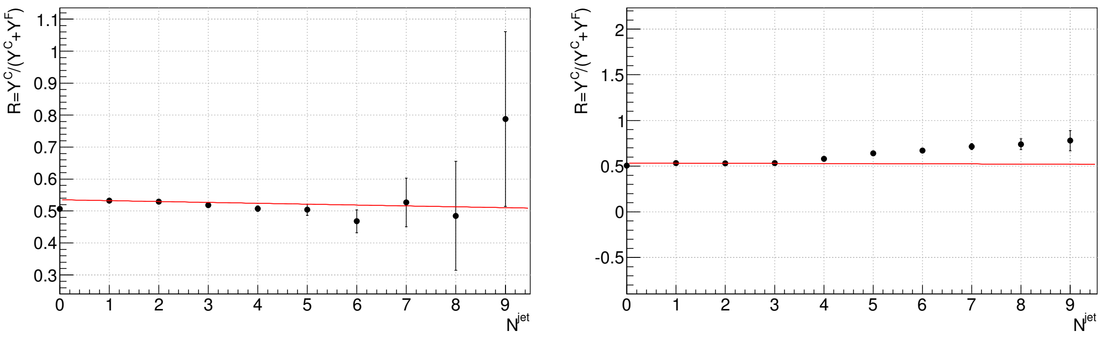

(a) (b)

Figure 7.3.: Ratio $R_{N_{\text{jet}}}$ as a function of N_{jet}, both for (a) a pure W+Jets sample and (b) a cross-section weighted mixture of leptonic $t\bar{t}$ and W+Jets events. The linear fit used for the extrapolation is illustrated by the solid red line. MC sample: $\sqrt{s} = 10$ TeV, $\mathcal{L} = 100$ pb^{-1}.

falling into the central region $Y^{\text{C}}_{N_{\text{jet}}}$ relative to all events in the central and forward region $(Y^{\text{C}}_{N_{\text{jet}}} + Y^{\text{F}}_{N_{\text{jet}}})$:

$$R_{N_{\text{jet}}} = \frac{Y^{\text{C}}_{N_{\text{jet}}}}{Y^{\text{C}}_{N_{\text{jet}}} + Y^{\text{F}}_{N_{\text{jet}}}}. \tag{7.2}$$

The extrapolation from low to high jet multiplicity is then done, assuming that $R_{N_{\text{jet}}}$ can be predicted stably, by applying a first order polynomial[1] to this ratio as a function of N_{jet} in the low jet multiplicity bins. As can be seen in Figure 7.3(a), showing the ratio as a function of N_{jet} for a pure W+Jets sample, the expected values of the ratio in high jet multiplicity bins can be reasonably well described by using a first order polynomial. An estimated central yield $Y^{\text{C, est}}_{N_{\text{jet}}}$ is then extracted using a ratio $R^{\text{fit}}_{N_{\text{jet}}}$ given by the polynomial at high jet multiplicities and by inverting the formula, such that

$$Y^{\text{C, est}}_{N_{\text{jet}}} = \frac{R^{\text{fit}}_{N_{\text{jet}}}}{1 - R^{\text{fit}}_{N_{\text{jet}}}} \cdot Y^{\text{F}}_{N_{\text{jet}}}. \tag{7.3}$$

To illustrate the basic principle of the method, a MC sample containing a cross-section weighted mixture of only leptonic $t\bar{t}$ (signal) and W+Jets (background) events has been created. This way the basics of the method can be tested without the influence of additional systematic uncertainties arising from additional background events. Figure 7.3 depicts the ratio $R_{N_{\text{jet}}}$, given in Equation (7.2), both for a pure W+Jets MC sample and the above mentioned mixture of leptonic $t\bar{t}$ and W+Jets events. As expected for the pure W+Jets sample, the ratio is fairly constant over jet multiplicities up to about eight, at which point the low statistics starts causing large uncertainties. The ratio is roughly centred around the expected value of 1/2, reflecting the fact that the η distribution is flat for all N_{jet} and both regions cover the same range of two units in η. The difference

---

[1] Fitted in cases of more than two points used in the extrapolation.

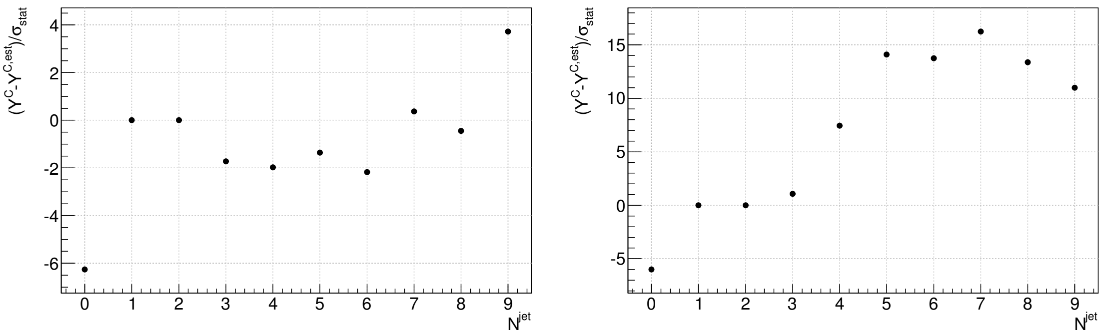

(a)

(b)

Figure 7.4.: Pull distribution of the central yield for (a) W+Jets events and (b) the mixture. MC sample: $\sqrt{s} = 10$ TeV, $\mathcal{L} = 100$ pb^{-1}.

between the extrapolated fit and the points in the case of the mixture reflects the additional $t\bar{t}$ contribution and will be utilised in the following. Figure 7.4 shows the so-called pull P of the central yield, defined as $P = (Y^{\mathrm{C}}_{N_{\mathrm{jet}}} - Y^{\mathrm{C,\ est}}_{N_{\mathrm{jet}}})/\sigma_{\mathrm{stat}}$, with $Y^{\mathrm{C,\ est}}_{N_{\mathrm{jet}}}$ given in Equation (7.3), as a function of N_{jet}, further illustrating the excess. From the deviations from zero in Figure 7.4(a), it can already be concluded that extrapolation is not perfect in describing the W+Jets background and will lead to a slight over-estimation especially at jet multiplicities from three to six. The same effect can be seen at the $N_{\mathrm{jet}} = 0$ bin, where this is of more importance for the definition of the low jet multiplicity region. As this feature is also observed when applying the method on MC truth information, it is unlikely to be caused by detector effects, though the exact reason is not fully understood yet.

In a final step the known cross-section of the leptonic $t\bar{t}$ sample $\sigma_{t\bar{t}_{\mathrm{lep}}}$ (about 217.1 pb at 10 TeV, see Table 4.1) can be compared with a cross-section σ_{basic} extracted from the difference between the number of observed events ($Y^{\mathrm{C}}_{N_{\mathrm{jet}}}$) and the number of estimated background events ($Y^{\mathrm{C,\ est}}_{N_{\mathrm{jet}}}$) in the signal region via

$$\sigma_{\mathrm{basic}} = \frac{\sum_{N_{\mathrm{jet}}} \left(Y^{\mathrm{C}}_{N_{\mathrm{jet}}} - Y^{\mathrm{C,\ est}}_{N_{\mathrm{jet}}} \right)}{\varepsilon^{\mathrm{C},\ t\bar{t}_{\mathrm{lep}}} \cdot \mathcal{L} \cdot \varepsilon^{\mathrm{ext},\ t\bar{t}_{\mathrm{lep}}} \cdot \varepsilon^{\mathrm{sel},\ t\bar{t}_{\mathrm{lep}}}}, \tag{7.4}$$

where $\mathcal{L}$ denotes the integrated luminosity of the used data or MC sample, $\varepsilon^{\mathrm{ext},\ t\bar{t}_{\mathrm{lep}}}$ is the fraction of leptonic $t\bar{t}$ events falling into the jet multiplicity bins used for the cross-section calculation (sum in numerator of Equation (7.4)), $\varepsilon^{\mathrm{C},\ t\bar{t}_{\mathrm{lep}}}$ denotes the fraction of leptonic $t\bar{t}$ events falling into the central region and $\varepsilon^{\mathrm{sel},\ t\bar{t}_{\mathrm{lep}}}$ states the fraction of offline selected leptonic $t\bar{t}$ events. These fractions require prior knowledge of the leptonic $t\bar{t}$ signal sample and have to be obtained from MC. Still, with the exception of the extrapolation, no prior knowledge of the W+Jets sample is needed. Using Equation (7.4) the estimated cross-section amounts to $\sigma_{\mathrm{basic}} = 129 \pm 14$ (stat.) pb, deviating significantly from the expected cross-section of the leptonic $t\bar{t}$ sample of $\sigma_{t\bar{t}_{\mathrm{lep}}} = 217.1$ pb. Hereby, $\varepsilon^{\mathrm{ext},\ t\bar{t}_{\mathrm{lep}}}$ and $\varepsilon^{\mathrm{sel},\ t\bar{t}_{\mathrm{lep}}}$ have been estimated, using MC simulations, to be $\varepsilon^{\mathrm{ext},\ t\bar{t}_{\mathrm{lep}}} = 0.348 \pm 0.006$ and

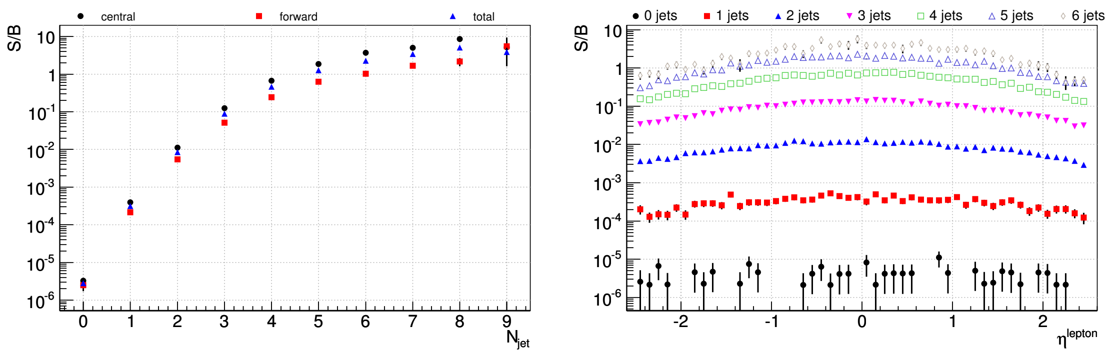

(a)

(b)

Figure 7.5.: Signal-over-background (S/B=leptonic $t\bar{t}/W$+Jets) ratio as function of (a) jet multiplicity and (b) η for jet multiplicities up to six, using the default setup as introduced in the text. The ratio as function of jet multiplicity is stated separately for the central, forward and total pseudo-rapidity region. MC sample: $\sqrt{s} = 10$ TeV, $\mathcal{L} = 100$ pb^{-1}.

$\varepsilon^{\text{sel},\, t\bar{t}_{\text{lep}}} = 0.269 \pm 0.003$. To estimate the uncertainty on the cross-section an ensemble test consisting of 250 toy-MC samples was performed. Hereby, the distributions are cloned following the given shapes with event numbers according to a Poissonian distribution around the expected yield and the measurement is repeated. The mean and the root mean square (RMS) of the resulting distribution of calculated cross-sections are taken as the actual result and its statistical uncertainty. The sizeable offset is due to the obviously significant forward contribution of leptonic $t\bar{t}$ events in the forward pseudo-rapidity region. This effect and a possible extension to consider this contamination is described in the following section.

7.2. Method Extension

As can be seen in Figures 7.5(a) and 7.5(b), which show the signal-over-background (S/B = leptonic $t\bar{t}/W$+Jets) ratio as a function of N_{jet} and η for jet multiplicities up to six, respectively, the assumption of a signal-free control region is not entirely valid. While for low jet multiplicities ($N_{\text{jet}} \leq 2$) the sample is dominated by background by at least two orders of magnitude both in the central and forward pseudo-rapidity region, the assumption is partly false in the forward region for higher jet multiplicities (S/B of about one for $N_{\text{jet}} \leq 4$). This effect, a signal contamination of the forward control region ($Y^{\text{F},\, t\bar{t}_{\text{lep}}}_{N_{\text{jet}}}$), has to be taken into account when estimating the number of background events in the central signal region ($Y^{\text{C},\, W\text{+Jets}}_{N_{\text{jet}}}$).

This can be achieved for the mixture of leptonic $t\bar{t}$ and W+Jets events, by defining the total central ($Y_{N_\text{jet}}^\text{C, all}$) and forward ($Y_{N_\text{jet}}^\text{F, all}$) yield as the sum of the two contributions

$$Y_{N_\text{jet}}^\text{C, all} = Y_{N_\text{jet}}^{\text{C, }t\bar{t}_\text{lep}} + Y_{N_\text{jet}}^{\text{C, }W\text{+Jets}}, \tag{7.5}$$

$$Y_{N_\text{jet}}^\text{F, all} = Y_{N_\text{jet}}^{\text{F, }t\bar{t}_\text{lep}} + Y_{N_\text{jet}}^{\text{F, }W\text{+Jets}}. \tag{7.6}$$

Using the ratio defined in Equation (7.2), the central yield of only the W+Jets sample can be expressed as a function of the forward yield and the ratio $R_{N_\text{jet}}^\text{fit}$ obtained from the extrapolation fit for each jet multiplicity N_jet as

$$Y_{N_\text{jet}}^{\text{C, }W\text{+Jets}} = \frac{R_{N_\text{jet}}^\text{fit}}{1 - R_{N_\text{jet}}^\text{fit}} \cdot Y_{N_\text{jet}}^{\text{F, }W\text{+Jets}}. \tag{7.7}$$

Assuming that the shapes of the leptonic $t\bar{t}$ N_jet as well as lepton-η distributions are known, one can define the central and forward yield for the leptonic $t\bar{t}$ sample as

$$Y_{N_\text{jet}}^{\text{C, }t\bar{t}_\text{lep}} = \sigma_{N_\text{jet}}^{t\bar{t}_\text{lep}} \cdot \mathcal{L} \cdot \varepsilon_{N_\text{jet}}^{\text{C, }t\bar{t}_\text{lep}} \cdot \varepsilon_{N_\text{jet}}^{\text{sel, }t\bar{t}_\text{lep}} \cdot \varepsilon_{N_\text{jet}}^{\text{ext, }t\bar{t}_\text{lep}}, \tag{7.8}$$

$$Y_{N_\text{jet}}^{\text{F, }t\bar{t}_\text{lep}} = \sigma_{N_\text{jet}}^{t\bar{t}_\text{lep}} \cdot \mathcal{L} \cdot \varepsilon_{N_\text{jet}}^{\text{F, }t\bar{t}_\text{lep}} \cdot \varepsilon_{N_\text{jet}}^{\text{sel, }t\bar{t}_\text{lep}} \cdot \varepsilon_{N_\text{jet}}^{\text{ext, }t\bar{t}_\text{lep}}. \tag{7.9}$$

At this stage no precise knowledge of the total cross-section is necessary to follow the method. The shape of the distribution plays a much more important role and is used here. As the forward contribution of $t\bar{t}$ in the extrapolation region is small and the theoretical description of the signal process is known to the approximate NNLO level (see Section 2.1.1), this assumed prior knowledge does not devalue the conclusiveness of the method. Using the equations above, the forward yield of the W+Jets sample can be expressed by means of the total central yield and the leptonic $t\bar{t}$ cross-section as

$$\begin{aligned} Y_{N_\text{jet}}^{\text{F, }W\text{+Jets}} &= Y_{N_\text{jet}}^\text{F, all} && - Y_{N_\text{jet}}^{\text{F, }t\bar{t}_\text{lep}} \\ &= Y_{N_\text{jet}}^\text{F, all} && - \sigma_{N_\text{jet}}^{t\bar{t}_\text{lep}} \cdot \mathcal{L} \cdot \varepsilon_{N_\text{jet}}^{\text{F, }t\bar{t}_\text{lep}} \cdot \varepsilon_{N_\text{jet}}^{\text{sel, }t\bar{t}_\text{lep}} \cdot \varepsilon_{N_\text{jet}}^{\text{ext, }t\bar{t}_\text{lep}}. \end{aligned} \tag{7.10}$$

In a similar fashion the total central yield can be derived from the equations above as

$$\begin{aligned} Y_{N_\text{jet}}^\text{C, all} &= Y_{N_\text{jet}}^{\text{C, }W\text{+Jets}} && + Y_{N_\text{jet}}^{\text{C, }t\bar{t}_\text{lep}} \\ &= \frac{R_{N_\text{jet}}^\text{fit}}{1 - R_{N_\text{jet}}^\text{fit}} \cdot Y_{N_\text{jet}}^{\text{F, }W\text{+Jets}} && + \sigma_{N_\text{jet}}^{t\bar{t}_\text{lep}} \cdot \mathcal{L} \cdot \varepsilon_{N_\text{jet}}^{\text{C, }t\bar{t}_\text{lep}} \cdot \varepsilon_{N_\text{jet}}^{\text{sel, }t\bar{t}_\text{lep}} \cdot \varepsilon_{N_\text{jet}}^{\text{ext, }t\bar{t}_\text{lep}}. \end{aligned} \tag{7.11}$$

Finally this leads to an expression similar to the simple case given in Equation (7.4), only that a correction for central and forward contributions of the leptonic $t\bar{t}$ sample are now included:

$$Y_{N_\text{jet}}^\text{C, all} - \frac{R_{N_\text{jet}}^\text{fit}}{1 - R_{N_\text{jet}}^\text{fit}} \cdot Y_{N_\text{jet}}^\text{F, all} = \sigma_{N_\text{jet}}^{t\bar{t}_\text{lep}} \cdot \mathcal{L} \cdot \varepsilon_{N_\text{jet}}^{\text{sel, }t\bar{t}_\text{lep}} \cdot \varepsilon_{N_\text{jet}}^{\text{ext, }t\bar{t}_\text{lep}} \cdot \left(\varepsilon_{N_\text{jet}}^{\text{C, }t\bar{t}_\text{lep}} - \frac{R_{N_\text{jet}}^\text{fit}}{1 - R_{N_\text{jet}}^\text{fit}} \cdot \varepsilon_{N_\text{jet}}^{\text{F, }t\bar{t}_\text{lep}} \right). \tag{7.12}$$

This can be rewritten to achieve a formula for the cross-section of the leptonic $t\bar{t}$ sample as

$$\sigma_{N_\text{jet}}^{t\bar{t}_\text{lep}} = \frac{Y_{N_\text{jet}}^\text{C, all} - \frac{R_{N_\text{jet}}^\text{fit}}{1-R_{N_\text{jet}}^\text{fit}} \cdot Y_{N_\text{jet}}^\text{F, all}}{\left(\varepsilon_{N_\text{jet}}^{\text{C, } t\bar{t}_\text{lep}} - \frac{R_{N_\text{jet}}^\text{fit}}{1-R_{N_\text{jet}}^\text{fit}} \cdot \varepsilon_{N_\text{jet}}^{\text{F, } t\bar{t}_\text{lep}}\right) \cdot \mathcal{L} \cdot \varepsilon_{N_\text{jet}}^{\text{sel, } t\bar{t}_\text{lep}} \cdot \varepsilon_{N_\text{jet}}^{\text{ext, } t\bar{t}_\text{lep}}}. \qquad (7.13)$$

Using several jet multiplicity bins and a global selection efficiency $\varepsilon^{\text{sel, } t\bar{t}_\text{lep}}$, denoting the fraction of events passing the selection requirements relative to the total number of events, one gets

$$\sigma_\text{extended}^{t\bar{t}_\text{lep}} = \frac{1}{\mathcal{L} \cdot \varepsilon^{\text{ext, } t\bar{t}_\text{lep}} \cdot \varepsilon^{\text{sel, } t\bar{t}_\text{lep}}} \cdot \sum_{N_\text{jet}} \frac{Y_{N_\text{jet}}^\text{C, all} - \frac{R_{N_\text{jet}}^\text{fit}}{1-R_{N_\text{jet}}^\text{fit}} \cdot Y_{N_\text{jet}}^\text{F, all}}{\varepsilon_{N_\text{jet}}^{\text{C, } t\bar{t}_\text{lep}} - \frac{R_{N_\text{jet}}^\text{fit}}{1-R_{N_\text{jet}}^\text{fit}} \varepsilon_{N_\text{jet}}^{\text{F, } t\bar{t}_\text{lep}}}, \qquad (7.14)$$

where $\varepsilon^{\text{ext, } t\bar{t}_\text{lep}}$ represents the fraction of selected events that fall into the jet multiplicity bins used for the cross-section calculation (sum in numerator). As introduced before $\varepsilon_{N_\text{jet}}^{\text{C, } t\bar{t}_\text{lep}}$ and $\varepsilon_{N_\text{jet}}^{\text{F, } t\bar{t}_\text{lep}}$ denote, for a given N_jet, the fraction of events falling into the central and forward region, respectively.

The cross-section obtained from the method using Equation (7.14) can then be cross-checked against the known input cross-section of the leptonic $t\bar{t}$ sample of $\sigma_{t\bar{t}_\text{lep}} = 217.1$ pb. The uncertainty on the cross-section is again estimated using an ensemble test consisting of 250 toy-MC samples, as described before. For the given centre-of-mass energy $\sqrt{s} = 10$ TeV, an integrated luminosity of $\mathcal{L} = 100$ pb^{-1} and an extraction range of $5 \leq N_\text{jet} \leq 8$ the method yields a cross-section of $\sigma_\text{extended} = 202 \pm 21$ (stat.) pb using Equation (7.14), where $\varepsilon^{\text{ext, } t\bar{t}_\text{lep}}$ and $\varepsilon^{\text{sel, } t\bar{t}_\text{lep}}$ have been estimated, using MC simulations, to be $\varepsilon^{\text{ext, } t\bar{t}_\text{lep}} = 0.348 \pm 0.006$ and $\varepsilon^{\text{sel, } t\bar{t}_\text{lep}} = 0.269 \pm 0.003$, as in the basic approach illustrated above. The total central efficiency was found to be $\varepsilon^{\text{C, } t\bar{t}_\text{lep}} = 0.591 \pm 0.006$. The value derived using the extended formula covers the expected cross-section within one statistical standard deviation. Possible sources of systematic uncertainties will be discussed and quantified in Section 7.5.

To estimate the actual number of W+Jets events in the central, forward or complete pseudo-rapidity region the cross-section $\sigma_{N_\text{jet}}^{t\bar{t}_\text{lep}}$ derived in Equation (7.13) can be entered in Equations (7.8) and (7.9). Using Equations (7.5) and (7.6) one gets the central ($Y_{N_\text{jet}}^{\text{C, } W\text{+Jets}}$) and the forward ($Y_{N_\text{jet}}^{\text{F, } W\text{+Jets}}$) yield of W+Jets events, corrected for leptonic $t\bar{t}$ contributions. Utilising the initial assumption of a flat distribution of W+Jets events as a function of pseudo-rapidity one can get the total number of W+Jets events simply by scaling the summed yield of the central and forward regions by the inverse coverage fraction of both regions. For the default setup using $|\eta^\text{lep}| \leq 1$ ($1.5 \leq |\eta^\text{lep}| \leq 2.5$) for the central (forward) region and with the assumption of a lepton acceptance flat in η, one gets a scaling factor of 5/4, as the complete pseudo-rapidity region is given by $-2.5 \leq \eta^\text{lep} \leq 2.5$.

7.3. Application in a Data-like MC Sample

The validation of the method presented above was based only on a sample given by a mixture of leptonic $t\bar{t}$ and W+Jets events. In a more data-like sample containing all major backgrounds - such as hadronic $t\bar{t}$, Z+Jets and single-top events - a slightly different approach has to be utilised. The background arising from QCD-multi-jet events is discussed separately later in this section and is neglected for now, as it is difficult to model in MC generators. While most of these backgrounds do not pass the selection criteria, it is especially the single-top events also containing a W boson and possible jets from gluon radiation that, despite the lower cross-section and mean jet multiplicity (see Figure 5.3(a)), have to be accounted for in addition to the leptonic $t\bar{t}$ events. To do so, the derivation of Equation (7.14) has to be extended to include contributions from single-top events.

Similar to Equations (7.5) and (7.6), a total yield can be defined in a data-like sample, only including an additional contribution from single-top events, passing the selection cuts, via

$$Y_{N_\mathrm{jet}}^{\mathrm{C,\ all}} = Y_{N_\mathrm{jet}}^{\mathrm{C},\ t\bar{t}_\mathrm{lep}} + Y_{N_\mathrm{jet}}^{\mathrm{C},\ t} + Y_{N_\mathrm{jet}}^{\mathrm{C},\ W\text{+Jets}}, \tag{7.15}$$

$$Y_{N_\mathrm{jet}}^{\mathrm{F,\ all}} = Y_{N_\mathrm{jet}}^{\mathrm{F},\ t\bar{t}_\mathrm{lep}} + Y_{N_\mathrm{jet}}^{\mathrm{F},\ t} + Y_{N_\mathrm{jet}}^{\mathrm{F},\ W\text{+Jets}}. \tag{7.16}$$

The estimation of the central yield of only the W+Jets sample used in Equation (7.7) holds, while Equations (7.8) and (7.9) are, as indicated above, complemented by formulas for the central and forward yield of the single-top sample, given by

$$Y_{N_\mathrm{jet}}^{\mathrm{C,\ t}} = \sigma^{t} \cdot \mathcal{L} \cdot \varepsilon_{N_\mathrm{jet}}^{\mathrm{C},\ t} \cdot \varepsilon_{N_\mathrm{jet}}^{\mathrm{sel},\ t} \cdot \varepsilon_{N_\mathrm{jet}}^{\mathrm{ext},\ t}, \tag{7.17}$$

$$Y_{N_\mathrm{jet}}^{\mathrm{F,\ t}} = \sigma^{t} \cdot \mathcal{L} \cdot \varepsilon_{N_\mathrm{jet}}^{\mathrm{F},\ t} \cdot \varepsilon_{N_\mathrm{jet}}^{\mathrm{sel},\ t} \cdot \varepsilon_{N_\mathrm{jet}}^{\mathrm{ext},\ t}. \tag{7.18}$$

The forward yield of the W+Jets sample is now given as

$$\begin{aligned} Y_{N_\mathrm{jet}}^{\mathrm{F},\ W\text{+Jets}} &= Y_{N_\mathrm{jet}}^{\mathrm{F,\ all}} && - Y_{N_\mathrm{jet}}^{\mathrm{F},\ t\bar{t}_\mathrm{lep}} - Y_{N_\mathrm{jet}}^{\mathrm{F},\ t} \\ &= Y_{N_\mathrm{jet}}^{\mathrm{F,\ all}} && - \sigma^{t\bar{t}_\mathrm{lep}} \cdot \mathcal{L} \cdot \varepsilon_{N_\mathrm{jet}}^{\mathrm{F},\ t\bar{t}_\mathrm{lep}} \cdot \varepsilon_{N_\mathrm{jet}}^{\mathrm{sel},\ t\bar{t}_\mathrm{lep}} \cdot \varepsilon_{N_\mathrm{jet}}^{\mathrm{ext},\ t\bar{t}_\mathrm{lep}} \\ & && - \sigma^{t} \cdot \mathcal{L} \cdot \varepsilon_{N_\mathrm{jet}}^{\mathrm{F},\ t} \cdot \varepsilon_{N_\mathrm{jet}}^{\mathrm{sel},\ t} \cdot \varepsilon_{N_\mathrm{jet}}^{\mathrm{ext},\ t}, \end{aligned} \tag{7.19}$$

and the total central yield can be expressed as

$$\begin{aligned} Y_{N_\mathrm{jet}}^{\mathrm{C,\ all}} &= Y_{N_\mathrm{jet}}^{\mathrm{C},\ W\text{+Jets}} && + Y_{N_\mathrm{jet}}^{\mathrm{C},\ t\bar{t}_\mathrm{lep}} + Y_{N_\mathrm{jet}}^{\mathrm{C},\ t} \\ &= \frac{R_{N_\mathrm{jet}}^{\mathrm{fit}}}{1 - R_{N_\mathrm{jet}}^{\mathrm{fit}}} \cdot Y_{N_\mathrm{jet}}^{\mathrm{F},\ W\text{+Jets}} && + \sigma^{t\bar{t}_\mathrm{lep}} \cdot \mathcal{L} \cdot \varepsilon_{N_\mathrm{jet}}^{\mathrm{C},\ t\bar{t}_\mathrm{lep}} \cdot \varepsilon_{N_\mathrm{jet}}^{\mathrm{sel},\ t\bar{t}_\mathrm{lep}} \cdot \varepsilon_{N_\mathrm{jet}}^{\mathrm{ext},\ t\bar{t}_\mathrm{lep}} \\ & && + \sigma^{t} \cdot \mathcal{L} \cdot \varepsilon_{N_\mathrm{jet}}^{\mathrm{C},\ t} \cdot \varepsilon_{N_\mathrm{jet}}^{\mathrm{sel},\ t} \cdot \varepsilon_{N_\mathrm{jet}}^{\mathrm{ext},\ t}. \end{aligned} \tag{7.20}$$

Unfortunately, due to the different efficiencies for leptonic $t\bar{t}$ and single-top no analytic representation of the sum of both cross-sections can be derived from these formulas. To still allow for a cross check of the method, a formula stating the method prediction on one side and the efficiency corrected expected cross-sections on the other side can be checked

Table 7.1.: Z-values obtained using Equation (7.22) with the default pseudo-rapidity regions for jet multiplicities of $5 \leq N_{\text{jet}} \leq 8$. Uncertainties are statistical only.

N_{jet}	5	6	7	8
Z [pb]	–14±64	17±35	22±19	6±10

for consistency as

$$\begin{aligned}\frac{Y^{\text{C, all}}_{N_{\text{jet}}} - \frac{R^{\text{fit}}_{N_{\text{jet}}}}{1-R^{\text{fit}}_{N_{\text{jet}}}} \cdot Y^{\text{F, all}}_{N_{\text{jet}}}}{\mathcal{L}} &= \sigma^{t\bar{t}_{\text{lep}}} \cdot \varepsilon^{\text{ext, }t\bar{t}_{\text{lep}}} \cdot \varepsilon^{\text{sel, }t\bar{t}_{\text{lep}}} \cdot \left(\varepsilon^{\text{C, }t\bar{t}_{\text{lep}}}_{N_{\text{jet}}} - \frac{R^{\text{fit}}_{N_{\text{jet}}}}{1 - R^{\text{fit}}_{N_{\text{jet}}}} \varepsilon^{\text{F, }t\bar{t}_{\text{lep}}}_{N_{\text{jet}}} \right) \\ &+ \sigma^{t} \cdot \varepsilon^{\text{ext, }t} \cdot \varepsilon^{\text{sel, }t} \cdot \left(\varepsilon^{\text{C, }t}_{N_{\text{jet}}} - \frac{R^{\text{fit}}_{N_{\text{jet}}}}{1 - R^{\text{fit}}_{N_{\text{jet}}}} \varepsilon^{\text{F, }t}_{N_{\text{jet}}} \right) \end{aligned} \tag{7.21}$$

Defining the left-hand side of the equation as F^M and the leptonic $t\bar{t}$ and single-top related terms as $F^{t\bar{t}}$ and F^t, respectively, one can check a quantity

$$Z_{N_{\text{jet}}} = F^M_{N_{\text{jet}}} - F^{t\bar{t}}_{N_{\text{jet}}} - F^t_{N_{\text{jet}}} \stackrel{?}{=} 0 \text{ pb} \tag{7.22}$$

for consistency with zero. This equality should be given in all bins of the jet multiplicity used for later signal extraction. The results obtained using Equation (7.22) with the default pseudo-rapidity regions for jet multiplicities of $5 \leq N_{\text{jet}} \leq 8$ and the input cross-sections $\sigma_{\text{t}} = 57.4$ pb and $\sigma_{t\bar{t}_{\text{lep}}} = 217.1$ pb are summarised in Table 7.1. All results are in agreement with the expected value of zero within the statistical uncertainty.

Assuming some prior knowledge on the single-top cross-section together with rearranging Equation (7.21) to get an estimate of the leptonic $t\bar{t}$ cross-section $\sigma^{t\bar{t}_{\text{lep}}}$, the actual number of W+Jets events in the central, forward or complete pseudo-rapidity region can be estimated in a similar approach as described in the previous section.

7.4. Discussion of Possible Modifications

The default setup of the method can be modified in several parameters. These adaptations are discussed in the following. Systematic uncertainties present in all adaptations of the method are summarised in the following section, while here only the effect on the final result of each modification will be discussed and quantified.

Extrapolation Fit Function As a default, the extrapolation function applied to the ratio $R_{N_{\text{jet}}}$ as a function of jet multiplicity N_{jet} is given by a first order polynomial $(a+bx)$. Even though the ratio is expected to be constant for the W+Jets background over a wide range of jet multiplicities, this allows for a better description of a constant decrease of $R_{N_{\text{jet}}}$ with increasing N_{jet} as depicted in Figure 7.3(a). In a different approach, a constant function could be used, enforcing the assumed behaviour. Using a constant function has been found to cause a sizeable underestimation of the cross-

Table 7.2.: σ_{extended} and Z values derived for various m_T^W-window sizes. Uncertainties are statistical only.

Δm_T^W [GeV]	±10	±15	±20	**±25**	±30	±35	∞
σ_{extended} [pb]	206±35	205±26	201±20	202±21	199±18	199±18	199±16
Z at $N_{\text{jet}} = 5$ [pb]	–15±41	–15±52	–19±61	–14±64	–12±66	–21±65	–30±78
Z at $N_{\text{jet}} = 6$ [pb]	17±24	23±29	19±33	17±35	23±40	19±37	26±48
Z at $N_{\text{jet}} = 7$ [pb]	15±12	16±15	20±18	22±19	20±19	24±22	33±26
Z at $N_{\text{jet}} = 8$ [pb]	3±7	5±9	6±9	6±10	6±10	7±11	8±14

section by more than 40%, hence has been omitted in the following.

Extrapolation Fit Range In addition to changing the function used for the extrapolation, also the default range of $1 \leq N_{\text{jet}} \leq 2$ can be modified. It has been found that including the $N_{\text{jet}} = 0$ bin and fitting a first order polynomial results in sizeable deviations of the predicted yield, due to a not fully understood reduced ratio $R_{N_{\text{jet}}}$ in this bin visible in Figures 7.3(a) and 7.4(a). Though the previously discussed constant function extrapolation improves using the $N_{\text{jet}} = 0$ bin, the first bin has been excluded from the extrapolation for the above stated reasons. Also the inclusion of the $N_{\text{jet}} = 3$ bin would be of advantage in terms of a possible fit to all three points, though it was abstained from doing so, due to the already quite large signal contribution at this multiplicity (see Figure 7.5(a)).

W Boson Transverse Mass Independent of changes to the parameters of the method itself, such as described above, the prior selection of events used in the method could be subject to modifications. One distinct feature in the event selection is the requirement on the reconstructed transverse mass of the leptonic W boson. Mainly to suppress backgrounds arising from QCD-multi-jet events, this requirement also has influence on the available event numbers and might influence the η distribution of the lepton as well as the jet multiplicity distribution. It has been found that the ratio $R_{N_{\text{jet}}}$ remains flat at jet multiplicities of $0 \leq N_{\text{jet}} \leq 8$ as a function of the m_T^W-window size as long as a minimum window size Δm_T^W of ±20 to ±25 GeV is ensured. Smaller window sizes noticeably affect the available event numbers especially at high jet multiplicities for W+Jets events. The final motivation to choose a default value of ±25 GeV arose from a trade-off between both statements. To quantify changes in the result, the window size has been varied (see Table 7.2) between ±10 and ±35 GeV or was omitted completely. The resulting estimations are consistent amongst each other and with the expected value within less than two standard deviations.

Lepton Transverse Momentum The requirements imposed on reconstructed leptons, introduced in Chapter 5, are based on the standard definitions applied in the ATLAS top quark group [43]. To quantify the influence of a change in the transverse momentum (p_{T}) threshold from its default of 20 GeV, thresholds of 10 and 30 GeV have been analysed yielding consistent results (see Table 7.3) also compatible with the expected value within less than two standard deviations.

Table 7.3.: σ_{extended} and Z values derived for various lepton-p_{T} thresholds. Uncertainties are statistical only.

$p_{\mathrm{T}}^{\text{lep, min}}$ [GeV]	10	**20**	30
σ_{extended} [pb]	198±21	202±21	207±21
Z at $N_{\text{jet}} = 5$ [pb]	–36±66	–14±64	–7±52
Z at $N_{\text{jet}} = 6$ [pb]	8±37	17±35	19±30
Z at $N_{\text{jet}} = 7$ [pb]	20±20	22±19	21±15
Z at $N_{\text{jet}} = 8$ [pb]	5±11	6±10	6±10

Table 7.4.: σ_{extended} and Z values derived for various $E_{\mathrm{T}}^{\text{miss}}$ thresholds. Uncertainties are statistical only.

$E_{\mathrm{T}}^{\text{miss}}$ [GeV]	**none**	10	20	30	40
σ_{extended} [pb]	202±21	202±21	204±19	205±21	196±24
Z at $N_{\text{jet}} = 5$ [pb]	–14±64	–16±64	–8±59	–11±52	–16±52
Z at $N_{\text{jet}} = 6$ [pb]	17±35	14±36	18±34	21±31	12±31
Z at $N_{\text{jet}} = 7$ [pb]	22±19	21±19	21±18	18±19	9±16
Z at $N_{\text{jet}} = 8$ [pb]	6±10	6±10	7±11	6±9	4±9

Missing Energy Another possible criterion in the selection is a cut on the missing transverse energy in the event, which might offer additional suppression of e.g. QCD-multi-jet or especially Z+Jets events. Due to the level of detector understanding (e.g. jet energy fluctuations, noise and inefficiency regions) necessary to fully understand this quantity, a direct transverse missing energy ($E_{\mathrm{T}}^{\text{miss}}$) requirement has been neglected in the default event selection. Nevertheless, an indirect requirement remains via the m_T^W-window cut. To evaluate a possible influence of an $E_{\mathrm{T}}^{\text{miss}}$ cut in the selection, various thresholds have been implemented. The selected values are distributed around the default $E_{\mathrm{T}}^{\text{miss}}$-cut value used in the ATLAS top quark group of 20 GeV and yield results (see Table 7.4) consistent with the expected values within less than two standard deviations.

7.5. Systematic Uncertainties

As part of the validation of the method, various sources of uncertainties, arising from the method itself, from measurements of observables in the detector and from the MC input, have been studied and will be discussed in this section.

Cross-section Extraction Range The calculation of the leptonic $t\bar{t}$ cross-section is based on a range of jet multiplicity bins. Though the calculation should yield the same value for each bin in itself, these results and especially the corresponding uncertainties are subject to large variations due to the different statistics available in each bin. By deriving the value in question using several jet multiplicity bins the effect of

Table 7.5.: σ_{extended} and Z values derived for various N_{jet} ranges. Uncertainties are statistical only.

N_{jet} Range	4-7	4-8	5-6	5-7	**5-8**	6-7	6-8
σ_{extended} [pb]	186±20	187±20	199±22	201±20	202±21	200±29	201±29

statistical fluctuations can be minimised. Still the results obtained by using different ranges should agree within their uncertainties. Various setups within the range of $4 \leq N_{\text{jet}} \leq 8$ have been studied.

Only the inclusion of the $N_{\text{jet}} = 4$ bin, containing the highest fraction of leptonic $t\bar{t}$ events, leads to a deviation from the expected result of about twice the statistical uncertainty. The deviation is most likely caused by the fact that due to a large $t\bar{t}$ contribution in that N_{jet} bin also the fraction of events in the background dominated region, used for the extrapolation, is quite high and reaches a point that cannot be accounted for with the present extended method, assuming only small signal contributions in the background dominated regions. All other ranges (see Table 7.5) yield results consistent within their uncertainties amongst each other and with the expected cross-section. Omitting the $N_{\text{jet}} = 4$ bin a systematic uncertainty on the extracted cross-section of about $^{+0}_{-3}$ pb is assumed based on the given results.

Central-Forward Definition The definition of central and forward regions of the lepton pseudo-rapidity is both driven by topological as well as detector geometry constraints. The topological part is represented by one of the main assumptions of the method, that the $t\bar{t}$ signal is dominant at low rapidity, and therefore limits the upper bound of the central region to an area of phase space where this statement still holds. At the same time it restricts the lower bound of the forward region, to an area where the background (W+Jets) dominates. The choice of omitting the η-range between the central and forward region is motivated both on account of excluding areas in which none of the above stated assumptions hold and by geometrical reasons. The latter one comprise regions of inefficiency, due to the transition between the barrel and end-cap detector parts, as well as the acceptance boundary of the tracking detectors at $|\eta| = 2.5$. Still the effect of variations in these bounds have been studied by changing the default values of the upper bound of the central region $|\eta| \leq 1.0$ and the lower bound of the forward region $|\eta| \geq 1.5$ separately up and down by 0.2 in steps of 0.1 in units of η. Essentially all considered configurations (see Table 7.6) yield identical and therefore consistent results. Only the inclusion of the previously described transition region between barrel and end-cap in either the central or the forward region will cause a slight increase in the statistical uncertainty due to reconstruction and trigger inefficiencies in this region. An uncertainty on the extracted cross-section of less than $^{+2}_{-5}$ pb can is hereby estimated due to this effect.

Jet Energy Scale Uncertainties in the Jet Energy Scale (JES) are reflected directly and indirectly in several observables utilised in this method. Variations in the measured transverse energy E_{T} of jets have direct impact on the jet multiplicity distribution and a possible cut on $E_{\text{T}}^{\text{miss}}$, as discussed above. It is through the $E_{\text{T}}^{\text{miss}}$, used in

Table 7.6.: σ_{extended} and Z values for various definitions of the central ($|\eta^{\text{lep}}| \leq \eta^{\text{C}}_{\text{max}}$) and forward ($\eta^{\text{F}}_{\text{min}} \leq |\eta^{\text{lep}}| \leq 2.5$) region. Uncertainties are statistical only.

$\eta^{\text{C}}_{\text{max}}$ $\eta^{\text{F}}_{\text{min}}$	0.9 1.5	1.0 1.3	1.0 1.4	**1.0** **1.5**	1.0 1.6	1.0 1.7	1.1 1.5	1.3 1.6
σ_{extended} [pb]	202±20	197±22	201±21	202±21	202±19	201±18	204±22	201±19
Z at $N_{\text{jet}} = 5$ [pb]	−11±57	−20±61	−15±64	−14±64	−14±62	−17±61	−13±73	−22±72
Z at $N_{\text{jet}} = 6$ [pb]	16±31	11±37	15±33	17±35	20±36	19±38	18±36	20±43
Z at $N_{\text{jet}} = 7$ [pb]	18±18	19±20	22±20	22±19	24±20	24±19	23±20	25±20
Z at $N_{\text{jet}} = 8$ [pb]	6±9	6±10	6±10	6±10	6±10	6±11	7±11	8±12

the calculation of the transverse mass of the leptonic W boson, that uncertainties in JES indirectly affect the event selection. The effect of changing the JES for all jets on both the absolute value and the direction of $E_{\text{T}}^{\text{miss}}$ is depicted in Figure 7.6. To estimate the effect of fluctuations in JES on the method presented, samples with a ±5% variation of the JES have been investigated and the results (see Table 7.7) have been compared to the default reconstruction. Hereby 5% represents a conservative approximation of the expected JES uncertainty after having recorded about 100 pb^{-1} of data. An uncertainty on the extracted cross-section of $^{+0}_{-1}$ pb is estimated due to the influence of wrongly adjusted JES.

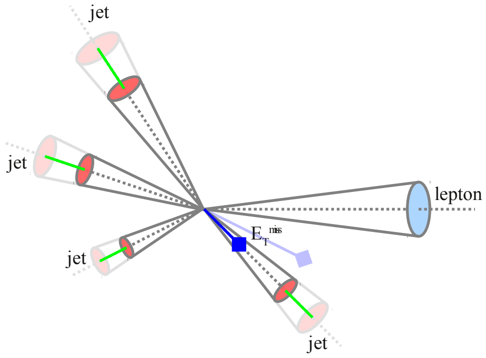

Figure 7.6.: Illustration of the effect, of reducing the JES, on $E_{\text{T}}^{\text{miss}}$. In this exaggerated example the JES is reduced by 25% (opaque objects) compared to the default scale (transparent objects). $E_{\text{T}}^{\text{miss}}$ is recalculated using the old $E_{\text{T}}^{\text{miss}}$ vector and the vectorial information on the jet energy differences of each jet (green solid lines). The different colours (red, blue, purple) indicate different object types (leptons, jets, $E_{\text{T}}^{\text{miss}}$).

PDF Variations As variations on JES, also variations in the parton distribution functions (PDFs) have a direct influence on the event topology and therefore the jet multiplicity distribution. To estimate an uncertainty arising from the PDFs, samples have been re-weighted, using the technique introduced in Section 4.4.1. As a first order approach, a PDF error set (CTEQ6ME), containing ±1σ changes in each parameter, of the same PDF set used for the production of the $t\bar{t}$ sample (CTEQ6M) has been used and the method was repeated for each configuration. To also reflect a possible

Table 7.7.: σ_{extended} and Z values derived for corrected JES. Uncertainties are statistical only.

JES	-5%	**nominal**	+5%
σ_{extended} [pb]	201±19	202±21	202±20
Z at $N_{\text{jet}} = 5$ [pb]	–19±59	–14±64	–15±62
Z at $N_{\text{jet}} = 6$ [pb]	15±35	17±35	18±35
Z at $N_{\text{jet}} = 7$ [pb]	21±19	22±19	22±19
Z at $N_{\text{jet}} = 8$ [pb]	7±10	6±10	6±10

Table 7.8.: Mean and RMS of σ_{extended} and Z values derived for $\pm 1\sigma$ modifications of all parameters within each of two PDF error sets (CTEQ6ME and MRST2001E).

PDF set	CTEQ6ME	MRST2001E
$\langle\sigma_{\text{extended}}\rangle$ [pb]	203±20	198±15
$\langle Z\rangle$ at $N_{\text{jet}} = 5$ [pb]	–20±50	–53±45
$\langle Z\rangle$ at $N_{\text{jet}} = 6$ [pb]	7±32	15±30
$\langle Z\rangle$ at $N_{\text{jet}} = 7$ [pb]	22±13	27±12
$\langle Z\rangle$ at $N_{\text{jet}} = 8$ [pb]	10±7	6±7

influence due to using a different PDF set, the procedure has been done also for a second PDF error set (MRST2001E). Since both PDF sets are NLO sets, applying the stated re-weighting technique to events generated using LO precision PDF sets, such as the W+Jets samples, the results have to be taken with a pinch of salt and can only serve as a guidance. A conservative uncertainty on the extracted cross-section of ±20 pb is assumed from the results (see Table 7.8) obtained using both PDF (sub)sets and the Hessian method [111] with

$$\Delta X = \frac{1}{2}\sqrt{\sum_i \left[X(a_i^+) - X(a_i^-)\right]}, \tag{7.23}$$

where $a_i^\pm$ are the parameters (eigenvectors) of the PDF set, varied by $\pm 1\sigma$. It has to be noted that the number of toy-MC samples produced for each configuration has been decreased to ten instead of 250 to minimise the computational complexity of this analysis, anyway dominated by the effect caused by variations in the PDF parameters.

QCD-multi-jet Background Due to the indirect cut on $E_{\text{T}}^{\text{miss}}$, given by the m_T^W-window in the event selection, only a small fraction of QCD-multi-jet events remains in the final analysis sample. As the available number of MC events represent only a marginal fraction of the expected event numbers at the centre-of-mass energy and integrated luminosity assumed in this analysis, the few selected events are heavily weighted and therefore blur the predictability of the method and have been neglected in this thesis. With the availability of the corresponding event numbers in real data, this issue can and should be addressed without the weight problem.

A possible method to estimate the QCD-multi-jet background could utilise the above mentioned direct $E_{\mathrm{T}}^{\mathrm{miss}}$ selection cut and use the low (below the cut) $E_{\mathrm{T}}^{\mathrm{miss}}$ region as a control region to establish a QCD enriched sample from data and extrapolate, if necessary including corrections, to the high $E_{\mathrm{T}}^{\mathrm{miss}}$ region used for the W+Jets background analysis. With an approximation of the QCD event numbers in hand, the W+Jets background estimation can be performed by subtracting the according yield in the central and forward regions.

MC Generators To investigate the uncertainty due to the theoretical description and the modelling of both the hard process and the subsequent parton showering it would be of advantage to repeat the study using various available MC generators, such as SHERPA [112], for the production of the W+Jets sample. Unfortunately at the time of writing this thesis only the ALPGEN samples utilised in this study have been available as fully simulated MC events. While samples using other MC generators could be produced using Fast Simulation tools, this approach was omitted due to the additional uncertainty arising from the comparison of fully to fast simulated samples.

To derive a global systematic uncertainty it is necessary to assess possible correlations between the influencing parameters. The theoretical systematic uncertainty arising from the PDFs can be considered uncorrelated with any of the others. For the remaining uncertainties stemming from the finite precision in the determination of the Jet Energy Scale and from the definition of central and forward regions as well as extraction range, samples of variations in one of the variables versus modifications in the other were checked and no significant correlation was observed. Based on this the total systematic uncertainty is calculated as the square root of the squared individual uncertainties stated in Table 7.9. Adding the obtained systematic uncertainty to the previously stated approximated cross-section derived for the mixture of leptonic $t\bar{t}$ and W+Jets events using the extended method one gets $\sigma_{\mathrm{extended}} = 202 \pm 21\ (\mathrm{stat.})^{+20}_{-21}\ (\mathrm{syst.})$ pb. It can be seen that amongst the investigated sources of uncertainties, the PDF variations are clearly dominating, though the resulting uncertainty on the estimated cross-section of the leptonic $t\bar{t}$ sample of about 10% is not unexpected and has been found to be of similar size in the W charge asymmetry and W/Z ratio methods to estimate the W+Jets background.

7.6. Linearity of the Result

The linearity of the estimated cross-section relative to changes of the input cross-section of the leptonic $t\bar{t}$ sample is both a cross-check and allows, if fulfilled, to correct for small biases due to an imprecise known input cross-section especially in first data scenarios. To test for the linearity of the result the above mentioned mixture of leptonic $t\bar{t}$ and W+Jets events was reproduced scaling the cross-section (re-weighting the events) of the leptonic $t\bar{t}$ sample with factors from 0.5 to 1.5. Figure 7.7 shows the extracted cross-section for eleven mixtures fitted with a linear function. As can be seen the results are well described by the linear function (fit parameters are given in the plot).

Table 7.9.: Summary of systematic uncertainties on the leptonic $t\bar{t}$ cross-section $\sigma_{\text{extended}}^{t\bar{t}_{\text{lep}}}$ derived for the mixture of leptonic $t\bar{t}$ and W+Jets events using the extended method.

Source	Estimate
Cross-section Extraction Range	$^{+0}_{-3}$ pb
Central-Forward Definition	$^{+2}_{-5}$ pb
Jet Energy Scale	$^{+0}_{-1}$ pb
PDF Variations	±20 pb
QCD-multi-jet Background	–
MC Generators	–
Total	$^{+20}_{-21}$ pb

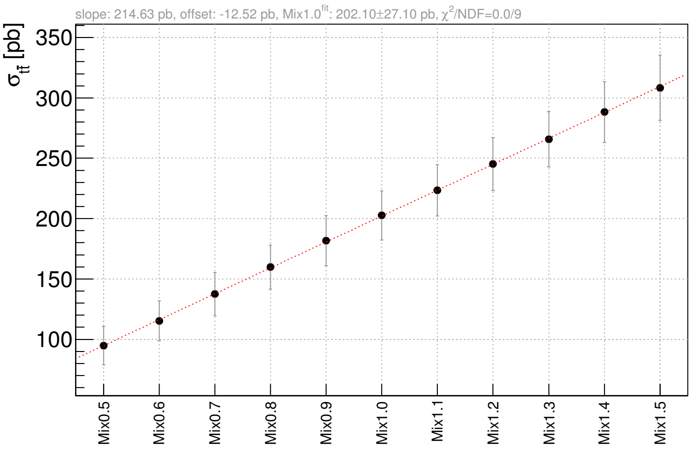

Figure 7.7.: Extracted cross-section for eleven mixtures of leptonic $t\bar{t}$ and W+Jets events fitted with a linear function. The cross-section scaling factor of the leptonic $t\bar{t}$ sample is given in the names on the abscissa.

Table 7.10.: Estimated and expected cross-sections (calculated for the mixture of leptonic $t\bar{t}$ and W+Jets events) and Z values (for the data-like mixture) for various combinations of assumed centre-of-mass energy and integrated luminosity. The estimated cross-section σ_{extended} was derived using the extended method with an N_{jet} extraction range as stated. Uncertainties are statistical only.

$\sqrt{s}$ [TeV]	**10**	10	7	7	7	7
$\mathcal{L}$ [pb^{-1}]	**100**	10	100	50	20	10
N_{jet} Range	5-8	5-7	5-7	5-6	5-6	5
σ_{extended} [pb]	202±21	225±83	79±12	75±18	81±31	81±52
$\sigma^{t\bar{t}_{\text{lep}}}$ [pb]	217.1	217.1	86.8	86.8	86.8	86.8
Z at $N_{\text{jet}} = 5$ [pb]	–14±64	–2±20	–1±41	–1±31	–2±18	–2±13
Z at $N_{\text{jet}} = 6$ [pb]	17±35	1±11	6±22	0±18	0±10	
Z at $N_{\text{jet}} = 7$ [pb]	22±19	2±6	12±12			
Z at $N_{\text{jet}} = 8$ [pb]	6±10					

7.7. Feasibility with Early Data

With the restart of the LHC this year, it is of topical interest to investigate the feasibility of a new method with early data. Hereby the term early data denotes the fact of limited available statistics of $O(10)$ pb^{-1} and a centre-of-mass energy of 7 TeV compared to the 14 TeV in the design of the LHC. Both the decrease in integrated luminosity and in centre-of-mass energy result in a reduction of the sample statistics. This affects backgrounds as well as signal processes, though the relative change is different between various processes as depicted in Figure 2.3. Since the MC samples introduced in Section 4.5 were produced assuming a centre-of-mass energy of 10 TeV, a re-weighting technique, as introduced in Section 4.4.2, was used to estimate the results at 7 TeV. As discussed before, such a re-weighting technique can only serve as a rough estimation. Various combinations of assumed centre-of-mass energy and integrated luminosity were tested and the results of the validation are shown in Table 7.10. It has to be noted that due to the limited number of events especially in the higher jet multiplicity bins, the result for $\mathcal{L} = 10$ pb^{-1} at $\sqrt{s} = 10$ TeV and those at $\sqrt{s} = 7$ TeV were derived using a reduced extraction range, as stated in the table, resulting in an increase of the statistical uncertainty. Due to both, the decreased extraction range and general decrease in available statistics, the statistical uncertainty rises significantly. It can be seen that with the event numbers expected from first data the validation of the method loses its conclusiveness. An integrated luminosity of the order 50 pb^{-1} or more seems to be necessary at $\sqrt{s} = 7$ TeV for this method to provide reasonably safe results, assuming an error below 50% percent of the actual value.

7.8. Application to Top-Antitop Cross-Section Measurement

Finally the method can be used to estimate the number of W+Jets events in the signal region used for measurements of the $t\bar{t}$ cross-section in the semi-leptonic decay channel.

Table 7.11.: Number of W+Jets events passing the selection as know from the MC input and estimated using the mentioned procedure for jet multiplicities ranging from 5 to 8, in a sample mixture of leptonic $t\bar{t}$ and W+Jets events only (I) and the data-like (excluding QCD events) mixture (II). Uncertainties are both statistical (first) and systematic (second).

	N_{jet}	5		6		7		8	
		MC	estimated	MC	estimated	MC	estimated	MC	estimated
I	$Y^{\text{C},\,W\text{+Jets}}_{N_{\text{jet}}}$	403	460±63±65	92	130±37±26	23	22±20±8	4	4±16±2
	$Y^{\text{F},\,W\text{+Jets}}_{N_{\text{jet}}}$	397	412±51±21	104	117±31±8	20	20±18±2	4	3±16±1
	$Y^{\text{T},\,W\text{+Jets}}_{N_{\text{jet}}}$	986	1089±141±68	243	309±86±27	54	52±48±8	11	8±40±2
II	$Y^{\text{C},\,W\text{+Jets}}_{N_{\text{jet}}}$	403	508±66±65	92	139±34±26	23	25±19±8	4	4±12±2
	$Y^{\text{F},\,W\text{+Jets}}_{N_{\text{jet}}}$	397	463±54±21	104	127±30±8	20	23±17±2	4	4±12±1
	$Y^{\text{T},\,W\text{+Jets}}_{N_{\text{jet}}}$	986	1214±148±68	243	333±79±27	54	60±45±8	11	10±30±2

The calculation is detailed in Section 7.2 for the simplified case of the mixture of only leptonic $t\bar{t}$ and W+Jets events. Table 7.11 (I) gives an overview on the number of W+Jets events passing the selection taken from the MC input and estimated using the mentioned procedure for jet multiplicities ranging from 5 to 8, in a sample mixture of leptonic $t\bar{t}$ and W+Jets events only. It can be seen that the estimated number of background events agrees well with the expected yield derived from the known input contribution of W+Jets events. The systematic uncertainty is propagated from the systematic uncertainty on the estimated cross-section. The total uncertainty is about 15% for $N_{\text{jet}} = 5$ bin and increases with increasing jet multiplicity as the available statistics drops. In real data, as discussed above, some more prior knowledge such as an estimate of the single-top cross-section and shapes is needed. Due to much better predictions on the single-top cross-section compared to that of W+Jets especially for higher multiplicities this does not pose a major drawback. Using a similar approach as for the mixture of leptonic $t\bar{t}$ and W+Jets events the number of W+Jets events, as stated in Table 7.11 (II), can be estimated. Hereby changing the input cross-section for single-top by ±20% has an impact of less than 3% on the total number of estimated W+Jets events. Considering the total approximated uncertainty of the predictions the deviation is below two standard deviations and amounts to about 25% of the expected number of W+Jets events for most of the top dominated region. This can be compared to alternative methods, taking advantage of the production asymmetry between W^+ and W^- bosons or the ratio between W and Z bosons as a function of the number of associated jets, as introduced above. With total uncertainties of below 40% and 35%, respectively, already with about 50 pb^{-1} of integrated luminosity at $\sqrt{s} = 7$ TeV, the approach introduced in this thesis, along with the presented extension, could serve as an orthogonal procedure to estimate the W+Jets background in ATLAS. All data-driven approaches, including the one presented above, are essential to get a handle on the absolute normalisation of the W+Jets background, which has a theoretical uncertainty of up to 50% for higher jet multiplicities, as mentioned above.

Chapter 8.

Summary and Conclusion

In this thesis, data-driven techniques to estimate the multi-jet trigger efficiency and the W+Jets background in top pair events have been introduced to the ATLAS experiment.

The first analysis covered the characterisation and optimisation of jet triggers and introduced an alternative method, based on a *tag-and-probe* approach, to estimate the trigger efficiency of multi-jet trigger objects in semi-leptonic $t\bar{t}$ events. The characterisation and optimisation of jet triggers has been published as part of an ATLAS physics paper [43] using an older software environment, while the results have been reproduced and confirmed with a current software release for the purpose of the writing of this thesis. The *tag-and-probe* method proved to be a suitable way to estimate multi-jet trigger object efficiencies without introducing any significant bias. Beyond the scope of this thesis the derived efficiencies could be applied to other event topologies unfolding the event selection efficiency for the utilised semi-leptonic $t\bar{t}$ topology.

In the second analysis, a data-driven approach to estimate the background contribution arising from W+Jets events has been investigated and introduced to ATLAS. By defining signal and background dominated regions by means of the jet multiplicity and the pseudo-rapidity distribution of the lepton in the event, the W+Jets contribution is extrapolated from the background dominated into the signal dominated region. Taking into account a possible signal contribution in the extrapolation region, an extension of the method has been developed and evaluated. By avoiding any prior knowledge on the absolute and relative cross-section of W+Jets events obtained from unreliable predictions of LO MC generators, this data-driven approach contents itself with signal shapes of top quark events. Using 100 pb^{-1} of fully simulated data at $\sqrt{s} = 10$ TeV it has been shown that with basic assumptions the yield of W+Jets events in signal dominated regions in jet multiplicity and lepton pseudo-rapidity can be estimated within uncertainties to a level of about 25% for most of the top dominated region. It was found that a minimum integrated luminosity exceeding the expectation for the first year of LHC physics is required to achieve this level of agreement. Still this approach could serve as an additional procedure to available methods taking advantage of the production asymmetry between W^+ and W^- bosons or the ratio between W and Z bosons as a function of the number of associated jets, though these methods are expected to yield total uncertainties of below 40% and 35%, respectively, already with about 50 pb^{-1} of integrated luminosity at $\sqrt{s} = 7$ TeV.

To allow for a more precise estimate on the feasibility of the method with early data, the analyses need to be repeated with the recently available fully simulated $\sqrt{s} = 7$ TeV MC samples, thereby also avoiding additional uncertainties due to the re-weighting procedure.

In addition a more detailed study utilising MC samples produced with various available MC generators could give important insights into e.g. the η-dependence of the W+Jets background or the response of the method especially on variations in the N_{jet} spectrum of the W+Jets background.

Independent of these data-driven analyses, a study covering the characterisation of the thermal performance of the Pixel Detector of ATLAS has been presented. Despite a few imperfections, the system has been found, and is expected, to operate perfectly within its given design specification even after several years of irradiation. The survey covered both the detector itself as well as the off-detector elements connected to the Pixel Detector. The presented analyses constitute a major fraction of an ATLAS note [113] in preparation and will be part of a general ATLAS Pixel Detector paper [78].

Appendices

Appendix A.

Thermal Performance of the ATLAS Pixel Detector

The ATLAS Pixel Detector, described in Section 3.2.4, is the device closest to the interaction point. It will have to sustain a radiation dose of up to 10^{15} MeV neutron equivalent fluence per square centimetre (10^{15} F_{neq} cm^{-2}) throughout its lifetime. To minimise the damage due to irradiation of the sensors and thereby limit the consequential leakage current, the modules have to be cooled down to temperatures below 0°C ideally without interruption. To ensure this, the Pixel Detector is build using two types of cooling systems: an evaporative cooling system for the detector components within the ID volume and a mono-phase cooling system for cables and patch-panels outside the ID volume, as described in Section 3.2.4.

In this chapter studies, performed during the Pixel Detector commissioning phase in 2008 and early 2009, are presented that help understanding and ensuring the running of the detector itself as well as its connected services such as the cooling system. A note covering all these analyses is in preparation [113]. While two analyses are based on measurements from specific occurrences a third analysis uses input from various measurements throughout the whole commissioning phase. Studies concerning the beam-pipe bake-out performed in July 2008 and the low back-pressure test realised in December 2008, are motivated and summarised in Section A.2 and Section A.3, respectively. More general investigations on the operational performance of the Pixel Detector are presented in Section A.4.

The studies presented below are to a large extend based on software developed within the scope of the thesis, that for the first time allowed to easily combine and compare various measurements of the ATLAS Detector Control System (DCS) [82] at a given point in time. This development is introduced in Section A.1

A.1. DCS Software

All detector status information, including for example temperatures measured on each module and currents of the optoboard PIN diode[1], continuously monitored by the DCS are stored in databases. To minimise the bandwidth of the DCS data transfer and the amount of unnecessary repeated information, the DCS exploits a data reduction technique for storing information in the databases, based on two simple rules: data, such as a

---

[1] PIN diode = Positive-Intrinsic-Negative diode, to detect the optical signals coming from the off-detector elements.

measured current, is only written to the database in case (a) the measured value changed by a previously defined percentage over a given number of measurements or time; or (b) after a certain, also to be defined, time interval. The percentage values as well as the length of the time intervals are defined and optimised for each measured quantity, so-called data point element (DPE). This entails the fact that not all information from all DCS channels is written to the database at the same time.

The rationale of the software is to obtain the last measured, and therefore at the time of interest valid, values of all quantities in question and label them with a common time-stamp. In addition it automatically calculates and stores the arithmetic mean of all measurements of a single quantity in a given interval in time together with the root mean square (RMS) and the centre of the time interval as a common time-stamp. In the standard setup, all temperatures, currents and voltages measured at each module and PP0 are stored along with the common time-stamp as well as the object location within the Pixel Detector and the connected cooling loop. This basic selection can be easily extended by any other DPE using regular expressions on the element alias in the database. The information are then stored as an object oriented tree structure into an open file format utilising the ROOT data analysis framework [114]. Hereby various analyses, including arithmetic operations and comparisons between different DPEs, can be carried out without accessing the central databases each and every time.

The software, including most of the analysis code utilised for the studies presented in this chapter, is documented in [115] and accessible via a concurrent versions system at CERN [116].

A.2. Beam-pipe Bake-out

One of the main sources of background noise to the experiments at the LHC is given by beam-gas interactions along the experimental insertion regions. Due to that the vacuum control is a crucial point in the operation of experiments such as ATLAS. While in most of the cold beam-pipe regions the so-called cold bore beam pipe acts as an efficient cryopump collecting almost all residual contamination [117], resulting in a vacuum of better than 10^{-11}, the interaction region in ATLAS features only six ion pumps, resulting in a relatively poor pumping impedance. To compensate this deficit, a TiZrV NEG (Non Evaporable Getter) coating is applied to the beam-pipe in most of the interaction region (more than 90% coverage in ATLAS). After an initial activation that requires temperatures of above 200°C, the NEG will provide a very high pumping rate. To develop the full effect the system must be cleaned before activating the NEG. To meet this twofold procedure, the beam-pipe bake-out is performed in two steps. In a first step, the non-NEG coated components are heated in a high temperature bake-out (250 - 350°C), to de-gas impurities from their surfaces. In the second step, the NEG regions are activated at temperatures between 200 to 250°C.

For the beam-pipe bake-out in July 2008 the beam pipe was equipped with independent heaters to allow individual heating of all beam-pipe sections in the ATLAS interaction region[2]. In case of an emergency, the beam pipe heaters can be switched off immediately

---

[2] Sections cover e.g. the central Be beam pipe integrated into the Pixel Detector package; the stainless

by the ATLAS Detector Safety System (DSS) [118], a system complementary to the control and low-level safety DCS, designed to put the detector in a safe state in case of an abnormal situation potentially dangerous for the detector. Nevertheless the time to reach a safe temperature can be quite long, due to the thermal inertia of the beam pipe itself. Therefore the cooling system has to reliably guarantee sufficient cooling to keep the detector at a safe temperature, assumed to be below 0°C.

A.2.1. Initial Setup

Mainly due to an accident, severely damaging the cooling system, earlier in 2008, the system was not yet fully operational and stabilised. To still be able to perform the beam-pipe bake-out, fitting the tight operation schedule of both ATLAS and the LHC, the Pixel Detector was operated in dedicated *Bake-out Mode* to minimise the potential risk for the detector and the cooling plant, while having all necessary cooling loops operational. The setup of this *Bake-out Mode* is described in detail in [113]. In terms of cooling loops the partly operational system covered all Layer-0 loops, only Layer-1 loops operated from the A-side as well as all end-cap loops besides loop 46. A list of operational cooling loops is stated in Table A.1. To validate the chosen settings a selection of thermal tests has been carried out during the days before the beam-pipe bake-out itself. Switching off single cooling loops as well as the complete cooling plant in a controlled manner gave valuable insights into the performance of single and the interplay of neighbouring cooling loops as well as the system as a whole, to evaluate possible dangers in case of similar events during the actual beam-pipe bake-out. The results of the preceding thermal tests are reported in the next section.

Table A.1.: List of cooling loops active during the beam pipe bake-out period. The optoboard circuits (02, 22, 23, 50, 51, 72, 73) were kept on during the preceding thermal tests to allow for detector tests, but were switched off before the actual bake-out.

Quadrant	Cooling Loops
Q1	03, 17, 02, 14, 19, 21, 04, 16, 18, 15, 20
Q2	24, 39, 23, 35, 36, 41, 43, 22, 25, 26, 38, 40, 37, 42
Q3	45, 52, 47, 49, 51, 63, 44, 50, 53, 48, 64, 65
Q4	67, 74, 75, 71, 73, 86, 66, 68, 72, 76, 70, 87, 88

A.2.2. Results from Thermal Tests

In order to assess the risk for the detector components at high beam-pipe heater temperatures, measurements at two lower temperatures have been done which could then be extrapolated to the expected behaviour at high temperatures. Due to changes in the magnitude of the radiative, conductive as well as convective heat transfer, this extrapolation is difficult and can only provide a rough estimate. The quantities to be extracted from the

---

steel (SS) beam pipe sections passing through the calorimeter end-caps; and the SS beam pipe sections passing through the end-cap toroids.

Table A.2.: Groups of bi-staves and sectors (cooling loops) used in the thermal tests.

Group	**Bi-stave/Bi-sector (cooling loop)**
I	L0_B3 (loop 35), D1A_B2 (loop 16), D3C_B2 (loop 43)
II	L0_B7 (loop 64), L0_B11 (loop 88), D2A_B2 (loop 39)
III	L0_B8 (loop 65), D3C_B3 (loop 49)

measurements are the basic time constant and the maximum variation of the temperature of the sensors, since both fast and large temperature changes have a negative impact on the lifetime and the performance of the detector. Three groups of cooling loops, as stated in Table A.2, were identified due to their location as well as thermal properties and used for the tests. L0_B3 is the bi-stave just above the beam pipe, while L0_B8 and L0_B11 are beneath the beam pipe and on the side right at the mid-plane, respectively. L0_B7 was chosen as a neighbouring bi-stave to L0_B8 to verify the loose thermal coupling between neighbouring staves. Among the chosen disc sectors, sector 2 denotes top quadrant, while sector 3 is situated on the side. While a loose thermal coupling is expected between discs in one end-cap, connected sectors on one disc have a strong thermal coupling. In addition the thermal convection in the end-caps is stifled, due to an additional polyimide foil wrapping, possibly further increasing the temperature at the top. All measurements were performed at beam-pipe heater temperatures of 60°C and 120°C. For technical reasons L0_B7 (loop 64) was not turned off for the test at 120°C. To illustrate the thermal behaviour of the detector during the tests, an exemplary temperature profile, showing the average module temperature of stave L0_B3_S1_A7 (Group I), is given in Figure A.1. The complete test can be divided into four phases, visible as distinct features in Figure A.1. In Phase I (about 13h00 to 13h45) all three groups of cooling loops have been switched off separately while keeping the rest of the detector untouched and the beam-pipe heater temperature at 60°C. The whole cooling plant was shut down in Phase II (about 15h40 to 17h00). The same procedures were repeated at 120°C during Phase III (about 18h30 to 19h00) and IV (about 20h40 to 21h40), respectively.

It could be observed that in all four cases the loss in cooling power, either for individual groups of cooling loops or the whole plant, resulted in an initial drop in temperature. This is caused by the low pressure evaporation of the remaining coolant, the so-called dry-out, in the cooling pipes. The duration of this process is represented by the dry-out time t_{dry}. After reaching a minimum temperature T_{min}, the temperature rises asymptotically until reaching the environmental temperature. In this specific setup a maximum temperature T_{max} is reached just before the cooling system is switched back on. Especially in the cases where the whole cooling plant was switched off (Phase II and IV), the minimum temperature T_{min} can reach very low values down to -35°C. While this, due to the nitrogen atmosphere in the Pixel Detector volume, causes no harm, it is the large temperature gradient during the warm-up that can cause long-term damage to the detector. The beginning of the dry-out, the times of reaching T_{min} and T_{max} as well as the temperatures themselves have been extracted from DCS data, in an automated procedure. The exact times of switching off (parts of) the cooling system were (a) not equal for all loops and (b) not recorded; therefore they had to be extracted for all cooling loops from data afterwards.

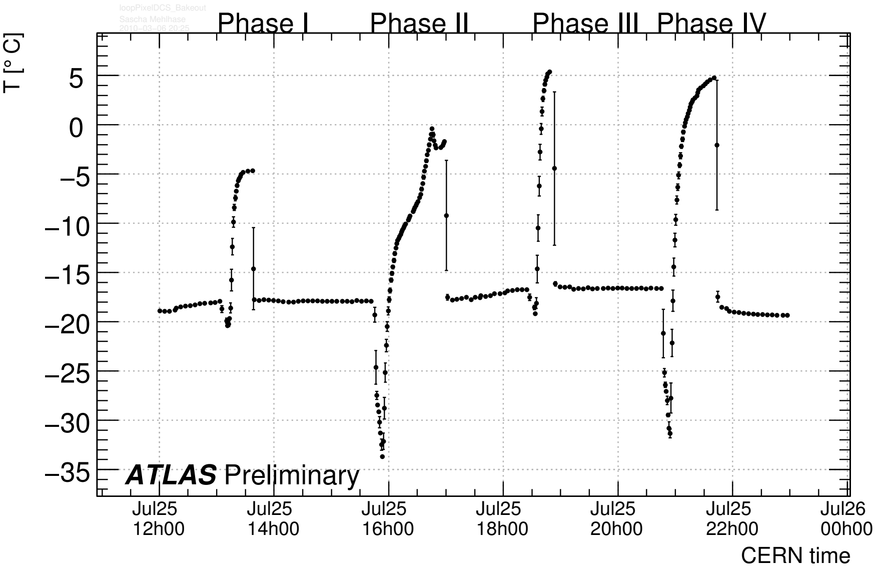

Figure A.1.: Time trend of the average module temperature of stave L0_B3_S1_A7 (Group I, top of L0) during the thermal tests.

The dry-out times together with the maximum temperature difference $\Delta T_{\mathrm{max}} = T_{\mathrm{max}} - T_{\mathrm{min}}$ are stated in Table A.3 for all four phases of the test and each of the three groups as well as the rest of the cooling loops if applicable. For the topmost Layer-0 cooling loop (L0_B3), closest to the heated beam-pipe and most affected by thermal convection, the dry-out time was about six minutes in Phase I and III and about eight minutes in Phase II and IV. The maximum temperature difference ΔT_{max} was found to be 16°C, 33°C, 26°C and 37°C in Phases I, II, III and IV, respectively. The effect of thermal convection within the Pixel Detector volume is further illustrated in Figure A.2, showing ΔT_{max} in Phase II for all staves in Layer 2 as a function of ϕ. Due to the heat rising up in the Pixel Detector volume the temperature of the modules in the upper part is already quite high (slightly below 0°C), while the rest of the detector was at about −20°C. As a result, clearly visible in Figure A.2, ΔT_{max} is much smaller in the upper part than in the lower part of Layer 2. Similar plots for the other layers can be found in [113].

Especially in Phase II and IV, even after the dry-out, the beam-pipe temperature was still at 90°C or above, further decreasing to roughly 35°C in about 15 minutes. Even though the numbers presented looked less worrying for the top sectors in the end-caps, it was concluded that normal operation at heater temperatures of 200°C, as foreseen for the actual bake-out, has to be considered unsafe.

A.2.3. Results from Beam-pipe Bake-out

The actual beam-pipe bake-out was again divided into phases: Phase I, in which the beam-pipe heaters were switched off; Phase II, with the heaters at 130°C; and Phase III, with heaters at 200°C (considered unsafe based on the thermal tests). Though the heaters were off during Phase I the temperature within the Pixel Detector volume varied between

Table A.3.: Dry-out times t_{dry} and maximum temperature variations ΔT_{max} averaged within each of the three groups (or the rest of the cooling loops, if applicable) during all four phases.

Phase		**Group I**	**Group II**	**Group III**	**Others**
I	$\langle \Delta T_{\mathrm{max}} \rangle$ [°C]	13±3	4±3	4±3	n.a.
	$\langle t_{\mathrm{dry}} \rangle$ [min]	9±3	9±4	15±2	n.a.
II	$\langle \Delta T_{\mathrm{max}} \rangle$ [°C]	34±1	30±2	30±2	29±5
	$\langle t_{\mathrm{dry}} \rangle$ [min]	10±2	12±2	10±1	11±3
III	$\langle \Delta T_{\mathrm{max}} \rangle$ [°C]	19±7	7±4	4±2	n.a.
	$\langle t_{\mathrm{dry}} \rangle$ [min]	8±2	10±3	15±2	n.a.
IV	$\langle \Delta T_{\mathrm{max}} \rangle$ [°C]	37±1	32±3	31±3	31±5
	$\langle t_{\mathrm{dry}} \rangle$ [min]	10±2	11±4	12±1	10±3

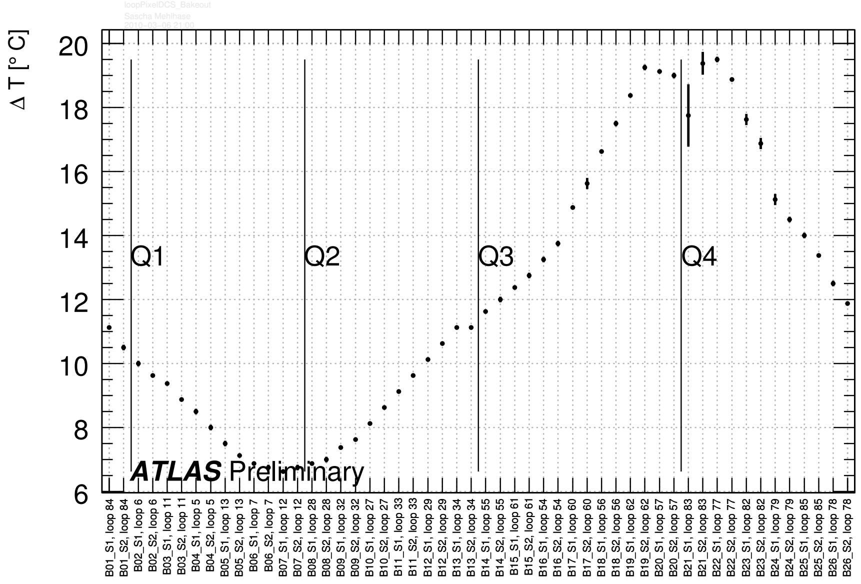

Figure A.2.: Maximum temperature difference ΔT_{max} for all cooling loops in Layer 2 during Phase II. See text for interpretation.

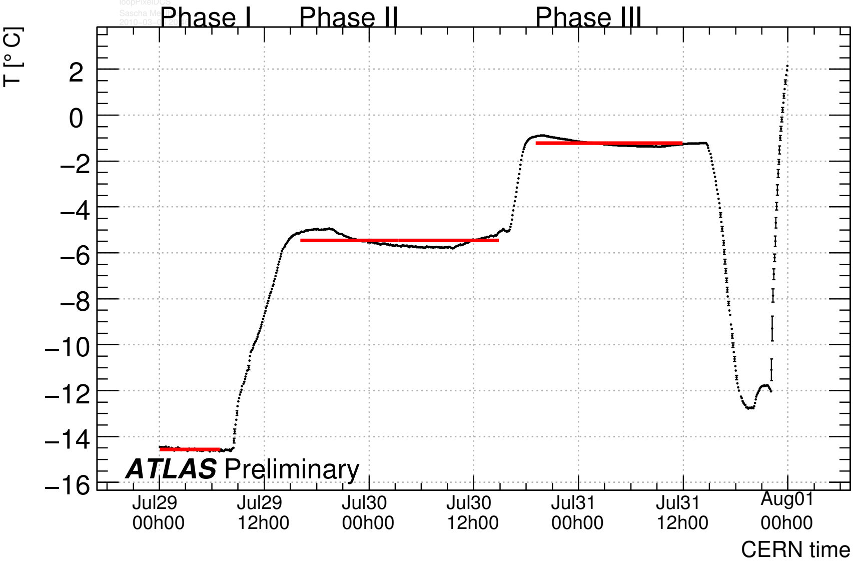

Figure A.3.: Time trend of the average module temperature of stave L2_B8_S2_C6 (top of L2) during the beam-pipe bake-out. The rise in the end is due to a shutdown of the cooling plant, similar to those seen in the thermal tests. The straight (red) lines represent fits with a constant function to the three phases of the beam-pipe bake-out.

−1°C (−16°C) and −20°C (−22°C) in the top and bottom part of the barrel (end-caps), respectively. Mainly due to convection this difference was also still caused by the preceding thermal test. An exemplary temperature profile spanning the whole beam-pipe bake-out period is given in Figure A.3. To extract the temperature change between the phases, fits with a constant function given by the straight (red) lines in Figure A.3, were performed for all cooling loops. Figures A.4(a) and A.4(b) shows the temperature difference between Phase I and III for all staves in Layer 1 and Layer 2, respectively.

The effect of the beam-pipe bake-out can be clearly seen in Figure A.4, as there is a strong ϕ dependence visible in the non-operational cooling loops (see Table A.1), especially in Layer 2. Also in Layer 1 the non-operational cooling loops show up with distinctively higher temperature changes and a strong ϕ dependence.

A.3. Low Back–Pressure Test

As introduced in Section 3.2.4, the operating temperature of the Pixel Detector modules is defined by a back-pressure regulator (BPR) in the exhaust line of each cooling loop. The default back-pressure for the 2008 operation period was set to three bar absolute (bara). The low back-pressure test was carried out to characterise the current and future performance of the Pixel Detector and its cooling system. By changing the back-pressure and using special detector configurations *end-of-life* conditions could be resembled and important insights into the future performance were obtained. During the back-pressure

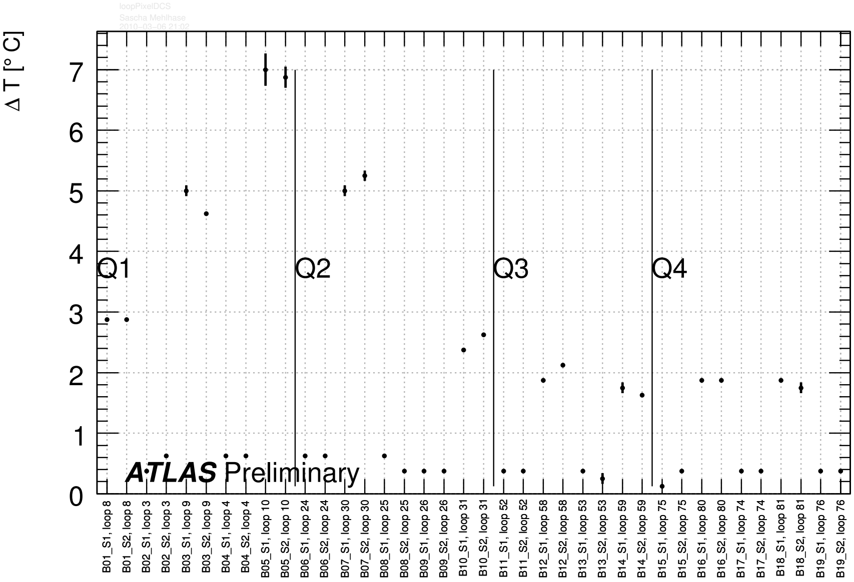

(a) Layer 1

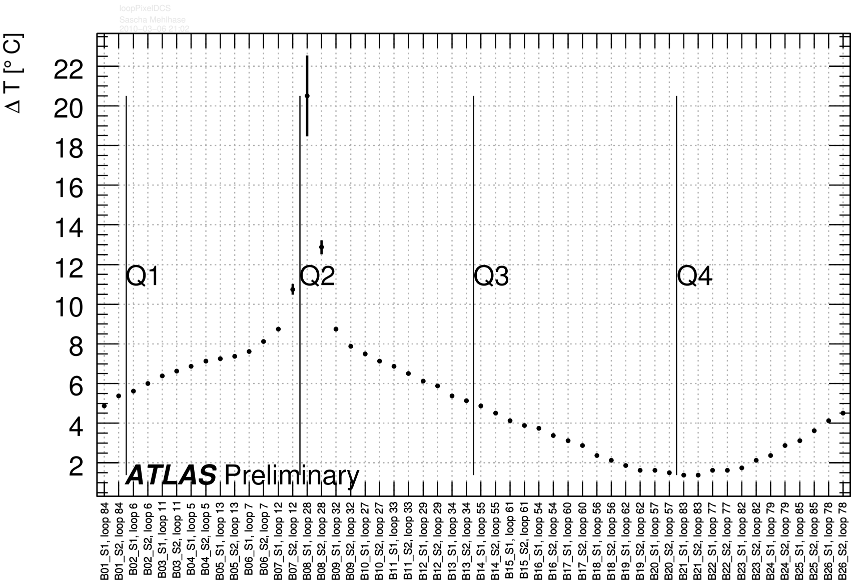

(b) Layer 2

Figure A.4.: Temperature difference between Phase I and III of the beam-pipe bake-out for all staves in (a) Layer 1 and (b) Layer 2, respectively. See text for interpretation. Additional material can be found in [113].

test, the setting of the BPR was varied from the nominal 3 bara down to 1 bara, in discrete steps of half a bar each, and back up to the nominal value in steps of one bar. After transition times of one to two minutes the system was given approximately 25 minutes to stabilise. An illustration, reflecting these changes on the BPR in terms of temperature changes measured on an exemplary stave in Layer 0, is shown in Figure A.5. The thermal condition as well as the module configuration status for each of the eleven settings (Phase I to XI), as indicated in Figure A.5, is summarised in Table A.4. In Phase VI, with the BPR at 1 bara, the modules have been put into a special configuration of high-power consumption, resembling the *end-of-life* operation conditions. As a result of compensating inefficiencies and increased leakage currents due to the irradiation of the sensors, the power drawn by each module will increase from the current about 3.5 W to above 5 W. Measurements dedicated to the *end-of-life* operation conditions and performed during Phase VI will be discussed in one of the following sections.

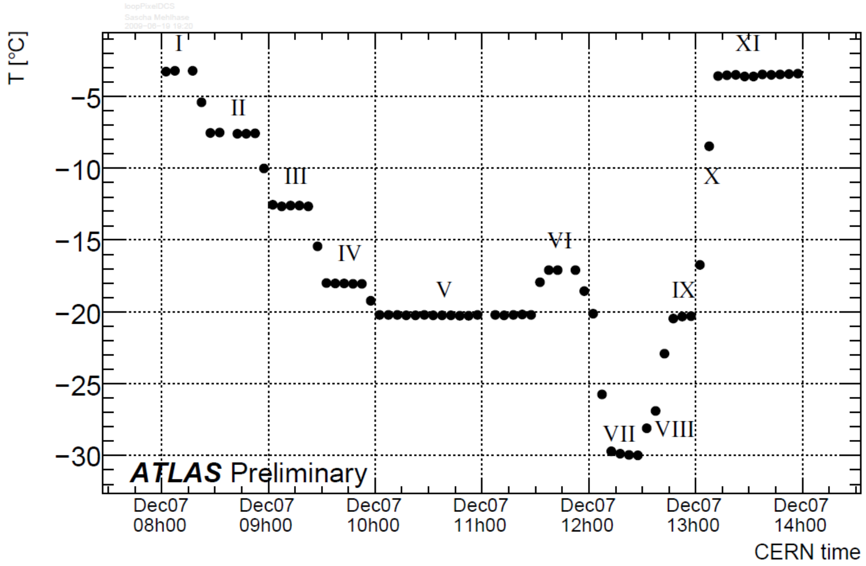

Figure A.5.: Profile of the average module temperature on stave L0_B1_S1_A7, spanning all eleven phases summarised in Table A.4.

A.3.1. Thermal Mapping of the Pixel Detector

To study the thermal behaviour of the Pixel Detector, the absolute module temperature as well as the module temperature relative to the temperature measured at the inlet or outlet of the corresponding cooling pipe have been mapped in all phases of the test. This gave an important insight on how different parts of the detector respond to changes at the BPR and can be used to determine the optimal working point for the Pixel Detector. The BPR working point was changed from 3 to 2 bara at the beginning of the 2009 operation period, also based on the thermal maps obtained from Phase II of this low back-pressure test.

An exemplary map of module temperatures in Layer 2 during Phase VI, resembling the

Table A.4.: Overview of all phases of the low back-pressure test. The setting of the Back-Pressure (BPR), the module configuration status (C: configured, U: unconfigured) as well as the drawn power P and module temperature T averaged over different groups of modules (Discs, Barrel inserted pipes, Barrel other) are stated.

Phase	**BPR [bara]**	**Status**	$\langle P \rangle$ [W] Discs	$\langle P \rangle$ [W] Barrel inserted	$\langle P \rangle$ [W] Barrel others	$\langle T \rangle$ [°C] Discs	$\langle T \rangle$ [°C] Barrel inserted	$\langle T \rangle$ [°C] Barrel others
I	3.0	C	3.3	3.7	3.7	−5.7	0.9	−3.0
II	2.5	C	3.3	3.4	3.7	−10.2	−3.6	−7.1
II	2.0	C	3.3	3.7	3.7	−15.6	−7.6	−11.9
IV	1.5	C	3.3	3.3	3.7	−21.6	−12.5	−17.2
V	1.0	C	3.3	3.7	3.7	−25.0	−14.9	−19.6
VI	1.0	C	5.1	5.1	4.9	−22.1	−9.5	−15.9
VII	1.0	U	0.8	0.9	0.9	−32.1	−29.3	−30.4
VIII	1.0	U	1.2	1.3	1.3	−30.4	−25.4	−27.0
IX	1.0	C	3.3	3.7	3.7	−25.4	−15.2	−19.7
X	2.0	C	–	–	–	–	–	–
XI	3.0	C	3.3	3.7	3.7	−6.1	0.6	−3.5

above mentioned *end-of-life* operation conditions is given in Figure A.6. It clearly shows the increased temperature in all cooling loops having the additional pipe inserted (see Section 3.2.4). While the remaining part of the detector (also in the Discs, Layer 0 and Layer 1, not shown here, see [113]) could be cooled down to temperatures between −20°C and −15°C (−25°C and −20°C for the Discs), the modules on these cooling loops have temperatures of −5°C to 5°C. Figure A.7 shows the distribution of module temperatures for different parts of the detector (Layer 0, Layer 1, inserted Layer 2, other Layer 2, Discs) during this configuration.

The *end-of-life* operation conditions during Phase VI did not only allow for projections on the future performance of the system, but also offered an optimal setup to study the performance of the evaporative cooling system. Due to the high power consumption and the low module temperatures, expected system responses will be enhanced and therefore measured more easily. Figure A.8 shows the module temperature distribution as a function of the distance from the inlet of the cooling pipe. Due to the obvious effect of the inserted pipes on the inlet side of the Layer-2 circuits, Layer 2 has been displayed separately from the other two layers. An increase both in the spread and the absolute value of the module temperatures (see also Figure A.7) is observable for these circuits. This behaviour was expected albeit not as strong as observed. The thermal performance of Disc modules (not shown here) is better compared to barrel modules (Discs at about −22°C in high-power configuration). It could be shown that, besides all discrepancies, the main project requirement of having an operating temperature below 0°C for the whole detector can be fulfilled even for modules with inserted pipes in Layer 2 and under *end-of-life* conditions. Also instantly visible in this configuration is the dependence of the module temperature on the distance to the inlet of the cooling circuit. The red line in Figure A.8 represents a linear fit to the mean temperatures excluding the first two modules. This exclusion is based on the fact that due to turbulent flow of the coolant, caused by the change in diameter when

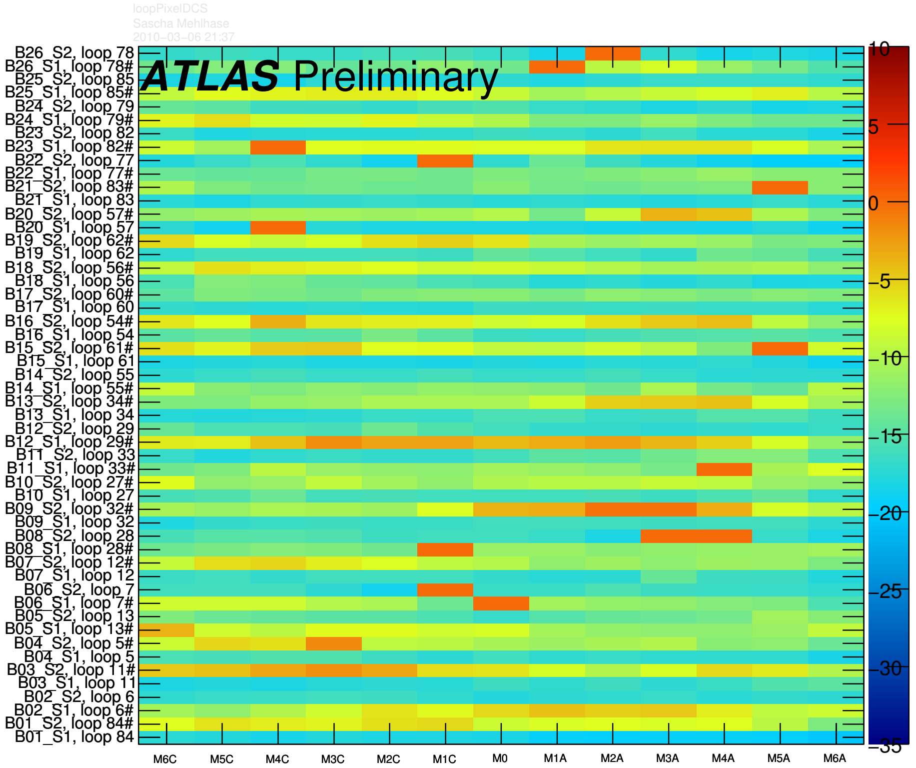

Figure A.6.: Map of module temperatures during Phase VI of the low back-pressure test. Each bin corresponds to a single module, with its module number (η position) and stave number (ϕ position) given on the x-axis and y-axis, respectively. The hash sign indicates staves with an inserted pipe.

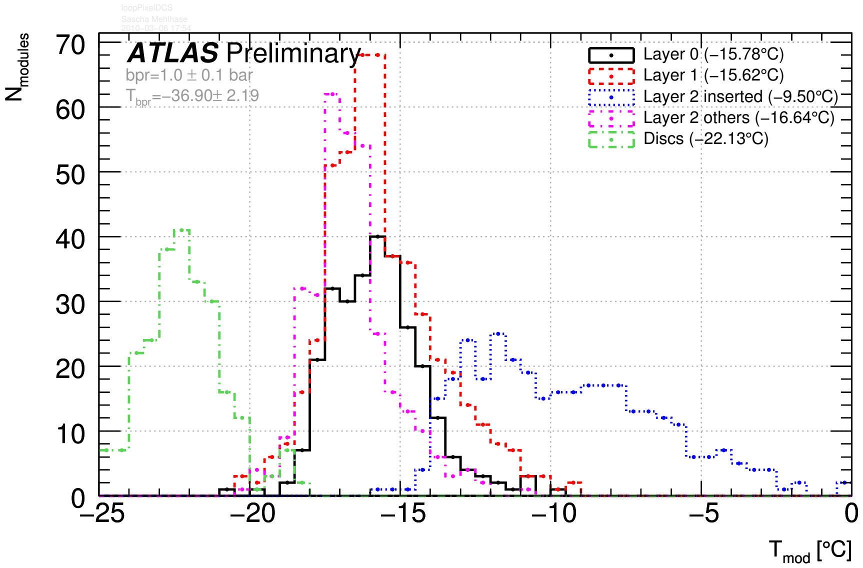

Figure A.7.: Distribution of module temperatures for different parts of the detector (Layer 0, Layer 1, inserted Layer 2, other Layer 2, Discs) during Phase VI of the low back-pressure test.

entering the cooling pipes, the first two modules are cooled slightly below the expected value. The estimated depth of this effect is about 8 cm [119], therefore the effect on the second module (module length: 6 cm) is less pronounced. The total temperature difference between the first and the last module on a circuit is given by (-2.5 ± 0.2)°C for Layer 0 and Layer 1. The same measurement performed in Layer 2, though fitted in two parts (inlet and outlet side), yields a consistent result of $(-2.8 \pm 0.7)^\circ\mathrm{C} = (-1.3 \pm 0.7)^\circ\mathrm{C} + (-1.5 \pm 0.2)^\circ\mathrm{C}$. The consistency of the two constant fits (blue lines) between the two plots shows that the inserted pipes on the inlet side in Layer 2 have no influence on the performance on the outlet side of the cooling circuit.

A.3.2. Thermal Performance of the Pixel Detector Modules

To evaluate the thermal performance of the modules it is interesting to look at the power-temperature relation. The low back-pressure test offered a unique setting to study this relation, by combining data from Phase V, VI and VII. Measuring the power-temperature relation together with the relative change of both values (not shown here) between different configurations / phases allows for a characterisation of the cooling performance similar to the one carried out during the post-installation tests (also called sign-off) of the Pixel Detector [113]. During the sign-off this analysis was limited to measurements on a stave-wise basis, averaging all modules on one stave. The measurements carried out during the low back-pressure test were the first measurement of this kind on a module-by-module basis. In Figure A.9 the module temperature is shown as a function of the module power for different parts of the detector. In agreement with the measurements carried out during the sign-off of the Pixel Detector, the dependence of the temperature on the module

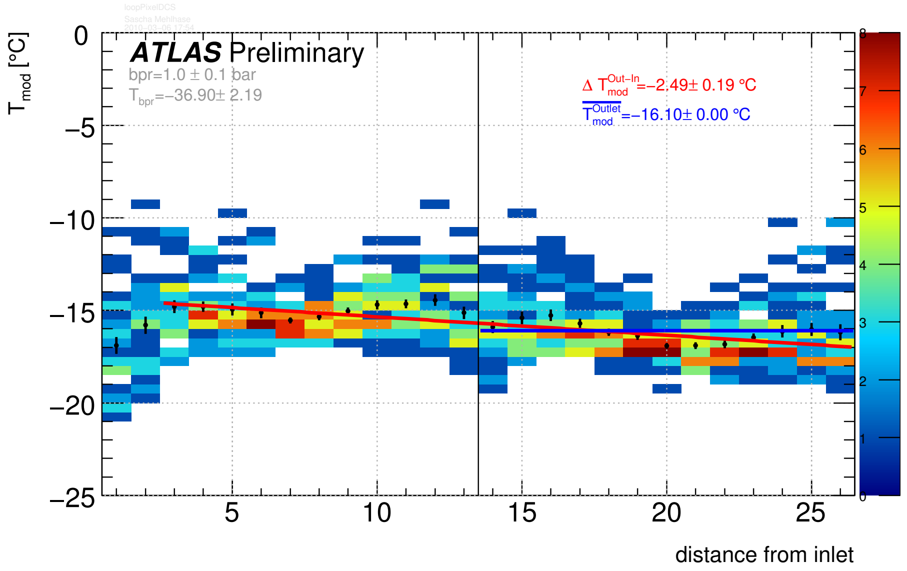

(a) Layer 0 and Layer 1

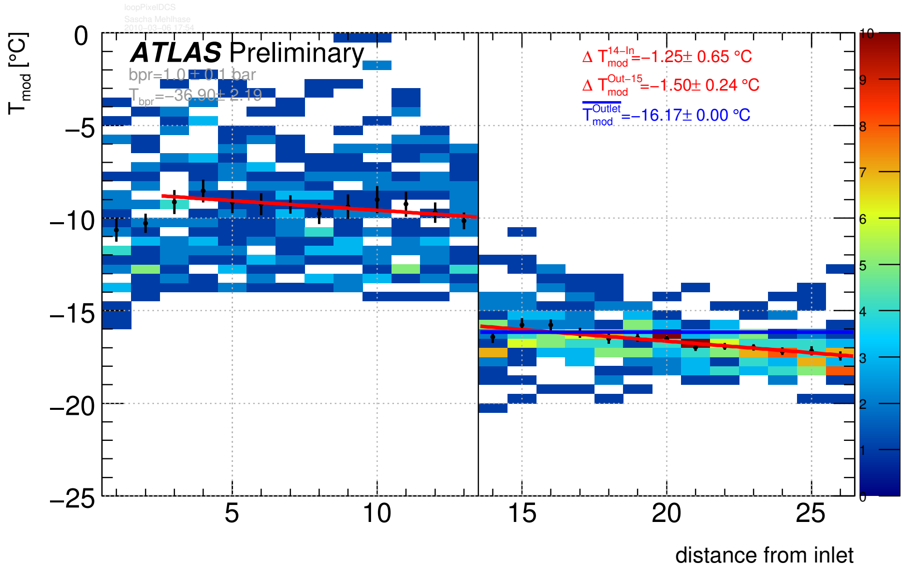

(b) Layer 2

Figure A.8.: Module temperature distribution as a function of the distance from the inlet of the cooling pipe (for barrel modules only). The black markers denote the mean temperature for each distance. The blue line is a constant fit to the temperatures of the outlet side of the pipe, while the red line is a linear fit. Stated in the plots are the value of the constant as well as the change in temperature of the whole pipe (separately for inlet and outlet in Layer 2), derived from the linear fits.

power is roughly linear, even under *end-of-life* conditions. By applying a linear fit to these distributions the mean slope for each given group of modules has be found to be: (3.7 ± 0.5)°C/W for Layer-0 and Layer-1 modules, (4.7 ± 0.8)°C/W for Layer-2 modules on cooling loops with inserted pipes, (3.4 ± 0.4)°C/W for the remaining Layer-2 modules and (2.4 ± 0.3)°C/W for end-cap modules. It can be seen that modules in Layer 0, Layer 1 as well as on non-inserted pipes in Layer 2 and especially in the Discs show a very homogeneous behaviour. In contrary modules on inserted pipes in Layer 2 show a large spread of roughly twice the value of the other barrel modules. The linear behaviour of the relation as well as the measured slopes again lead to the conclusion that the cooling circuits have sufficient cooling power, also looking at a future operation of the Pixel Detector. The fact that the modules on the non-inserted pipe in Layer 2 show similar proportionality compared to Layer-0 and Layer-1 modules consolidates the conclusion that the inserted pipes on the inlet side have no significant influence on the thermal performance of the modules on the outlet side of a cooling circuit.

A.4. Operational Performance of the Pixel Detector

In addition to the analyses based on data from specific events, presented in the sections above, a complete study of the operational performance of the Pixel Detector during the commissioning phase of 2008 has been carried out as part of this thesis. These very technical studies will only be summarised in the following, leaving the reader with reference [113] for a detailed description.

The analyses covered the characterisation of the thermal environment of the Pixel Detector and its services, starting from PP2 down to PP0, both during stable cooling system operation and during special events. The latter included dedicated module configurations for unstable LHC beams and during detector calibration as well as cases of failure in the mono-phase cooling of the off-detector services. Stable periods however are, due to frequent changes in the thermal conditions during the 2008 commissioning phase, found only during cosmic ray data taking.

Starting at PP2, housing the Regulator Stations (PP2 Crates) responsible for regulating the low voltage generated by commercial off-the-shelf power supplies in the ATLAS service caverns and provided to the FE electronics, the studies investigated e.g. the influence of the physical position of the crates within a rack, the number of connected PP0s and the number of crates sharing one rack. Also the interplay between the detector and the Regulator Stations have been subject of investigations. Going closer towards the detector, the thermal environment around PP1 and PP0 has been characterised by mapping temperatures at various points inside this region as a function of their geometrical position. This included e.g. investigations of the influence on the thermal behaviour of the ϕ-position (octant), the distance from the actual detector. Furthermore a detailed characterisation of the thermal performance of the optoboards, including effects related to the connected optoheaters, was carried out. Finally the operational performance of the Pixel Detector itself was studied. Possible correlations between the performance and e.g. the geometrical position of the modules, the cooling pipes or the manufacturing-institute of the stave[3].

---

[3] The modules build at various institutes have all been loaded onto the staves in Genoa, Marseilles or

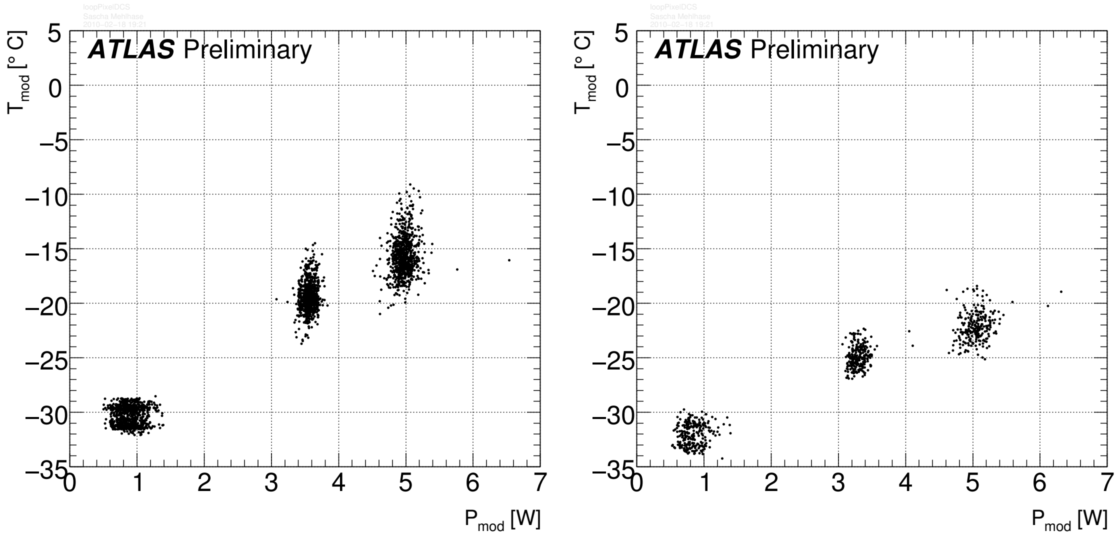

(a) Layer 0 and Layer 1

(b) Discs

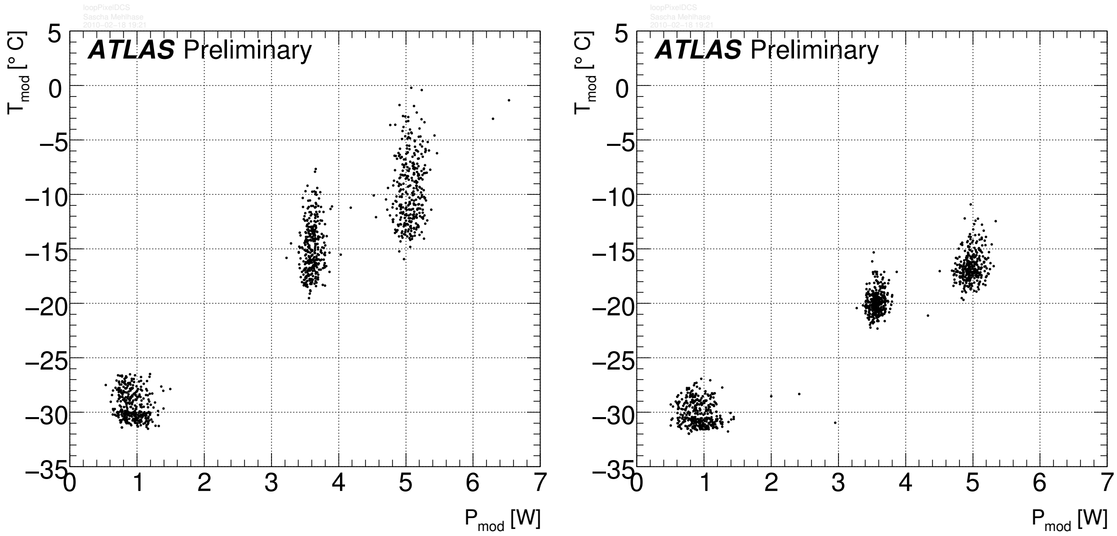

(c) inserted Layer 2

(d) other Layer 2

Figure A.9.: Module temperature as a function of the module power measured in Phase V, VI and VII for different parts of the detector.

With the exception of a few, all measurements yield results within expectation and specification of the system. While most discrepancies could be understood and/or resolved, some remain under investigation. An example covering all levels, from the off-detector services to the detector itself, will be highlighted in the following.

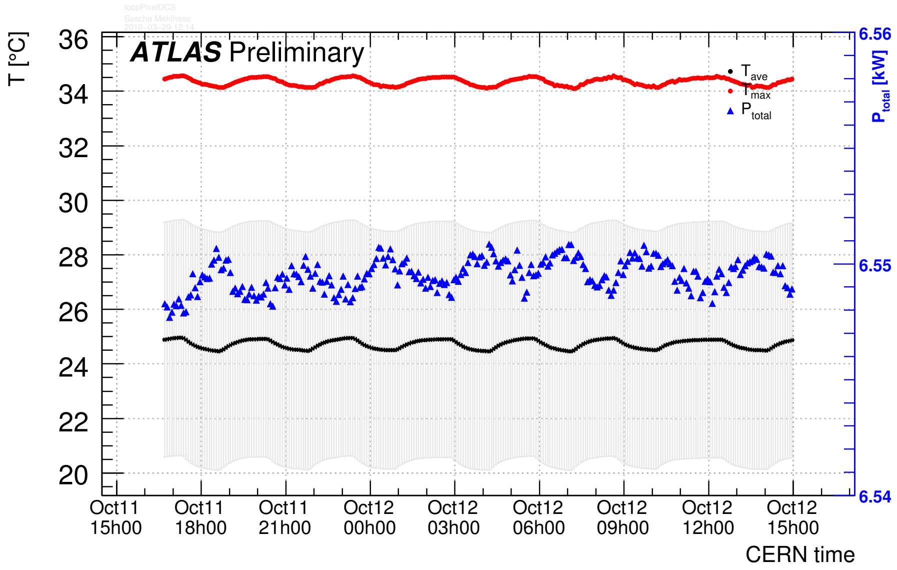

Figure A.10.: Maximum and average temperature of all PP2 Crate NTCs (all sensors on all crates; left ordinate) as well as the total power drawn by the Pixel Detector (right ordinate) versus time during a phase of stable running. The error bars for the average temperature represent the spread over all Crate NTCs of the detector.

During the characterisation of the operational performance of the PP2 Crates in stable running periods, given by times of cosmic data taking[4], small but periodic fluctuations of the temperatures measured at PP2 have been observed. Using the software introduced above, a correlation between these variations and fluctuations of the total power consumed by the detector has been observed. Both fluctuations, with a period of approximately three hours, are illustrated in Figure A.10. The variations can neither be observed for individual modules nor at the level of optoboards, hence must be marginal at this level and only shows up in the summation of the power. Due to the anti-cyclic variation of the detector power it can be concluded that the cause for these fluctuations is not due to changes in the power consumption. While this problem is not yet fully understood the current best explanation assumes that due to some cycle of the external cooling plant either the temperature or the flux of the coolant is varying with such a temporal modulation. This can be affirmed by the fact that this variation can already be seen at the inlet of the PP2 Crate cooling pipe. The change of the measured power is then based on a temperature dependent reading of the voltages at PP2. Following this explanation it is only the measured value of the power that changes while the real setting remains stable.

Wuppertal, using slightly different techniques.

[4] Run 91387 in 2008 in this specific case.

Appendix B.

Trigger Efficiency Calculation and Turn-On Fit

B.1. Trigger Efficiency Calculation

The efficiency is determined as

$$\varepsilon = \frac{N^{\text{pass}}}{N^{\text{total}}}, \tag{B.1}$$

where N^{pass} is the number of events that pass the trigger criterion and N^{total} is the total number of events. The uncertainty is given by the variance of the binomial distribution, ε (1-ε), divided by the number of generated events N^{total} as

$$\sigma_\varepsilon = \sqrt{\frac{\varepsilon(1-\varepsilon)}{N^{\text{total}}}}. \tag{B.2}$$

This calculation is only valid for $\varepsilon \neq 0, 1$. Though there are possible corrections for this, they all fail in cases of dealing with weighted events. Especially in cases where different weights are used for individual events (or groups of events) one has to extend the given equation, as described in [120], to

$$\varepsilon = \frac{\sum_{\text{pass}} w_i}{\sum_{\text{total}} w_i}, \tag{B.3}$$

where w_i is the weight of event i. The uncertainty σ_ε is then given by

$$\sigma_\varepsilon = \frac{\sqrt{\sum_{\text{pass}} w_i^2 (\sum_{\text{fail}} w_i)^2 + \sum_{\text{fail}} w_i^2 (\sum_{\text{pass}} w_i)^2}}{\left(\sum_{\text{total}} w_i\right)^2}. \tag{B.4}$$

In case of unweighted events both equations simplify to Equations (B.1) and (B.2), respectively.

B.2. Trigger Turn-On Fit Function

To fit the trigger item turn-on curves, namely the trigger efficiency ε as a function of the p_{T} threshold value, a Fermi-Dirac-like function given by

$$\varepsilon(p_{\mathrm{T}}) = \varepsilon^{\mathrm{offset}} + \frac{\varepsilon^{\mathrm{plateau}} - \varepsilon^{\mathrm{offset}}}{1 + \exp\left[-s \cdot \left(p_{\mathrm{T}} - p_{\mathrm{T}}^{\mathrm{threshold}}\right)\right]}, \tag{B.5}$$

where $\varepsilon^{\mathrm{offset}}$ denotes the starting efficiency (usually zero), $\varepsilon^{\mathrm{plateau}}$ represents the efficiency at the plateau reached at high p_{T} values, s is proportional to the slope of the rise and $p_{\mathrm{T}}^{\mathrm{threshold}}$ is the p_{T} value for which $\varepsilon\ (p_{\mathrm{T}})$ is half way between $\varepsilon^{\mathrm{offset}}$ and $\varepsilon^{\mathrm{plateau}}$. All these parameters are obtained from the fit and allow, using the function above, to extract e.g. the p_{T} value yielding 90% efficiency for a given trigger item threshold. While turn-on curves are often fitted with an error function variety, such as

$$\varepsilon(p_{\mathrm{T}}) = \varepsilon^{\mathrm{offset}} + \frac{\varepsilon^{\mathrm{plateau}}}{2}\left[1 + \mathrm{Erf}\left(\frac{p_{\mathrm{T}} - p_{\mathrm{T}}^{\mathrm{threshold}}}{\sqrt{2} \cdot \sigma}\right)\right], \tag{B.6}$$

where σ denotes the width of the turn on and Erf is the error function given by

$$\mathrm{Erf}(x) = \frac{2}{\pi}\int_0^x e^{-t^2} dt, \tag{B.7}$$

the function given in Equation (B.5) gave better results, e.g. in terms of a χ^2 test, in all cases presented within this thesis.

Bibliography

[1] S. W. Herb et al. Observation of a Dimuon Resonance at 9.5 GeV in 400 GeV Proton - Nucleus Collisions. *Phys. Rev. Lett.*, 39:252–255, 1977. doi: 10.1103/PhysRevLett.39.252.

[2] F. Abe et al. (CDF Collaboration). Observation of Top Quark Production in $\bar{p}p$ Collisions. *Phys. Rev. Lett.*, 74:2626–2631, 1995. doi: 10.1103/PhysRevLett.74.2626.

[3] S. Abachi et al. (D0 Collaboration). Observation of the Top Quark. *Phys. Rev. Lett.*, 74:2632–2637, 1995. doi: 10.1103/PhysRevLett.74.2632.

[4] S. Willenbrock. *The Standard Model and the Top Quark*. University of Illinois, Urbana-Champaign, 2002.

[5] D. Griffiths. Introduction to Elementary Particles. *Wiley-VCH (2008) 454 p*, 2008.

[6] V. D. Barger and R. J. N. Phillips. Collider Physics. *Addison-Wesley (1987) 592 P. (Frontiers in Physics, 71)*, 1987.

[7] S. Weinberg. A Model of Leptons. *Phys. Rev. Lett.*, 19(21):1264–1266, Nov 1967. doi: 10.1103/PhysRevLett.19.1264.

[8] S. L. Glashow. Partial Symmetries of Weak Interactions. *Nucl. Phys.*, 22:579–588, 1961. doi: 10.1016/0029-5582(61)90469-2.

[9] A. Salam and J. C. Ward. Electromagnetic and Weak Interactions. *Phys. Lett.*, 13: 168–171, 1964. doi: 10.1016/0031-9163(64)90711-5.

[10] M. Gell-Mann. Symmetries of Baryons and Mesons. *Phys. Rev.*, 125(3):1067–1084, Feb 1962. doi: 10.1103/PhysRev.125.1067.

[11] D. J. Gross and F. Wilczek. Asymptotically Free Gauge Theories. I. *Phys. Rev. D*, 8(10):3633–3652, Nov 1973. doi: 10.1103/PhysRevD.8.3633.

[12] H. D. Politzer. Asymptotic Freedom: An Approach to Strong Interactions. *Phys. Rept.*, 14:129–180, 1974. doi: 10.1016/0370-1573(74)90014-3.

[13] F. Reines and C. L. Cowan. Detection of the Free Neutrino. *Phys. Rev.*, 92:830–831, 1953. doi: 10.1103/PhysRev.92.830.

[14] G. Danby et al. Observation of High-Energy Neutrino Reactions and the Existence of Two Kinds of Neutrinos. *Phys. Rev. Lett.*, 9:36–44, 1962. doi: 10.1103/PhysRevLett.9.36.

[15] K. Kodama et al. (DONUT Collaboration). Observation of Tau-Neutrino Tnteractions. *Phys. Lett.*, B504:218–224, 2001. doi: 10.1016/S0370-2693(01)00307-0.

[16] J. J. Thomson. Cathode rays. *Phil. Mag.*, 44:293–316, 1897.

[17] J. C. Street and E. C. Stevenson. New Evidence for the Existence of a Particle of Mass Intermediate between the Proton and Electron. *Phys. Rev.*, 52:1003–1004, 1937. doi: 10.1103/PhysRev.52.1003.

[18] M. L. Perl et al. Evidence for Anomalous Lepton Production in e^+e^- Annihilation. *Phys. Rev. Lett.*, 35:1489–1492, 1975. doi: 10.1103/PhysRevLett.35.1489.

[19] M. Gell-Mann. A Schematic Model of Baryons and Mesons. *Phys. Lett.*, 8:214–215, 1964. doi: 10.1016/S0031-9163(64)92001-3.

[20] J. J. Aubert et al. (E598 Collaboration). Experimental Observation of a Heavy Particle J. *Phys. Rev. Lett.*, 33:1404–1406, 1974. doi: 10.1103/PhysRevLett.33.1404.

[21] J. E. Augustin et al. (SLAC-SP-017 Collaboration). Discovery of a Narrow Resonance in e^+e^- Annihilation. *Phys. Rev. Lett.*, 33:1406–1408, 1974. doi: 10.1103/PhysRevLett.33.1406.

[22] D. P. Barber et al. Discovery of Three Jet Events and a Test of Quantum Chromodynamics at PETRA Energies. *Phys. Rev. Lett.*, 43:830, 1979. doi: 10.1103/PhysRevLett.43.830.

[23] M. Planck. Über das Gesetz der Energieverteilung im Normalspectrum. *Annalen Phys.*, 309(3):553–563, 1901. doi: 10.1002/andp.19013090310.

[24] A. Einstein. Concerning an Heuristic Point of View toward the Emission and Transformation of Light. *Annalen Phys.*, 322(6):132–148, 1905. doi: 10.1002/andp.19053220607.

[25] G. Arnison et al. (UA1 Collaboration). Experimental Observation of Isolated Large Transverse Energy Electrons with Associated Missing Energy at $\sqrt{s} = 540$ GeV. *Phys. Lett.*, B122:103–116, 1983.

[26] M. Banner et al. (UA2 Collaboration). Observation of Single Isolated Electrons of High Transverse Momentum in Events with Missing Transverse Energy at the CERN $p\bar{p}$ Collider. *Phys. Lett.*, B122:476–485, 1983. doi: 10.1016/0370-2693(83)91605-2.

[27] G. Arnison et al. (UA1 Collaboration). Experimental Observation of Lepton Pairs of Invariant Mass around 95 GeV/c^2 at the CERN SPS Collider. *Phys. Lett.*, B126: 398–410, 1983. doi: 10.1016/0370-2693(83)90188-0.

[28] M. Banner et al. (UA2 Collaboration). Evidence for $Z^0 \to e^+e^-$ at the CERN $p\bar{p}$ collider. *Phys. Lett.*, B129:130–140, 1983. doi: 10.1016/0370-2693(83)90744-X.

[29] J. C. Collins and D. E. Soper. The Theorems of Perturbative QCD. *Ann. Rev. Nucl. Part. Sci.*, 37:383–409, 1987.

[30] J. C. Collins, D. E. Soper, and G. Sterman. Heavy Particle Production in High-Energy Hadron Collisions. *Nucl. Phys.*, B263:37, 1986. doi: 10.1016/0550-3213(86)90026-X.

[31] I. Abt et al. (H1 Collaboration). The H1 Detector at HERA. *Nucl. Instrum. Meth.*, A386:310–347, 1997. doi: 10.1016/S0168-9002(96)00893-5.

[32] ZEUS Collaboration. The ZEUS Detector: Status Report 1993. *ZEUS-STATUS-REPT-1993*, 1993.

[33] V. N. Gribov and L. N. Lipatov. Deep Inelastic e-p Scattering in Perturbation Theory. *Sov. J. Nucl. Phys.*, 15:438–450, 1972.

[34] G. Altarelli and G. Parisi. Asymptotic Freedom in Parton Language. *Nucl. Phys.*, B126:298, 1977. doi: 10.1016/0550-3213(77)90384-4.

[35] Y. L. Dokshitzer. Calculation of the Structure Functions for Deep Inelastic Scattering and e^+e^- Annihilation by Perturbation Theory in Quantum Chromodynamics. *Sov. Phys. JETP*, 46:641–653, 1977.

[36] J. Pumplin et al. New Generation of Parton Distributions with Uncertainties from Global QCD Analysis. *JHEP*, 07:012, 2002.

[37] Alan D. Martin, R. G. Roberts, W. J. Stirling, and R. S. Thorne. MRST2001: Partons and α_s from Precise Deep Inelastic Scattering and Tevatron Jet Data. *Eur. Phys. J.*, C23:73–87, 2002. doi: 10.1007/s100520100842.

[38] A. D. Martin, R. G. Roberts, W. J. Stirling, and R. S. Thorne. Uncertainties of Predictions from Parton Distributions. 1: Experimental Errors. *Eur. Phys. J.*, C28: 455–473, 2003. doi: 10.1140/epjc/s2003-01196-2.

[39] W. A. Bardeen, A. J. Buras, D. W. Duke, and T. Muta. Deep Inelastic Scattering Beyond the Leading Order in Asymptotically Free Gauge Theories. *Phys. Rev.*, D18: 3998, 1978. doi: 10.1103/PhysRevD.18.3998.

[40] HEPDATA databases. `http://durpdg.dur.ac.uk/hepdata/pdf3.html`, 2010.

[41] P. Nason, S. Dawson, and R. K. Ellis. The total cross section for the production of heavy quarks in hadronic collisions. *Nuclear Physics B*, 303(4):607–633, 1988. ISSN 0550-3213. doi: DOI:10.1016/0550-3213(88)90422-1.

[42] W. Beenakker, H. Kuijf, W. L. van Neerven, and J. Smith. QCD Corrections to Heavy-Quark Production in $p\bar{p}$ Collisions. *Phys. Rev. D*, 40(1):54–82, Jul 1989. doi: 10.1103/PhysRevD.40.54.

[43] G. Aad et al. (ATLAS Collaboration). *Expected Performance of the ATLAS Experiment - Detector, Trigger and Physics.* CERN, Geneva, 2009.

[44] R. Bonciani, S. Catani, M. L. Mangano, and P. Nason. NLL Resummation of the Heavy-Quark Hadroproduction Cross-Section. *Nucl. Phys.*, B529:424–450, 1998. doi: 10.1016/S0550-3213(98)00335-6.

[45] M. Cacciari, S. Frixione, M. L. Mangano, P. Nason, and G. Ridolfi. Updated Predictions for the Total Production Cross Sections of Top and of Heavier Quark Pairs at the Tevatron and at the LHC. *JHEP*, 09:127, 2008. doi: 10.1088/1126-6708/2008/09/127.

[46] N. Kidonakis and R. Vogt. The Theoretical Top Quark Cross Section at the Tevatron and the LHC. *Phys. Rev.*, D78:074005, 2008. doi: 10.1103/PhysRevD.78.074005.

[47] S. Moch and P. Uwer. Theoretical Status and Prospects for Top-Quark Pair Production at Hadron Colliders. *Phys. Rev.*, D78:034003, 2008. doi: 10.1103/PhysRevD.78.034003.

[48] A. D. Martin, R. G. Roberts, and W. J. Stirling. Parton Distributions: A Atudy of the New HERA Data, alpha(s), the Gluon and p Anti-p Jet Production. *Phys. Lett.*, B387:419–426, 1996. doi: 10.1016/0370-2693(96)01031-3.

[49] P. M. Nadolsky et al. Implications of CTEQ Global Analysis for Collider Observables. *Phys. Rev.*, D78:013004, 2008. doi: 10.1103/PhysRevD.78.013004.

[50] W. K. Tung et al. Heavy Quark Mass Effects in Deep Inelastic Scattering and Global QCD Analysis. *JHEP*, 02:053, 2007.

[51] S. Catani. Aspects of QCD, from the Tevatron to the LHC, 2000.

[52] T. Aaltonen et al. (CDF Collaboration). First Observation of Electroweak Single Top Quark Production. *Phys. Rev. Lett.*, 103:092002, 2009. doi: 10.1103/PhysRevLett.103.092002.

[53] V. M. Abazov et al. (D0 Collaboration). Observation of Single Top-Quark Production. *Phys. Rev. Lett.*, 103:092001, 2009. doi: 10.1103/PhysRevLett.103.092001.

[54] M. Kobayashi and T. Maskawa. CP Violation in the Renormalizable Theory of Weak Interaction. *Prog. Theor. Phys.*, 49:652–657, 1973. doi: 10.1143/PTP.49.652.

[55] Z. Sullivan. Understanding Single-Top-Quark Production and Jets at Hadron Colliders. *Phys. Rev.*, D70:114012, 2004. doi: 10.1103/PhysRevD.70.114012.

[56] J. M. Campbell and F. Tramontano. Next-to-Leading Order Ccorrections to W-t Production and Decay. *Nucl. Phys.*, B726:109–130, 2005. doi: 10.1016/j.nuclphysb.2005.08.015.

[57] C. Amsler et al. (Particle Data Group). Review of Particle Physics (with 2009 Partial Update for the 2010 Edition). *Phys. Lett.*, B667:1, 2008. doi: 10.1016/j.physletb.2008.07.018.

[58] Tevatron Electroweak Working Group. Combination of CDF and D0 Results on the Mass of the Top Quark. *preprint*, 2009.

[59] N. Besson, M. Boonekamp, E. Klinkby, S. Mehlhase, and T. Petersen. Re-evaluation of the LHC potential for the Measurement of m_W. *Eur. Phys. J.*, C57:627–651, 2008. doi: 10.1140/epjc/s10052-008-0774-4.

[60] ALEPH Collaboration. Precision Electroweak Measurements on the Z Resonance. *Phys. Rept.*, 427:257, 2006. doi: 10.1016/j.physrep.2005.12.006.

[61] ALEPH, CDF, D0, DELPHI, L3, OPAL, SLD Collaborations, LEP, Tevatron Electroweak Working Group, and SLD Electroweak Heavy Flavour Groups. Precision Electroweak Measurements and Constraints on the Standard Model. *preprint*, 2009.

[62] W. Bernreuther, A. Brandenburg, Z. G. Si, and P. Uwer. Top Quark Pair Production and Decay at Hadron Colliders. *Nucl. Phys.*, B690:81–137, 2004. doi: 10.1016/j.nuclphysb.2004.04.019.

[63] T. Aaltonen et al. (CDF Collaboration). Measurement of W-Boson Helicity Fractions in Top-Quark Decays Using $\cos\theta^*$. *Phys. Lett.*, B674:160–167, 2009. doi: 10.1016/j.physletb.2009.02.040.

[64] V. M. Abazov et al. (D0 Collaboration). Model-Independent Measurement of the W Boson Helicity in Top Quark Decays at D0. *Phys. Rev. Lett.*, 100:062004, 2008. doi: 10.1103/PhysRevLett.100.062004.

[65] CDF Collaboration. Exclusion of Exotic Top-like Quark with $-4/3$ Electric Charge Using Soft Lepton Tags. *Fermi National Laboratory, CDF Note CDF/PUB/TOP/PUBLIC/9939*, 2010.

[66] V. M. Abazov et al. (D0 Collaboration). Experimental Discrimination Between Charge 2e/3 Top Quark and Charge 4e/3 Exotic Quark Production Scenarios. *Phys. Rev. Lett.*, 98:041801, 2007. doi: 10.1103/PhysRevLett.98.041801.

[67] D0 Collaboration. Useful Diagrams of Top Signals and Backgrounds. `http://www-d0.fnal.gov/Run2Physics/top/top_public_web_pages/top_feynman_diagrams.html`, September 2009.

[68] F. A. Berends, W. T. Giele, H. Kuijf, R. Kleiss, and W. J. Stirling. Multi-Jet Production in W, Z Events at $p\bar{p}$ colliders. *Phys. Lett.*, B224:237, 1989. doi: 10.1016/0370-2693(89)91081-2.

[69] CERN. *LEP Design Report: Vol. 1. The LEP Injector Chain.* CERN, Geneva, 1984. CERN-LEP-84-01.

[70] CERN. *LEP Design Report: Vol. 2. The LEP Main Ring.* CERN, Geneva, 1984. CERN-LEP-84-01.

[71] CERN. *LEP Design Report: Vol. 3. LEP2.* CERN, Geneva, 1996. CERN-AC-96-01-LEP-2.

[72] CERN. The CERN Accelerator Complex. `http://cdsweb.cern.ch/record/979035`, June 2006.

[73] G. Aad et al. (ATLAS Collaboration). The ATLAS Experiment at the CERN Large Hadron Collider. *JINST*, 3:S08003, 2008. doi: 10.1088/1748-0221/3/08/S08003.

[74] ATLAS Collaboration. Computer Generated Image of the whole ATLAS Detector. `http://cdsweb.cern.ch/record/1095924`, March 2008.

[75] K. G. Wilson. Confinement of Quarks. *Phys. Rev.*, D10:2445–2459, 1974. doi: 10.1103/PhysRevD.10.2445.

[76] ATLAS Collaboration. Event Cross Section in a Computer Generated Image of the ATLAS Detector. `http://cdsweb.cern.ch/record/1096081`, March 2008.

[77] ATLAS Collaboration. Computer Generated Image of the ATLAS Inner Detector. `http://cdsweb.cern.ch/record/1095926`, March 2008.

[78] ATLAS Pixel Collaboration. Commissioning of the ATLAS Pixel Detector. Technical Report ATL-COM-INDET-2010-???, CERN, Geneva, in preparation.

[79] G. Aad et al. (ATLAS Pixel Collaboration). ATLAS Pixel Detector Electronics and Sensors. *JINST*, 3:P07007, 2008. doi: 10.1088/1748-0221/3/07/P07007.

[80] I. Peric et al. The FEI3 Readout Chip for the ATLAS Pixel Detector. *Nucl. Instrum. Meth.*, A565:178–187, 2006. doi: 10.1016/j.nima.2006.05.032.

[81] J. Dopke et al. (ATLAS Pixel Collaboration). Commissioning of the ATLAS Pixel Optical Readout Link. Technical Report ATL-COM-INDET-2010-047, CERN, Geneva, Mar 2010. Internal note.

[82] H. Boterenbrood et al. Design and Implementation of the ATLAS Detector Control System. Technical Report ATL-DAQ-2003-043. 3, CERN, Geneva, May 2003.

[83] S. Mehlhase. Electron Identification with the TRT and the W Boson Mass Measurement at ATLAS. Master Thesis at Niels Bohr Institute, Copenhagen, February 2007.

[84] ATLAS Collaboration. Computer Generated Image of the ATLAS Calorimeter. `http://cdsweb.cern.ch/record/1095927`, March 2008.

[85] ATLAS Collaboration. *ATLAS Detector and Physics Performance*, volume I of *Technical Design Report ATLAS*. ATLAS Collaboration, CERN, 25 May 1999.

[86] ATLAS Collaboration. Computer Generated Image of the ATLAS Muons System. `http://cdsweb.cern.ch/record/1095929`, March 2008.

[87] P. Jenni et al. (ATLAS Collaboration). *ATLAS Forward Detectors for Measurement of Elastic Scattering and Luminosity.* Technical Design Report. CERN, Geneva, 2008.

[88] ATLAS Collaboration. *ATLAS level-1 trigger: Technical Design Report.* Technical Design Report ATLAS. ATLAS Collaboration, CERN, Geneva, 1998.

[89] ATLAS Collaboration. *ATLAS High-Level Trigger, Data-Acquisition and Controls.* Technical Design Report ATLAS. ATLAS Collaboration, CERN, Geneva, 2003.

[90] ATLAS Collaboration. *ATLAS computing: Technical Design Report.* Technical Design Report ATLAS. CERN, Geneva, 2005.

[91] M. A. Dobbs et al. Les Houches Guidebook to Monte Carlo Generators for Hadron Collider Physics, 2004.

[92] A. Shibata et al. Understanding Monte Carlo Generators for Top Physics. Technical Report ATL-COM-PHYS-2009-334, CERN, Geneva, Jun 2009. Internal note.

[93] T. Sjöstrand, S. Mrenna, and P. Z. Skands. PYTHIA 6.4 Physics and Manual. *JHEP*, 05:026, 2006.

[94] G. Corcella et al. HERWIG 6.5: an Event Generator for Hadron Emission Reactions With Interfering Gluons (Including Supersymmetric Processes). *JHEP*, 01:010, 2001.

[95] J. M. Butterworth, J. R. Forshaw, and M. H. Seymour. Multiparton Interactions in Photoproduction at HERA. *Z. Phys.*, C72:637–646, 1996. doi: 10.1007/s002880050286.

[96] B. P. Kersevan and E. Richter-Was. The Monte Carlo Event Generator AcerMC Version 2.0 with Interfaces to PYTHIA 6.2 and HERWIG 6.5, 2004.

[97] M. L. Mangano, M. Moretti, F. Piccinini, R. Pittau, and A. D. Polosa. ALPGEN, a Generator for Hard Multiparton Processes in Hadronic Collisions. *JHEP*, 07:001, 2003.

[98] S. Frixione and B. R. Webber. Matching NLO QCD Computations and Parton Shower Simulations. *JHEP*, 06:029, 2002.

[99] S. Agostinelli et al. GEANT4: A Simulation Toolkit. *Nucl. Instrum. Meth.*, A506: 250–303, 2003. doi: 10.1016/S0168-9002(03)01368-8.

[100] E. Richter-Was, D. Froidevaux, and L. Poggioli. ATLFAST 2.0 a Fast Simulation Package for ATLAS. Technical Report ATL-PHYS-98-131, CERN, Geneva, Nov 1998.

[101] D. Cavalli et al. Performance of the ATLAS Fast Simulation ATLFAST. Technical Report ATL-PHYS-INT-2007-005. ATL-COM-PHYS-2007-012, CERN, Geneva, Jan 2007.

[102] D. Adams et al. The ATLFAST-II Performance in Release 14: Particle Signatures and Selected Benchmark Processes. Technical Report ATL-PHYS-INT-2009-110. ATL-COM-PHYS-2009-554, CERN, Geneva, Dec 2009.

[103] The Les Houches Accord PDF Interface. `http://hepforge.cedar.ac.uk/lhapdf/`, 2010.

[104] M. R. Whalley, D. Bourilkov, and R. C. Group. The Les Houches Accord PDFs (LHAPDF) and Lhaglue, 2005.

[105] M. L. Mangano. Merging Matrix Elements and Shower MCs. `http://cern.ch/~Emlm/talks/lund-alpgen.pdf`, 2004.

[106] J. Alwall et al. Comparative Study of Various Algorithms for the Merging of Parton Sshowers and Matrix Eelements in Hadronic Collisions. *Eur. Phys. J.*, C53:473–500, 2008. doi: 10.1140/epjc/s10052-007-0490-5.

[107] I. Abt et al. (H1 Collaboration). The Tracking, Calorimeter and Muon Detectors of the H1 Experiment at HERA . *Nucl. Instrum. Meth.*, A386:348–396, 1997. doi: 10.1016/S0168-9002(96)00894-7.

[108] V. M. Abazov et al. (D0 Collaboration). Measurement of the Shape of the Boson Rapidity Distribution for $p\bar{p} \to Z/gamma^* \to e^+e^- + X$ Events Produced at $\sqrt{s}$ of 1.96-TeV. *Phys. Rev.*, D76:012003, 2007. doi: 10.1103/PhysRevD.76.012003.

[109] M. L. Mangano. Understanding the Standard Model, as a Bridge to the Discovery of New Phenomena at the LHC. *Int. J. Mod. Phys.*, A23:3833–3848, 2008. doi: 10.1142/S0217751X08042353.

[110] V. Pavlunin and D. Stuart. Background Modeling in New Physics Searches Using Forward Events at LHC. *Phys. Rev.*, D78:035012, 2008. doi: 10.1103/PhysRevD.78.035012.

[111] J. Pumplin et al. Uncertainties of Predictions from Parton Distribution Functions. II. The Hessian Method. *Phys. Rev. D*, 65(1):014013, Dec 2001. doi: 10.1103/PhysRevD.65.014013.

[112] T. Gleisberg et al. Event Generation with SHERPA 1.1. *JHEP*, 02:007, 2009. doi: 10.1088/1126-6708/2009/02/007.

[113] ATLAS Pixel Collaboration. A Summary of Thermal Measurements from the Pixel Commissioning Program of 2008. Technical Report ATL-COM-INDET-2010-???, CERN, Geneva, in preparation. Internal note.

[114] R. Brun and F. Rademakers. ROOT: An Object Oriented Data Analysis Framework. *Nucl. Instrum. Meth.*, A389:81–86, 1997. doi: 10.1016/S0168-9002(97)00048-X.

[115] S. Mehlhase. Tool for Pixel Offline DCS Monitoring. `https://wiki-zeuthen.desy.de/ATLAS/Projects/Pixel/DCSSoftware`, 2010.

[116] S. Mehlhase. Tool for Pixel Offline DCS Monitoring - CVS Repository. `http://isscvs.cern.ch/cgi-bin/cvsweb.cgi/Pixel/mehlhase/?cvsroot=atdesyz`, 2010.

[117] O. Gröbner. The LHC vacuum system, 1999. Prepared for CERN Accelerator School Course on Vacuum Technology for Particle Accelerators, Copenhagen, Snekersten, Denmark, 28 May - 3 Jun 1999.

[118] O. Beltramello et al. The Detector Safety System of the ATLAS experiment. *JINST*, 4(09):P09012, 2009.

[119] Private Communications with C. Gemme (INFN) and D. Giugni (INFN)., 2009.

[120] B. List. Statistical Error of Efficiency Determination from Weighted Events. `www.desy.de/~blist/notes/effic.ps.gz`, 2003.

Selbständigkeitserklärung

Ich erkläre, dass ich die vorliegende Arbeit selbständig und nur unter Verwendung der angegebenen Literatur und Hilfsmittel angefertigt habe.

Berlin, den 31. Mai 2010 Sascha Mehlhase